*Thesis*

*On*

# To investigate the Microstructural Changes during Tensile Deformation of AISI 304L Austenitic Stainless Steels using In-Situ and Ex-Situ Tensile Experiment

*Submitted in partial fulfillment of the requirement for the award of degree*

*of*

**Master of Engineering**

*in*

**(PRODUCTION AND INDUSTRIAL ENGINEERING)**

*Submitted by:*

**Navjot Singh**

Roll No. 801182016

***Under the guidance of***

**Dr. Tarun Nanda**
Assistant Professor,
MED, TU, Patiala

**Dr. Swapan Kumar Das**
Principle Scientist (E-II)
MST Division, NML, Jamshedpur

## DEPARTMENT OF MECHANICAL ENGINEERING

## THAPAR UNIVERSITY

Patiala - 147004, Punjab, India

July, 2013

# DECLARATION

I hereby declare that the thesis report entitled '***To investigate the microstructural changes during tensile deformation of AISI 304L austenitic stainless steels using in-situ and ex-situ tensile experimentation***' is an authentic record of my thesis carried out as requirement for the award of degree of M.E (Production and Industrial Engineering) at Thapar University, Patiala under the supervision of Dr. Tarun Nanda, Assistant Professor, Thapar University, Patiala and Dr. Swapan Kumar Das, Principle Scientist E2, MST Division, National Metallurgical Laboratory (NML), Jamshedpur, during 4th semester, Jan-July 2013.

The matter presented in this report has not been submitted in any other University/Institute for award of Masters of Engineering or any other degree.

Date: 22/7/13

Navjot Singh

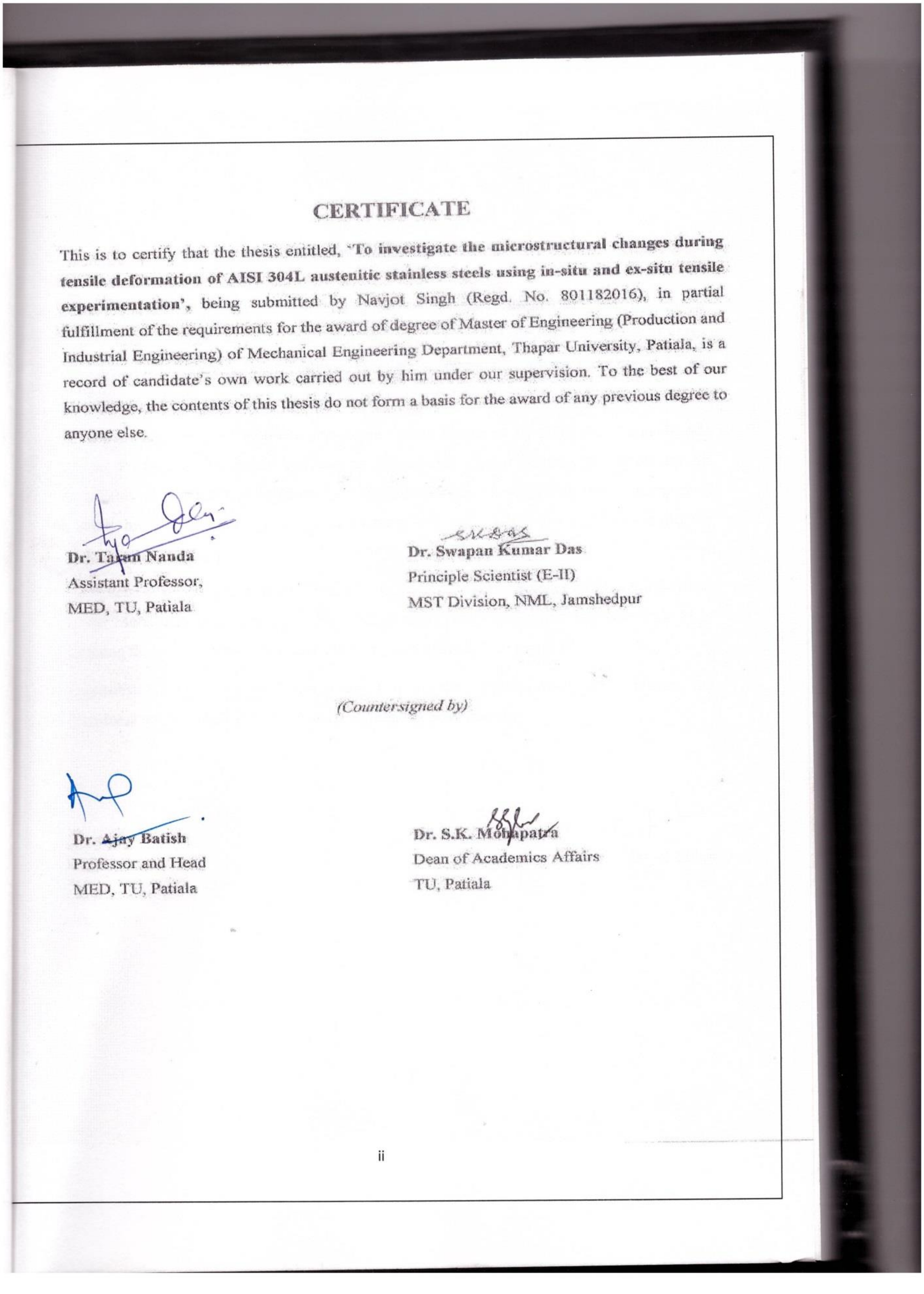

# CERTIFICATE

This is to certify that the thesis entitled, '**To investigate the microstructural changes during tensile deformation of AISI 304L austenitic stainless steels using in-situ and ex-situ tensile experimentation**', being submitted by Navjot Singh (Regd. No. 801182016), in partial fulfillment of the requirements for the award of degree of Master of Engineering (Production and Industrial Engineering) of Mechanical Engineering Department, Thapar University, Patiala, is a record of candidate's own work carried out by him under our supervision. To the best of our knowledge, the contents of this thesis do not form a basis for the award of any previous degree to anyone else.

**Dr. Tarun Nanda**
Assistant Professor,
MED, TU, Patiala

**Dr. Swapan Kumar Das**
Principle Scientist (E-II)
MST Division, NML, Jamshedpur

*(Countersigned by)*

**Dr. Ajay Batish**
Professor and Head
MED, TU, Patiala

**Dr. S.K. Mohapatra**
Dean of Academics Affairs
TU, Patiala

# ACKNOWLEDGEMENT

I would like to express my deep sense of gratitude to **Dr. Swapan Kumar Das**, Principle Scientist ($E_2$), Material Science and Testing division, National Metallurgical Laboratory (NML), Jamshedpur for his invaluable suggestions, excellent supervision, constant encouragement and critical discussion throughout the research work.

I express my deep sense of gratitude and a very sincere thanks to my guide **Dr. Tarun Nanda** Assistant Professor, Mechanical engineering department, Thapar University, Patiala for his indefatigable guidance and full support which helped me in the accomplishment of this project. I am highly indebted to them for their painstaking efforts and invaluable suggestions during the period of work.

I offer special regards to **Dr. B. Ravi Kumar**, Scientist ($E_2$), Material Science and Testing division, National Metallurgical Laboratory (NML), Jamshedpur for providing his immense support in performing the experimental work throughout my stay at NML, Jamshedpur.

The greatest thanks go to my **Parents** for their infinite support. Above all, I express my indebtedness to the "ALMIGHTY" for all His blessing and kindness.

**Navjot Singh**

# ABSTRACT

In the present times the main emphasis of research field is on improving the mechanical properties of various materials for industrial and other purposes. Austenitic stainless steels are very important materials for several applications where corrosion resistance is an important issue. The other important properties of this category of steels are very good formability, room-temperature and cryogenic toughness, good oxidation resistance and creep properties at elevated temperatures. But these steels have moderate yield strengths. Many processing routes have been developed till date to improve the mechanical strength of these steels at the expense of ductility. The main emphasis of the present work is to study and understand the microstructural changes in AISI 304L austenitic stainless steels during tensile deformation which can be used to further enhance their properties. The microstructural evaluation has been studied in respect of change in grain orientation, phase transformation and slip activated in the material during in-situ and ex-situ tensile experiments. Deformation behaviour of these steels is dependent on the crystal/grain orientation. So the microstructural changes in respect of grain orientation change and the effect of the annealing twins on the orientation change during in-situ tensile deformation at different strain levels is studied. The phenomenon of plastic deformation activated during in-situ tensile deformation and its correlation with grain orientation has also been described in the medium range of strain. In the latter part of the work, the nucleation sites of martensitic transformation from austenitic phase and its growth with increased stress has also been described in detail in bi-modal type austenite grains. It was noticed that the strain induced martensitic transformation observed in the bi-modal type austenite grains during tensile deformation is due to localized stresses induced in the small grains and in the strained grain boundary regions with high angle of misorientation.

# LIST OF FIGURES

# LIST OF TABLES

# LIST OF ACRONYMS

| **Acronym** | **Full Name** |
|---|---|
| ASS | Austenitic Stainless Steel |
| BM | Bi-Modal |
| BSE | Back-Scattered Electrons |
| CRSS | Critical Resolved Shear Stress |
| CSL | Coincidence Site Lattice |
| EBSD | Electron Back Scattered Diffraction |
| GB | Grain Boundary |
| IQ | Image Quality |
| OIM | Optical Imaging Microscopy |
| SEM | Scanning Electron Microscope |
| SFE | Stacking Fault Energy |
| SF | Stacking Fault |

| | |
|---|---|
| SIM | Strain Induced Martensite |
| SS | Stainless Steel |
| TRIP | Transformation Induced Plasticity |
| TWIP | Twinning Induced Plasticity |
| UFG | Ultrafine Grained |
| UTS | Ultimate Tensile Strength |
| YS | Yield Strength |

# Table of Contents

TITLE PAGE NO.

**DECLARATION**

**CERTIFICATE**

**ACKNOWLEDGEMENT**

**ABSTRACT**

**LIST OF FIGURES**

**LIST OF TABLES**

**LIST OF ACRONYMS**

# CHAPTER 1

# INTRODUCTION

## 1.1 GENERAL

Stainless steels (SS) are the most useful category in the family of steels due to their great properties like strength, formability, luster and corrosion resistance etc. These steels are widely used in many industrial, medical and marine applications etc. (Marshall, 1984). In the stainless steels category, the most important steels are austenitic stainless steels (ASSs). The use of stainless steels is growing due to their excellent corrosion resistance, ease of maintenance, attractive appearance, ductility, toughness and fire resistance (Gardner *et al*., 2006). These steels can also be strengthened by cold working method to achieve a high ultimate tensile strength (UTS) and yield strength (YS) values.

The main objective of the present work is to study the change in the microstructure in the respect of change in grain orientation/ misorientation and strain induced α'- martensite transformation during tensile deformation by in-situ scanning electron microscope (SEM) and electron back scattered diffraction (EBSD) analysis. The present study includes the effect of grain orientation on the deformation behavior of AISI 304L austenitic stainless steel. The rotation of the grains during the tensile deformation towards preferred orientation and the effect of the annealing twins on the deformation behavior are also discussed. Also, in the bi-modal type austenite grains, the strain induced α'- martensitic transformation and its effects are discussed.

## 1.2 STAINLESS STEELS

The resistance to corrosion (and other environmental conditions) provided by stainless steels shows a huge difference as compared to other steels. As a result the word 'stainless' had been added to this special category of steels. Several groups of alloys containing a minimum of 11% chromium content and other alloying elements mainly nickel are considered into stainless steel category. There are mainly three series of stainless steels. One is 300 series or austenitic stainless steels having chromium and nickel as the main alloying elements. The second series is 400 which contains chromium as main alloying element, and are ferritic or martensitic stainless steels. The third series is 200 series in which the high nickel contents of austenitic grade are replaced with manganese. Other than corrosion resistance, the stainless steels (SS) also have very good fabricating properties. Stainless steels can be formed into coils, sheets, plates, bars, wire/tubes to be used in cookware, household hardware, surgical instruments and industrial equipment. Further, their low maintenance requirements and good luster make them an ideal material for many applications. Due to the high chromium content, stainless steels have high corrosion resistance at elevated temperature applications. Addition of nickel in 300 series stainless steels reduces scaling and also provides good mechanical properties at high temperature. Stainless steels are used in low-end to very sophisticated applications like cooking utensils and furniture to space vehicles and in other many more applications like automotive industry (moldings, wiper arms, wheel rings etc.), dairy industry (to preserve cheese, butter and ice-cream etc.), soft drink industry, textile industry etc. (Park et al., 2010; Kumar et al., 2011; Yeddu et al., 2012). On the basis of properties, stainless steels are divided into five main grades.

(i) Austenitic Stainless Steels
(ii) Ferritic Stainless Steels
(iii) Martensitic Stainless Steels
(iv) Duplex Stainless Steels
(v) Precipitation Hardened Stainless Steels

Figures 1.1 and Figure 1.2 show the compositional and property diagrams of stainless steels.

## 1.3 AUSTENITIC STAINLESS STEELS

Austenitic Stainless Steels are the most common and familiar type of stainless steels. They have 70% production in the total production of stainless steels due to their wide applications and very good properties like corrosion resistance, formability, moderate strength and appearance etc. (Yuan et al., 2006; Lee et al., 2007; Milad et al., 2008; Das and Tarafder, 2009; Rocha and Oliveira, 2009; Park et al., 2010; Shen et al., 2012; Xu et al., 2012). These steels can be strengthened also by grain refinement (cold and hot working methods) to achieve a very high yield strength and tensile strength with good ductility. They are called so as their structure remains austenitic at all normal temperatures. These steels have face centered cubic (FCC) structure which is the main reason of their great formability. Due to the FCC structure austenite, these steels have very low stacking fault energy value and so can be work hardened to large extents for good strength and ductility combinations. The presence of nickel enables the austenitic structure to be retained stable at room temperature (Smith, 2008). They are most easily recognized as non-magnetic. They are extremely formable and weldable, and they can be successfully used from cryogenic temperatures to the red-hot temperatures of furnaces and jet engines. They contain between about 16 to 25% Cr,

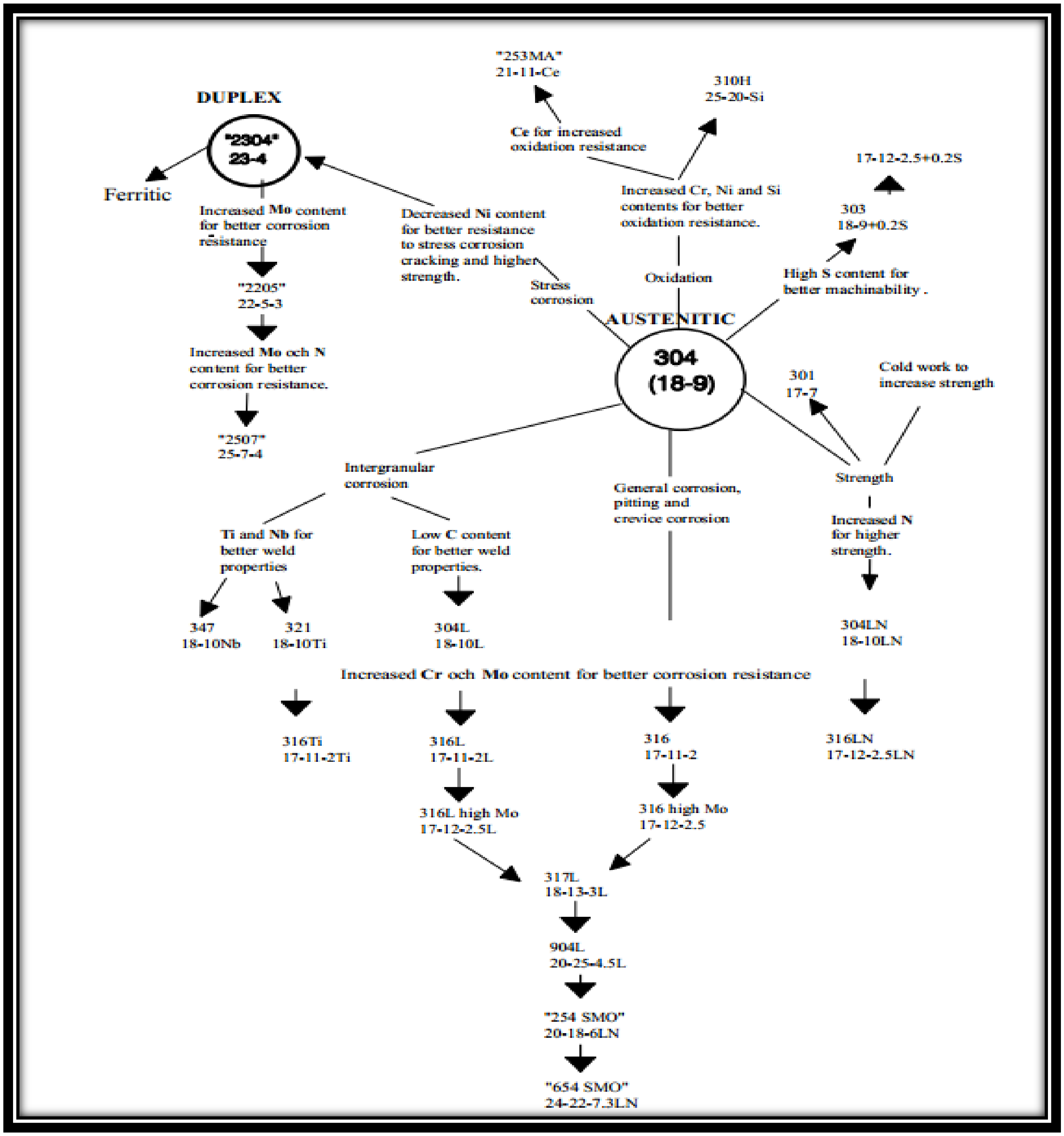

**Fig 1.1 Compositional and Property Relations for Austenitic and Duplex Stainless Steels**

(Image Source: Web Reference: Leffler, 2013)

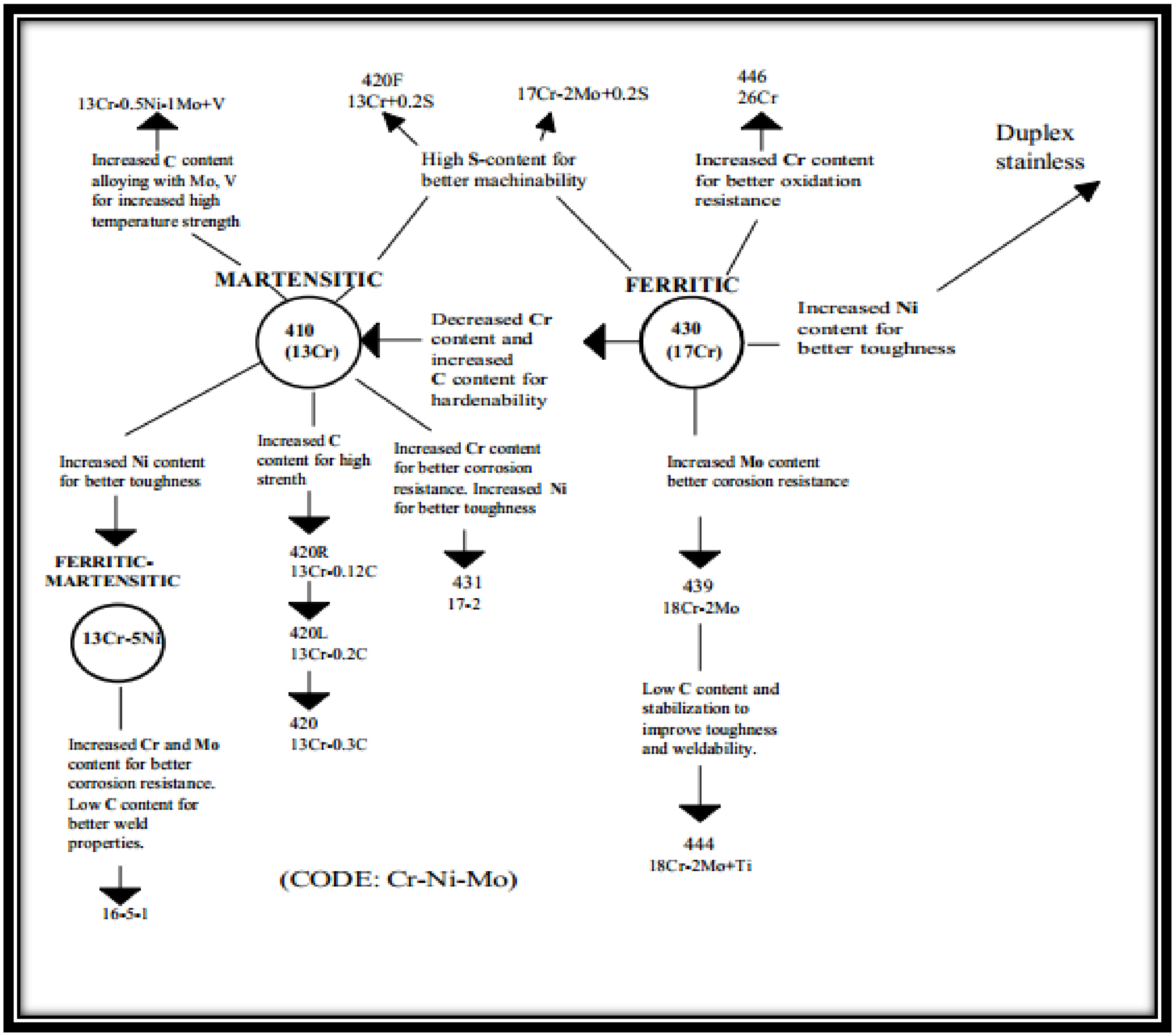

**Fig 1.2 Compositional and Property Relations for Martensitic and Ferritic Stainless Steels**

(Image Source: Web Reference: Leffler, 2013)

and can also contain nitrogen in solution, both of which contribute to their high corrosion resistance. They can be made soft enough (with a yield strength of about 200 MPa) to be easily formed by the same tools that work with carbon steel, but they can also be made incredibly strong by cold work (up to yield strengths of over 2000 MPa). Their austenitic structure is very tough and ductile down to absolute zero. They also do not lose their strength at elevated temperatures as rapidly as ferritic iron base alloys. The least corrosion-resistant versions can withstand the normal corrosive attack of the everyday environment (Callister, 2007; McGuire, 2008).

### 1.3.1 Common Grades of Austenitic Stainless Steels

Austenitic grades are the most commonly used grades of stainless steels mainly because, in many instances, they provide very predictable levels of corrosion resistance with excellent mechanical properties (McGuire, 2008). Some of the most important grades of ASS include AISI 316, AISI 316L, AISI 304, AISI 304L and AISI 301. Due to their good corrosion resistance, excellent weldability, very good formability and good luster, these grades are used in a large and varied range of applications such as automotive industries, food storage, transportation industries, surface piping, nuclear applications, paper industry, cookware and household hardware etc. (Elsariti and Haftirman, 2013). A brief description about the composition and properties of these most common grades is described as follows:

#### 1.3.1.1 AISI 304 Austenitic Stainless Steels

This grade of austenitic stainless steel is low carbon and chromium-nickel stainless steel with high heat resistivity. With good corrosion resistance and non-magnetic nature, this grade has very less stacking fault energy than the other grades of Austenitic Stainless Steel (ASS), so it is easily susceptible to work-hardening. However, these steels have low strength due to the low carbon content in them. But lower carbon content lowers the carbide precipitation which increases the corrosion resistance and lowers the brittleness at grain boundaries. This ASS consists of C=0.08% (max.); Cr=18-20%; Ni=8-10.5% as the main constituents and contains other constituents as Mn=2% (max.); P=0.045% (max.); S=0.030% (max.); Si=0.75% (max.). This grade is used for chemical processing equipment, for food, dairy, and beverage industries, for heat exchangers, and for the milder chemicals storage, nuclear power plants, marine applications etc. (Pickering, 1978; Web Reference: Aksteel, 2013, Espimetals, 2013).

#### 1.3.1.2 AISI 304L Austenitic Stainless Steels

The AISI 304L grade is a very low carbon stainless steel. Low carbon content is provided so as to avoid the formation of carbides due to which inter-granular corrosion takes place. The nickel content in the composition is slightly on the higher side due to which austenite phase inherits more stability. So, it slows down martensitic transformation by cold-deformation. This is also a chromium-nickel based austenitic stainless steel similar to AISI 304 grade with superior resistance to inter-granular corrosion after welding or stress relieving. This stainless steel contains C=0.03% (max.); Cr=18-20%; Ni=8-11% as the main constituents and Mn=2% (max.);

P=0.045% (max.); S=0.03% (max.) and Si=0.75% (max.) as minor constituents. This grade of steel does not require post weld annealing and finds extensive use in heavy gauge components where freedom from carbide precipitation is required (Pickering, 1978; Web Reference: Aksteel, 2013, Espimetals, 2013).

### 1.3.1.3 AISI 301 Austenitic Stainless Steels

This is also a chromium-nickel mixed stainless steel capable of attaining high tensile strength and good ductility by cold working. This grade of ASS contains, C=0.15% (max.); Cr=10-18%; Ni=6-8% as the main elements and Mn=2% (max.); P=0.045% (max.); S=0.030% (max.) and Si=0.75% (max) as minor elements. The available forms of this grade in market are sheet strip and wire forms. Corrosion resistance is similar to that of 304. This grade cannot be hardened by thermal treatment. Grade 301 and its low carbon variants are used where a high strength stainless steel is required. This grade gets work hardened at very high rates. High strength and excellent corrosion resistance make this steel useful for a wide variety of applications like aircraft structural parts, trailer bodies, diaphragms, utensils, automobile wheel covers, roof drainage products, etc. (Pickering, 1978; Web Reference: Aksteel, 2013).

### 1.3.1.4 AISI 316 Austenitic Stainless Steels

This grade contains molybdenum (2-3%) in it which gives extra corrosion resistance properties. Also more nickel is added to counterbalance molybdenum and to retain austenitic structure and provide required properties. This austenitic stainless steel has good heat resistance and has superior corrosion resistance against many types of chemical corrosives. This grade has superior creep strength at elevated temperatures. The constituents of this grade of ASS are C=0.08% (max.); Cr=16-18%; Ni=10-14%; Mn=2% (max.); P=0.045% (max.); Mo=2-3%; S=0.03% (max.); Si=1.0% (max.) and Cu=0.05% (max.). The weldability and resistance to pitting and corrosion in chloride environments is excellent. Grade 316 is the standard molybdenum-bearing grade. Molybdenum gives this steel better overall corrosion resistant properties than Grade 304, particularly higher resistance to pitting and crevice corrosion in chloride environments. It has excellent forming and welding characteristics. Typical uses include exhaust manifolds, furnace parts, heat exchangers, jet engine parts, pharmaceutical and photographic equipment, valves, chemical equipment, tanks, evaporators, paper and textile processing equipment, parts exposed to marine atmospheres and tubing. Type 316L is also used extensively for weldments where its immunity to carbide precipitation due to welding assures optimum corrosion resistance (Pickering, 1978; Web Reference: Aksteel, 2013, Espimetals, 2013).

#### 1.3.1.5 AISI 316L Austenitic Stainless Steels

Grade 316L is a low carbon version of AISI 316 and has similar corrosion resistance as AISI 316 grade but with superior inter-granular corrosion resistance after welding or stress relieving. This grade consists of C=0.03% (max.); Cr=16-18%; Ni=10-14%; Mn=1.25-2%; Mo=2-3%; P=0.04% (max.); Si=1.0% (max.); Cu=0.75% (max.). It is extensively used in heavy gauge welded components (over about 6mm). This grade is available in the market in forgings and castings of sheet strip, plate, bar, wire, tube/pipe shapes. The AISI 316L grade ASS is used in many applications such as food preparation equipment particularly in chloride environments, pharmaceuticals, marine applications, architectural applications, medical implants and fasteners etc. (Web Reference: Aksteel, 2013, Espimetals, 2013).

Figure 1.4 shows the compositional and property diagram for austenitic stainless steels.

## 1.4 TENSILE PROPERTIES OF AUSTENITIC STAINLESS STEELS

The study of mechanical properties and deformation behavior is generally studied by tensile testing because a single tensile test can provide large amount of information about the elastic and plastic properties of materials (viz. modulus of elasticity, elastic limit, percent elongation, reduction in area, yield strength, ultimate tensile strength (Hertzberg, 1996). ‘In situ’ is a Latin phrase which means ‘in position’. In-situ analysis of tensile testing means to study the deformation characteristics in a material happening right at the place and at every instant. An important work in conducting a tensile test is sample preparation. The tensile sample is of dog-bone shape having shoulders at ends and a reduced section between the shoulders. The measurements and the microstructural analysis are done in the section which is center of the reduced section called the gage length. Tensile properties of materials depend upon the sample size. As the gage length of the sample decreases, total strain in sample increases (McDowell et al., 1966). The holding of specimens is done at shoulders by several methods like gripping a threaded section made at end or by pinning etc. However, pinning is most suitable because of proper alignment.  Figure 1.3 shows a tensile specimen.

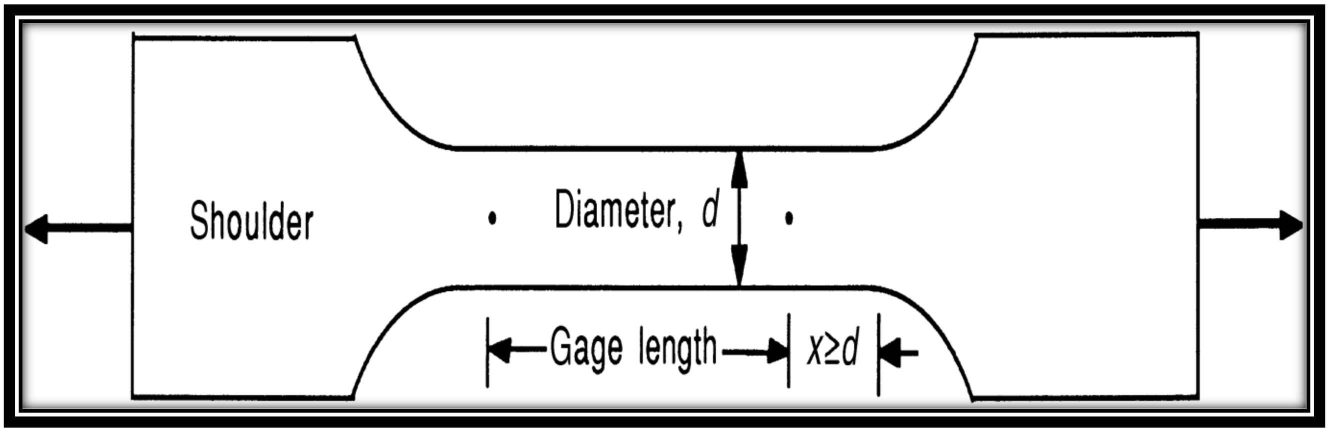

**Fig. 1.3 Tensile Specimen** (Image Source: McDowell, 1966)

In the present work, the tensile in-situ study of AISI 304 austenitic stainless steel has been done to study the various plastic deformation mechanisms working and the strain accumulation in the grains. The austenitic stainless steels are the steels having large tensile elongations (up to 62%) and moderate tensile strength (586-760 MPa) (McDowell et al., 1966). There are several factors which influence the tensile properties of austenitic stainless steels which are discussed as follows.

### 1.4.1 Role of Alloying Elements

Alloying elements play a very important role in the plastic deformation behavior and in the mechanical properties of stainless steels. Each and every element present in the composition plays a significant role in defining the properties and deformation behavior. The two major alloying elements present in ASS are chromium and nickel. The main role of chromium is to enhance corrosion resistance. Nickel is an austenite stabilizer. It retains the $\gamma$-phase in structure at room temperature. Ni (8% amount) decreases the $M_{s,}$ temperature just below the room temperature and so stabilizes $\gamma$-phase at room temperature. Chromium is a ferrite stabilizer, so as its amount increases above 18%, more nickel amount is needed to get fully austenitic structure. The 18Cr and 8Ni percentage combination makes the austenitic structure stable at room temperature with small amount of $\delta$-ferrite present in it. As amount of Ni increases up to 12%, fully austenitic structure is there. The elements with their weight percentage written in the Ni and Cr equivalent equations below in Equation 1.1 and Equation 1.2 perform the same functions as 1% wt. of Ni and Cr (Marshall, 1984).

- Ni equivalent = % Ni + % Co + 0.5% Mn + 30% C + 0.3% Cu + 25% N

………………….**Eq. 1.1**

- Cr equivalent = % Cr + 2.0% Si + 1.5% Mo + 5% V + 5.5% Al + 1.75% Nb + 1.5% Ti + 0.75% W

...........................**Eq. 1.2**

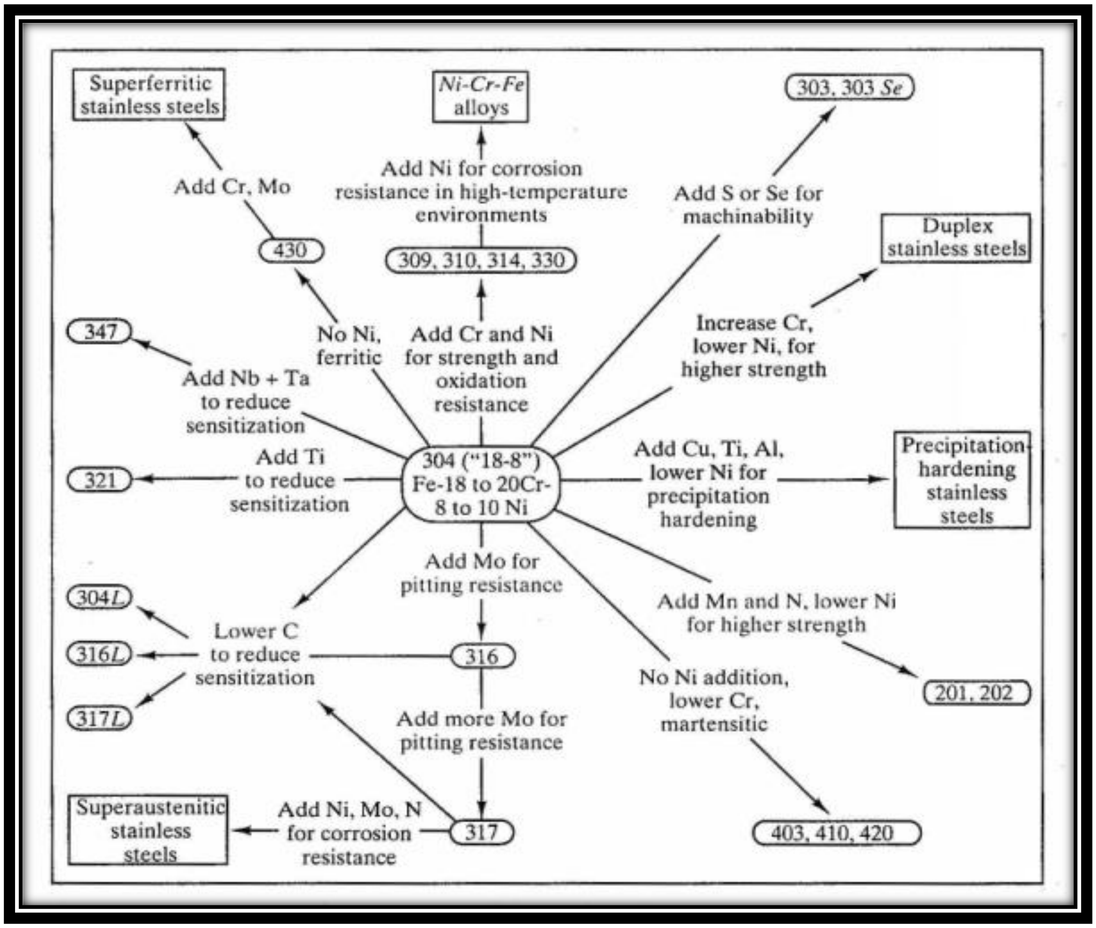

**Fig 1.4 Compositional and Property Diagram for Austenitic Stainless Steels**

(Image Source: Web Reference: Img186, 2013)

The dependency of 0.2 proof stress and tensile strength on the amount of alloying elements is given by empirical relations given in Equations 1.3 and Equation 1.4 respectively.

0.2% proof strength ($MNm^{-2}$) = 15.4 [4.4 + 23 (C) + 1.3 (Si) + 0.24 (Cr) + 0.94 (Mo) + 1.2 (V) + 0.29 (W) + 2.6 (Nb) + 1.7 (Ti) + 0.82 (Al) + 32 (N) + 0.16 ($\delta$-ferrite) + $0.46d^{-1/2}$]

...........................**Eq. 1.3**

$$\text{Tensile Strength (MNm}^{-2}) = 15.4\ [24 + 35\ (C) + 55\ (N) + 2.4\ (Si) + 0.11\ (Ni) + 1.2\ (Mo) + 5\ (Nb) + 3(Ti) + 1.2(Al) + 0.14(\delta\text{-ferrite}) + 0.82t^{-1/2}]$$

............................**Eq. 1.4**

Meanings of the symbols used in these equations are given as, d: mean linear intercept of grain diameter (nm), t: twin spacing (nm), ( ): alloying addition in weight percent (Sedriks, 1996).

The austenitic stainless steels have low stacking fault energy. As a result, twinning occurs in these steels which also affects their tensile properties. The high twinning in low SFE materials increases work hardening and greatly influences tensile strength. Also, the reduced grain size has great effect on tensile strength (known as Hall-Petch effect i.e. as grain size reduces, the tensile strength increases and tensile elongation decreases). The presence of δ-ferrite increases proof and tensile strength by dispersion strengthening effect. Carbon and nitrogen are interstitial solutes and have more solid solution strengthening effect than substitutionally dissolved ferrite-forming elements (Marshall, 1984; Das et al., 2011). The specific role of each of the alloying elements is discussed in Table 1.1.

### 1.4.2 Effect of Strain Rate

During tensile testing, the strain rates play a very important role in determining the properties of austenitic stainless steels. Some researchers have studied the strain rate effects on tensile properties of this material and concluded that as strain rate increases the tensile strength increases but tensile elongation decreases (Park et al., 2010, Kim et al., 2007). The strain rate has different influence on tensile properties of both AISI 304 and AISI 316 in its different ranges. As the strain rate drops under $10^{-5}$ to $10^{-6}s^{-1}$, the high temperature ductility decreases significantly. For the strain rate range from $0.4 \times 10^{-2}$ to 420 $s^{-1}$, as the strain increases tensile strength increases but tensile elongation decreases (Marshall, 1984).

**Table 1.1 Role of Alloying Elements** (Source: Avner, 1998; Singh, 2008; Web Reference: Leffler. 2013)

| S. No. | Alloying Element | Function |
|---|---|---|
| 1. | Chromium (Cr) | Imparts corrosion resistance when present in amount more than 10.5 percent<br>Provides resistance to oxidation at high temperatures<br>Acts as a ferrite stabilizer. Promotes a ferritic structure<br>Increases hardenability<br>Adds some strength at high temperature |

| S. No. | Alloying Element | Function |
|---|---|---|
| | | Resists abrasion and wear (with high carbon) |
| 2. | Nickel (Ni) | Promotes the austenitic structure |
| | | Increases ductility and toughness |
| | | Reduces the corrosion rate in acid environments |
| | | Strengthens unquenched or annealed steels |
| | | Toughens pearlitic-ferritic steels (especially at low temperature) |
| 3. | Molybdenum (Mo) | Increases resistance to general and localized corrosion |
| | | Strongly promotes ferritic structure |
| | | Raises grain-coarsening temperature of austenite |
| | | Deepens hardening |
| | | Counteracts tendency toward temper brittleness |
| 4. | Copper (Cu) | Enhances corrosion resistance in acid environments |
| | | Promotes the austenitic structure |
| 5. | Manganese (Mn) | Improves the ductility at high temperatures |
| | | Stabilizes the ferritic structure at high temperature |
| | | Increases the solubility of nitrogen in austenitic stainless steels |
| | | Counteracts brittleness from the sulphur |
| | | Increase hardenability in-expensively |
| 6. | Silicon (Si) | Increase the resistance to oxidation |
| | | Promotes the ferritic structure |
| | | Used as general-purpose de-oxidizer |
| | | Alloying element for electrical and magnetic sheet |
| | | Increase hardenability of steels carrying nongraphitizing elements |
| | | Strengthens low-alloy steels |
| **7.** | Carbon (C) | Strong austenite former and promotes austenitic structure |
| | | Increases the mechanical strength |
| 8. | Nitrogen (N) | Very strong austenite former and promotes austenitic structure |
| | | Increases resistance to localized corrosion |
| 9. | Titanium (Ti) | Strong ferrite and carbide former and promotes ferritic structure |
| | | Increases resistance to intergranular corrosion |
| | | Reduces martensitic hardness and hardenability in medium-chromium steels |

| S. No. | Alloying Element | Function |
|---|---|---|
| | | Prevents formation of austenite in high-chromium steels |
| 10. | Niobium (Nb) | Strong ferrite and carbide former and also promotes ferritic structure<br>Improves resistance to intergranular corrosion and enhances mechanical properties at high temperatures |

### 1.4.3 Effect of Cold Working

As the extent of cold working increases, the strength increases but ductility decreases. On cold working, the austenite present in the structure transforms to martensite. The formation of martensite increases the strength at the cost of ductility. As percentage of cold work increases grain size also decreases which gives the Hall-Petch strengthening. Also, the work hardening rate increases with increased cold working, which also increases tensile strength. The tensile elongation decreases because the movement of dislocations is restricted by reduced grain size (Marshall, 1984).

## 1.5 SUMMARY OF THE CHAPTER

This chapter provides the basic information about the austenitic stainless steels, commonly used grades of austenitic stainless steels and the effect of various factors on the tensile behavior of these steels. The present work includes the analysis of the effect of grain orientation on the deformation behavior of AISI 304L austenitic stainless steels. In the latter part of this study, strain induced α’- martensite transformation in bi-modal type austenitic grains during tensile deformation is also discussed.

The second chapter discusses some basic terms regarding the deformation phenomenon and presents the review of the literature discussed by various authors related to this work.

# CHAPTER 2

# REVIEW OF LITERATURE

## 2.1 GENERAL

This chapter is divided into two main parts. The initial part of the chapter discusses the deformation mechanisms in polycrystalline materials with emphasis on plastic deformation of FCC materials. The latter part of the chapter reviews the existing academic writings in the subject area. The review of literature relates to the deformation behavior and tensile properties of various austenitic stainless steels grades by several ex-situ and in-situ techniques.

## 2.2 DEFORMATION MECHANISM IN POLYCRYSTALLINE MATERIALS

The properties of several materials are dependent on their plastic deformation behavior which in turn depends on their crystal structure. Plastic deformation of materials depends on how the atoms are arranged and how many number of slip systems, defects (point, line, planer or three dimensional), stacking faults (SFs) are present in a particular crystal structure. As the hindrance to dislocation (line defect) movement in crystal structure increases, more work hardening effect is observed which leads to some great properties in materials. This study is an attempt to correlate the properties of the working material to its microstructure which is changing on the application of tensile loading. Slip, twinning and stacking faults are the main plastic deformation phenomenon which can be observed. This work is related to austenitic stainless steels of grade AISI 304 having face centered cubic FCC crystal structure.

### 2.2.1 Dislocations

Dislocations play a very important role in the deformation phenomenon of crystalline materials. Dislocations are actually two dimensional line defects which are very important in plastic deformation (Bacon and Hull, 2001). As dislocations move in a direction, these produce a slip step at the material by sliding of atomic planes on each other. In other words, it can be said that dislocations are the area of disturbed atoms in a material, which separate the slipped and unslipped (or deformed or undeformed) regions in crystals of material (Hertzberg, 1996). There are mainly three types of dislocations which can be observed during the plastic deformation viz. edge dislocations, screw dislocations and mixed of these two. The distance moved by one dislocation in the direction of slip is called a burger vector (b). The basic type of dislocations which were first observed during plastic deformation of materials were the edge dislocations. The burger vector and the direction of applied shear stress are perpendicular to the dislocation line in edge dislocations (Dieter, 1988). The second important dislocations are screw dislocations. In these type of dislocations, the burger vector, applied shear stress and dislocation line are parallel to each other. In FCC crystals, slip occurs mainly due to the edge dislocations (Abbaschian et al., 2009; Xu et al., 2012). Figure 2.1 shows the edge dislocation in a crystal lattice.

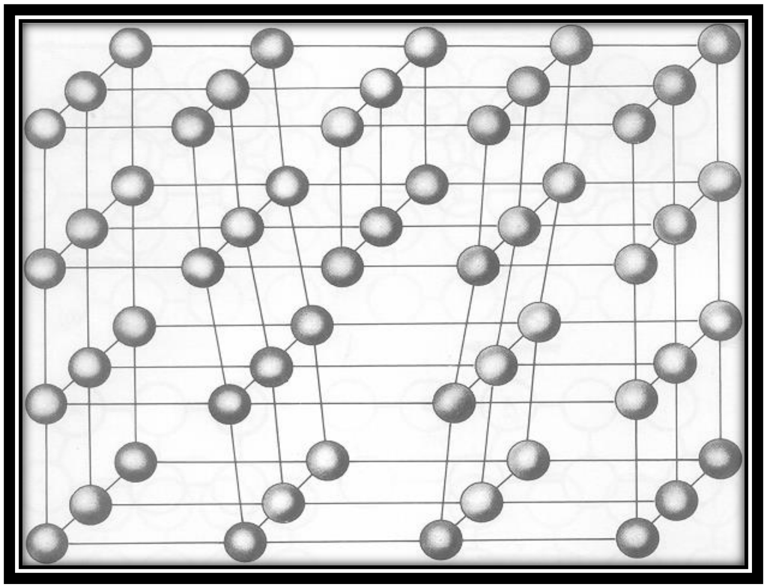

**Fig. 2.1 Edge Dislocation** (Image Source: Felbeck and Atkins, 1996)

### 2.2.1.1 Intersecting Dislocations

The restriction to dislocation motion produces work hardening effects which are important to discuss with regards to plastic deformation in the materials. The restriction caused by a dislocation to another dislocation results in large breaks in dislocation (in single or both) leading to large work hardening effects (Abbaschian et al., 2009).

There are mainly two types of breaks or dislocation intersections:

A) Jogs

B) Kinks

**A) Jogs**

Jog is mainly a dislocation intersection which results in a break in dislocation by another dislocation and takes away a part of the dislocation in another plane. If the two dislocations are moving at planes perpendicular to each other and the burger vectors of both dislocations are also perpendicular, the jog will be produced only in one dislocation whose burger vector will be normal to other dislocation. Also, jogs are produced by the intersection of two screw dislocations and intersection of one edge and one screw dislocation (Hertzberg, 1996; Bacon and Hull, 2001). Figure 2.2 shows the jog produced by two dislocations moving at reference planes perpendicular to each other with their burger vectors also normal to each other.

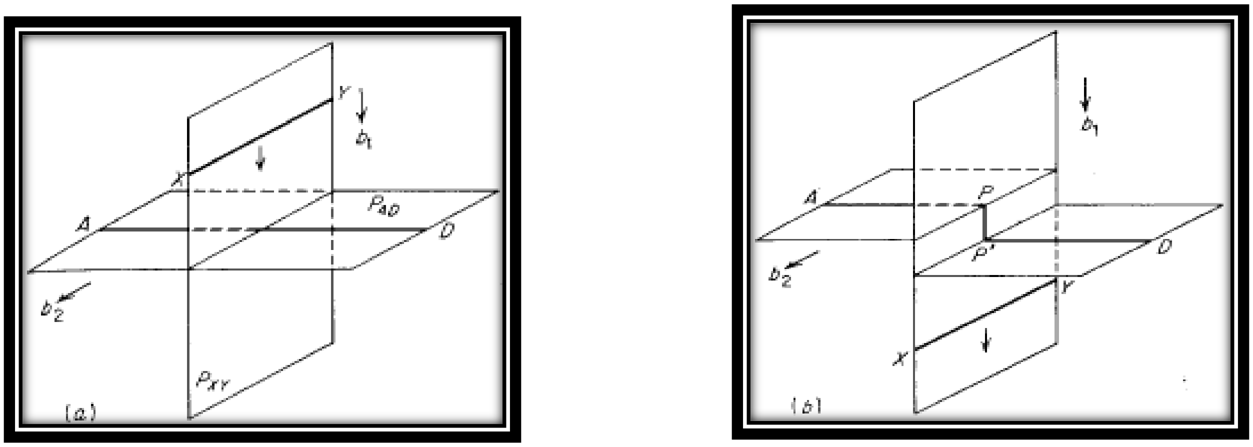

**Fig. 2.2 Jog by Intersection of Two Edge Dislocations** (Image Source: Dieter, 1988)

### B) Kinks

The break ups introduced in dislocations with intersection of dislocations, with the orientations in the same slip planes in which their dislocations lie are called kinks. If the burger vectors of both intersecting edge dislocations are parallel, then the kinks are produced in both dislocations and burger vectors of both dislocations will be normal to the intersecting dislocations. Kinks are also produced by intersection of one edge and one screw dislocation. Kinks are produced on the same planes of their dislocations. As a result, annihilation occurs on their further movement leading to their stability only to a small time (Dieter, 1988). Figure 2.3 shows the kink produced by two dislocations having parallel burger vectors.

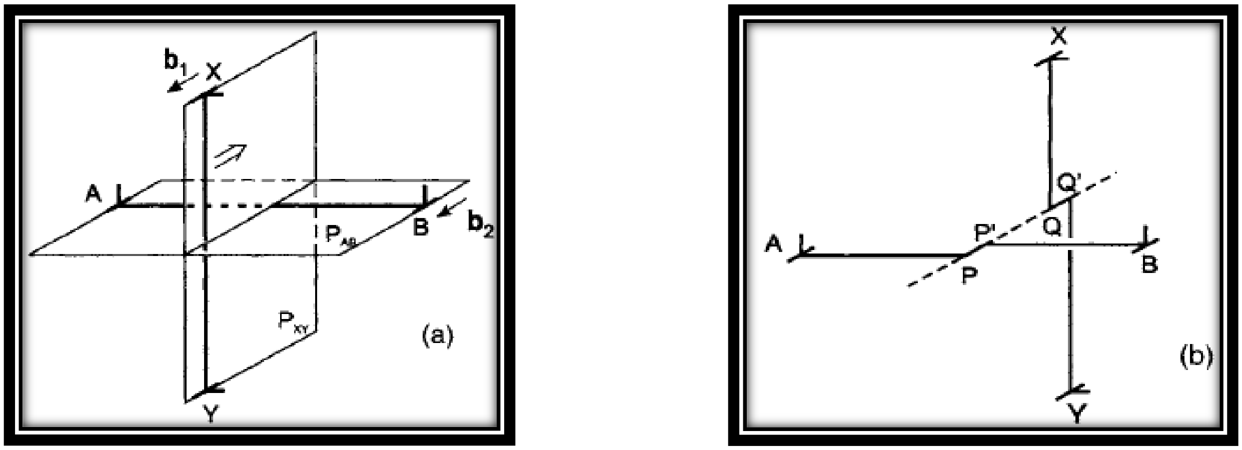

**Fig. 2.3 Kink Produced by Two Dislocations** (Image Source: Bacon and Hull, 2001)

### 2.2.2 Slip

In the phenomenon called slip, one atomic plane slides over the other to discrete multiples of one full atomic distance. Slip occurs in a preferred slip system (slip plane and slip direction). The slip plane is the plane with highest dense atomic packing and slip directions are directions with most closely packed atoms i.e. in the lowest energy directions (Hertzberg, 1996; Callister, 2007). Two types of slip can occur generally in materials. One is glide or conservative in which the dislocation moves in certain line and direction in the same plane and causes deformation. The other is climb or non-conservative type which moves from one plane to another (Bacon and Hull, 2001). In FCC crystal structure, there are 8 planes in one unit cell. The planes at opposite faces of octahedron are parallel. So total four {111} slip planes are there and three <110> slip directions (excluding reverse slip directions) are taken; so a total of 12 slip systems are available for slip to occur. The atoms in slip planes in FCC are closely packed as compared to BCC crystal structure; so in FCC materials slip occurs easily (Dieter, 1988; Abbaschian et al., 2009).

#### 2.2.2.1 Critical Resolved Shear Stress

The primary slip system is one having the highest value of critical resolved shear stress (CRSS). The shear stress required causing slip in a particular plane and direction is called critical resolved shear stress (CRSS). This stress value produces a large number of dislocations to move to attain a measurable strain. CRSS is calculated by the relation **[$\tau_R = P/A \sin\chi\cos\lambda$]**, where **$\tau_R$** is critical resolved shear stress, **P** is applied load, **A** is area and **$\sin\chi\cos\lambda$** is schmid factor (m)**.** As schmid factor increases for a particular plane, the CRSS increases on that plane and slip starts causing plastic deformation. As the number of defects increases in the crystal structure, CRSS increases (Dieter, 1988; Meyers and Chawla, 2009; Abbaschian et al., 2009).

### 2.2.3 Twining

Twinning is another mechanism of plastic deformation in crystalline materials. The twinned portion introduced under the shear force is a mirror image of the untwined portion of the crystal. In twinning, the twin dislocations change the orientation of twinned part of crystal under the shearing force. The twin plane is the plane of symmetry between twinned portion and original parent crystal. Twinning is different from slip phenomenon in the manner that in slip the atoms move to multiples of full atomic spacing but in twinning the movement is very small than atomic spacing. In twining, the rotation of crystal takes place but in slip phenomenon, the atoms do not go under any rotation of crystal. Twins are often seen in low stacking fault energy (SFE) crystal structures like FCC during plastic deformation (Hertzberg, 1996; Dieter, 1988; Bacon and Hull, 2001).

### 2.2.4 Stacking Faults

The perfect crystals are composed of atomic layers in a regular pattern. This sequence of regular pattern of layers is called stacking sequence. This stacking sequence in BCC crystals (ABABAB….) and FCC crystals (ABCABC……) is different. Stacking faults (SFs) are planer two dimensional defects associated with change in the stacking sequence. Stacking faults are produced in crystals with either sliding of an existing layer or introduction of a new layer of atoms. The first type of stacking fault in which one layer of atoms is slid from its position and changes the stacking sequence is called an intrinsic stacking fault. The second type of stacking fault in which a new layer of atoms is introduced in stacking sequence (which does not belong to the continuing pattern) above and below the pattern is called an extrinsic stacking fault. The intrinsic type stacking fault puts one break while extrinsic type puts two breaks in the stacking sequence. The energy associated with the stacking faults per unit area is called stacking fault energy (SFE) (Dieter, 1988; Bacon and Hull, 2001; Abbaschian, 2009).

## 2.3 PLASTIC DEFORMATION OF FCC MATERIALS

The deformation in face centered cubic (FCC) crystals is mainly due to slip and twinning phenomenon. The predominant plastic deformation mechanism is slip. In FCC crystal structure there are 12 potential slip systems, on which slip can occur. The primary slip system is one having the highest value of critical resolved shear stress. At the instant of a particular deformation, Schmid factor is high (means critical resolved shear stress is high) for a particular slip system and deformation by slip is predominant in that slip system. When the critical resolved shear stress becomes higher on some other plane, the slip starts in that plane. In FCC crystal system there can be more than one slip planes that have same value of critical resolved shear stress. Thus, in this case, duplex or multiple slip comes into picture. Due to duplex slip on the intersecting slip systems interaction of dislocations is there which produces more strain hardening effect (Dieter, 1988; Xu et al., 2012).

The austenitic stainless steels with FCC crystal structure appear with dislocations (pile ups and interactions) and stacking faults (SFs) at low deformations, which are due to the low stacking fault energy of these materials. The low SFE leads to high stacking faulted regions which grow on deformation and restrict the motion partial dislocations due to the large width of faulted region. As the deformation increases, the stacking faults start overlapping and result in the formation of twinned regions, which further restrict the motion of dislocations and produce a large work hardening effect. After slip, the second important deformation mechanism is twinning. Twinning generally occurs when critical resolved shear stress for slip to occur is very high (Raghvan, 2006). The twin emitted sections from grain boundary lowers the energy of random grain boundaries and transforms them to low energy coincidence site lattice (CSL) boundaries which resist the percolative phenomenon and also increase ductility (Hertzberg, 1996; Shimada et al., 2002; Bi et al., 2003; Tsurekawa, 2006; Abbaschian, 2009). Austenitic stainless steels under deformation show transformation of austenite to martensite which show twinning due to low SFE which affects their properties significantly. The transformation induced plasticity (TRIP) effect can also be observed in austenitic stainless steels having high stacking fault energies (SFE) by addition of some elements like copper and aluminum etc. This increment in stacking fault energy (SFE) delays the martensite transformations up to high deformations resulting in higher ductility (Rocha and Olieveira, 2009). TRIP effect is also observed in AISI 304 steels during tensile cyclic loading and unloading (Xu et al., 2012). Also austenitic stainless steels, show twinning induced plasticity (TWIP) effect, which is due to the stacking faults generation (low stacking fault energy) on increasing deformation and leads to twin formations which also results in delayed necking, resulting in increased ductility (Allain et al., 2004).

## 2.4 EFFECT OF GRAIN ORIENTATION ON STAGE-I DEFORMATION OF FCC MATERIALS

Stage-I hardening in FCC materials is described as the deformation by easy glide of the dislocations. This stage of deformation is attributed to very low strain hardening of the material and can account for shear strain maximum up to 40%. During the deformation, the grains with orientations in the soft region at centre (means nearly [123] orientation) and near [101] pole of stereographic triangle initially deforms with unit slip system activated due to high Schmid factor in these regions.

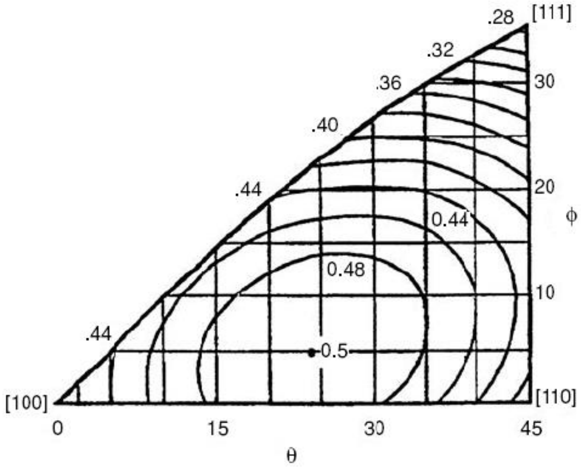

**Fig. 2.4 Contours of Constant Schmid Factors in FCC**

(Image Source: Hosford, 2005)

High Schmid factor areas in the stereographic triangle are shown in Figure 2.4. Soft and hard regions of stereographic triangle and number slip systems activated in different regions of Stereographic Triangle are shown in Figure 2.5 (a & b). The soft region is the region at which the unit slip system gets activated during deformation and strain hardening is absent and the hard regions are the regions where multiple slip systems get activated during deformation and strain harden the material.

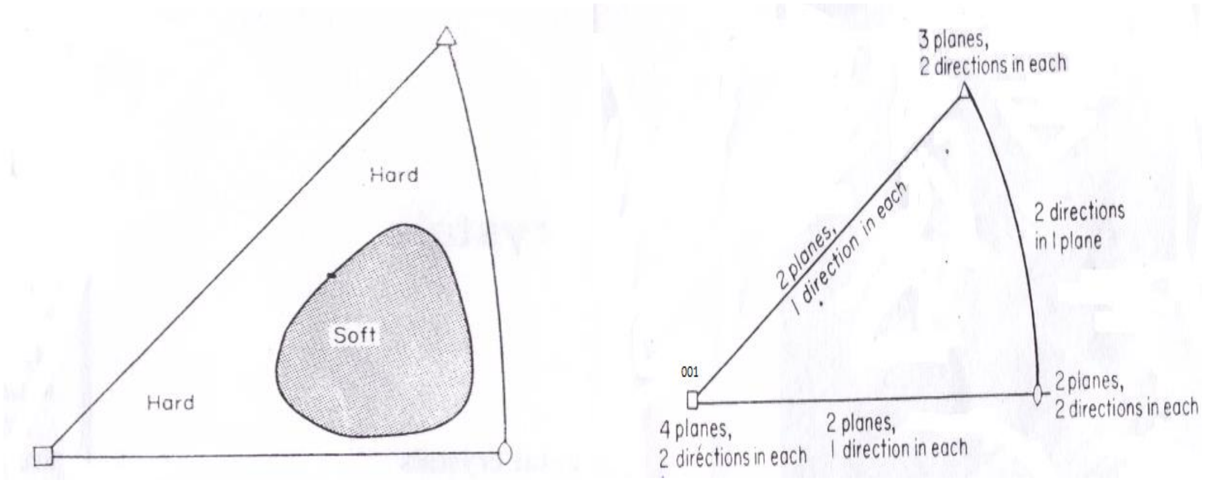

**Fig. 2.5 a) Hard and Soft Regions of Stereographic Triangle b) Slip Systems activated in different regions of Stereographic Triangle**

(Image Source: Honeycombe, 1968)

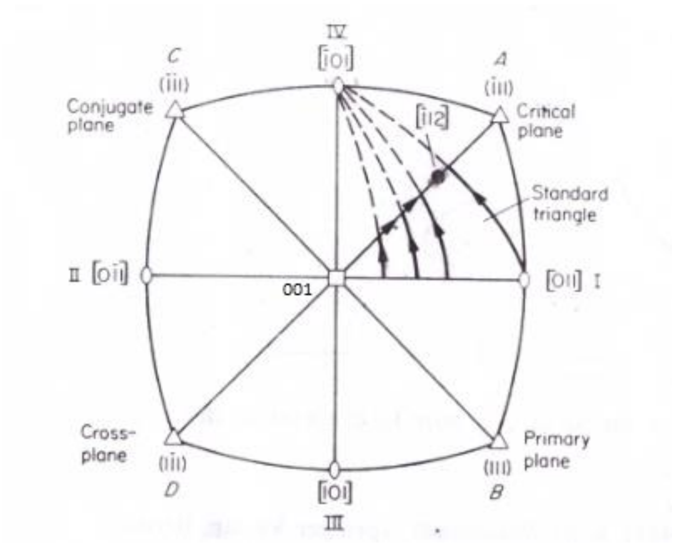

**Fig. 2.6 Rotation of Grains lying in different regions of the Stereographic Triangle**

(Image Source: Honeycombe, 1968)

When the material is subjected to deformation, rotation of the grains lying in the soft area (having high Schmid factor of the stereographic triangle) start to rotate towards the [101] orientation but become stable at the orientation [112] at the [001]-[111] boundary. The direction of rotation of the grains lying in the stereographic triangle is shown in Figure 2.6.

## 2.5 MARTENSITIC TRANSFORMATION

Martensitic transformation in highly stable/alloyed austenitic stainless steels (ASSs) is a very important phenomenon to decide the properties of steel. Martensitic transformations in these steels increase strength at the cost of ductility. In low alloyed or metastable austenitic stainless steels the martensite start temperature ($M_s$) is above room temperature, so matensite is formed during solution treatments. However, the transformation of austenite to martensite in highly alloyed austenitic stainless steels which are very stable can be achieved by refrigeration, quenching effects etc. In some of the highly stable steels, deformation induced martensite start temperature ($M_d$) is above room temperature, so in these steels, austenite to martensite transformation can be achieved by deformation. The austenite phase can be transformed into two types of martensite: α'-martensite with body centered cubic (BCC) structure and ε-martensite having hexagonal close packed (HCP) structure. Many researchers have paid great attention to transformation of austenite to martensite in several materials and have found that ε-martensite is an intermediate phase in transformation from austenite (γ) to α'-martensite. Further, researchers have reported that during shear-induced process, nucleation of α'-martensite starts generally at faults like twin boundaries, shear bands, stacking faults, at laths of ε-martensite and grain boundary triple points. It has also been observed in literature that with increased deformation percentages, the martensite content in microstructure also increases. As strain rates increases during deformation, the temperature of material system rises above the martensite start temperature ($M_s$) and suppresses martensite formation. In low stacking fault energy (SFE) materials, the slip bands, twins, shear bands, stacking faults etc form at lower deformation percentages and lead to formation of martensite in large amounts (Das and Tarafder, 2009; Das et al., 2011).

## 2.6 REVIEW OF LITERATURE

**Staudhammer et al. (1983)** investigated the transformation of strain induced α'-martensite in AISI 304 austenitic stainless steel during tensile deformation in-situ transmission electron microscopy. The material used for the study was deformed 304 stainless steel sheet in the mill annealed condition with a thickness of 0.178 mm. The nominal composition of the material was as: Cr-18.12, Ni-8.60, Co-0.2, Cu-0.14, Mo-0.14, W-0.14, C-0.055, and Fe-balance (all in wt. %). Grain size of the material used was 15μm which was in ultrafine grained (UFG) regime. The transformation was introduced by various modes of deformation, including low strain rate testing, high strain rate testing and explosive shock loading. Tests were performed at room temperature and over a range of lower temperature extending to near 5 K. Strains were measured after testing by measuring the residual formation. Transmission Electron microscope (TEM) observations were also performed. Results showed that the nucleation of martensitic phase was observed at low strains but large volume fraction martensite phase was observed at strains greater than 20%. The formation of martensitic embryos of size (~50–70A$^o$) was observed at pile-ups and shear bands at small strains. The coalescence of the small martensitic embryos above 20% strain was observed and the morphology of the phase was changed to blocky irregular type. Morphology of the martensite was invariant with respect to strain rate and strain state, only the number of dislocation interaction and the size of faulted arrays altered. The main conclusion of the study was that strain induced α'-martensite transformation was observed in the small grains; however slip mediated plastic deformation is a necessary condition for generation of nucleation sites which was very limited for UFG materials.

**Shimada et al. (2002)** examined the effects of process parameters like pre-strain, annealing temperature, time, etc. on the grain boundary character distribution (GBCD) and intergranular corrosion in thermomechanical treatment (during grain boundary engineering) of type 304 austenitic stainless steel. The material used in this study was type 304 austenitic stainless steel having composition as: Cr-18.28, Ni-8.48, Si-0.60, Mn-1.0, C-0.055, P-0.029, S-0.005, and Fe-balance (all in wt. %). The initial size of the base material specimen was 9×10×35 mm$^3$. The specimens were solution-heat-treated at 1323 K for 0.5 h. Thermomechanical treatment was performed by cold-rolling and subsequent annealing. The roll reduction ratio in thickness as pre-strain was varied from 0 to 60%. The pre-strained specimens were annealed at various temperatures from 1200 to 1600 K and quenched in cold water. The GBCD was examined by orientation imaging microscopy (OIM). The tested specimens were observed by scanning electron microscopy (SEM). OIM observations of the thermo mechanically treated specimens showed the effect of the roll reduction ratio on the frequency of CSL boundaries. The effect of annealing temperature at 5% pre-strain on the GBCD was examined by OIM. Annealing at 1400 K and higher temperatures did not result in any better differences in GBCD compared with that at 1300 K, but a favorable change in GBCD was observed during annealing at 1200 K, i.e. with increase in the annealing time at 1200 K, a high CSL frequency layer (about 85% CSL) was formed near the rolled surface and expanded into the specimen. A uniform distribution of the high CSL frequency area was achieved in the r5% specimen annealed at 1200 K for 72 h. The surface appearances revealed that the grain dropping due to intergranular corrosion was depressed in the strain annealed specimens, especially in the r5%–1200 K–72 h specimen with the optimized GBCD. These results verified that the optimum GBCD involving the homogeneously distributed high CSL frequency and the consequent discontinuous distribution of random boundaries can create a high resistance to intergranular corrosion in the material.

**Bi et al. (2003)** examined the difference in chromium depletion between a low-energy segment and an original random boundary in a thermo-mechanically treated 304 stainless steel by analytical transmission electron microscopy (TEM), in order to elucidate the mechanism of high intergranular resistance in a twin-induced grain boundary engineered material. The material used in this study was a type 304 austenitic stainless steel having chemical composition (wt %) 18.28 Cr, 8.48 Ni, 0.60 Si, 1.00 Mn, 0.055 C, 0.029 P, and 0.005 S. The specimen was solution heat treated at 1323K for 0.5h and subjected to 5% cold-rolling. The pre-strained specimen was annealed at 1300K for 0.5h, followed by quenching in cold water and then sensitized at 923K for 1h. Micro chemical analysis of grain boundary regions with a transmission electron microscope (TEM) system (equipped with an energy dispersive X-ray spectroscope) was performed. The grain boundary crystallographic orientations were determined by electron diffraction patterns and grain boundaries were characterized on the basis of CSL theory. Annealing twins were frequently observed in a thermo-mechanically treated specimen. The TEM micrograph showed a low energy segment introduced by twin emission into a random boundary. The random boundary had $Cr_{23}C_6$ precipitates, but the $\Sigma 13b$ CSL segment was free of precipitation. Severe chromium depletion with minimum chromium concentration of less than 12% was observed at the random boundary, while no chromium depletion was detected at the twin boundary. Formation of an annealing twin introduced a low energy segment into the random high angle boundary and sometimes resulted in low $\Sigma$ CSL boundary structure. This study showed that low-energy boundary segment suppresses chromium carbide precipitation and subsequent chromium depletion along the segment. Therefore, it was concluded that the frequent introduction of low-energy segments in the grain boundary network during twin-induced GBE disrupts the continuity of chromium depletion along the random boundary network and arrests the percolation of intergranular corrosion from the surface of grain boundary engineered 304 stainless steel.

**Schino and Kenny (2003)** conducted a study to examine the relationship between microstructure and mechanical properties of high nitrogen austenitic stainless steel with ultrafine grained structure obtained by means of cold rolling and subsequent annealing. The high austenitizing potential of nitrogen allows the nickel content in the steel to be reduced, offering additional advantages such as cost savings. Samples of industrial hot rolled steel were cold rolled with 80% cold reduction and then annealed. The effect of annealing temperature on the grain size was shown at T=900$^0$C, 1000$^0$C and 1100$^0$C. Results showed that for temperatures higher than 900$^0$C, grain boundary diffusion is activated with a consequent grain growth, while for 900$^0$C, the grain mean radius is almost constant with time. Annealing at this temperature showed the possibility of obtaining 2.5-µm. The effect of grain refining on ductility of both the high nitrogen and standard ASI 304 steel was shown. The ductility of high nitrogen (HN) steel was lower than that of AISI 304 stainless steel, and in both the steels, it was reduced by decreasing grain size. Finally, the effect of grain refining on the elastic modulus of the HN steel in comparison to AISI 304 stainless steel was reported. In both cases, the Hall-Petch relationship was found to hold good for elastic modulus behaviour as well as the yield strength in both type of steels. However, a stronger dependence of elastic modulus was found for high nitrogen steel than for AISI 304 steel. The conclusion of this study was that the dependence of tensile yield strength, ductility and the elastic modulus of the steel in the grain size followed the Hall-Petch relationship throughout the full analyzed range.

**Allain et al. (2004)** proposed a physical model of twinning induced plasticity (TWIP) effect in a high manganese steel. An austenitic (Fe–22 wt. % Mn–0.6 C wt. %) steel was used in this study which exhibited a low stacking fault energy (SFE) at room temperature. This rather low value promoted mechanical twinning in competition with gliding along with strain. This low value of SFE promoted mechanical twinning which resulted in high hardening rate that delayed necking, (this hardening effect due to twinning was attributed as twinning induced plasticity effect). The proposed modeling of the mechanical behavior introduced the formation of mechanical microtwins in a viscoplasticity framework based on dislocation glide at the mesoscopic scale in the case of a simple tensile test. In this study, authors particularly observed multiscale organization of twinning and orders of magnitude. The important parameter was the mean free path of the dislocations between twins, whose reduction explained the high hardening rate. Tensile tests were carried out at room temperature after pre strain at 673 K. The plot of elastic limits versus the pre-strain at 673 K was used as the stress–strain curve. The whole modeling including twin was then correlated with the experimental results at room temperature. The modeling also predicted the evolution of the deformation microstructure during loading at room temperature. The parameters for gliding were first fitted on results at intermediate temperatures (without twinning), and the whole modeling was then correlated at room temperature. The simulation was carried out using an easy-to-use homogenization law to deal with the polycrystals. Finally, it was concluded that the proposed modeling allowed successfully highlighting of the link between the mechanical and the microstructure properties (TWIP effect).

**Nagy et al. (2004)** investigated deformation induced martensitic transformation in metastable austenitic stainless steel. The thermomechanical treatment of stainless steels was investigated by tensile tests over a wide temperature range below the room temperature. The composition of the steel was C-0.04, Si-0.45, Mn-1.42, P-0.042, S-0.01, Cr-18.93, Ni-10.77, Ti-0.16, Mo-0.18, and Fe-balance (all in wt. %). The material was machined to cylinders with a diameter of 7 mm and a length of 100 mm (without the clamping heads). The cylindrical samples were loaded at 20, 0, −20, −40, −60, −80, −100 and −120°C temperatures up to the maximum uniform strain. Phase analysis was performed by using X-ray diffraction and magnetization measurements. Tensile tests results showed that, by decreasing the test temperature, the elongation was strongly increased while the hardening was slightly increased (20 to−20°C). On the other hand, below −40°C test temperature, the increase in strength was accompanied by a decrease in elongation. X-ray diffraction results showed that the formation of ε and α’ took place at the same time and by decreasing the test temperature, the amount of α’ martensite strongly increased on each section while the ε martensite slightly increased on the longitudinal surface. From the results it was also found that the γ to α’ and γ to ε transformations took place at higher temperature range (above −80°C) while ε to α’ transformation started below −80°C. From the results, it was concluded that due to the thermo-mechanical treatment, a well-defined texture view was formed in both austenite and α’ martensite phases and it was independent of the test temperature and the γ to α’ started along the austenite {2 2 0} plane to its detriment. It was also stated that the higher elongation of samples having a temperature of 0°C was caused by the appearance of ε and α’ phases.

**Chia et al. (2005)** verified the experimental results with those obtained from Hall-Petch equation regarding effect of grain size on flow stress for β-Ti-15.2at.% Mo alloy. The authors observed that the parameter $\sigma_i$ (lattice friction stress) increased with $\varepsilon$ (strain) and decreased with $T$ (temperature) whereas $K_{H\text{-}P}$ was found to be independent of strain and temperature. The study also verified the effect of d (grain size) on σ (flow stress) and ρ in the β-Ti alloy. It was observed that σ was inversely proportional to $d^{-1/2}$. There occurred an increase in ρ (dislocation density) with increase ε (strain) and decrease in d (grain size). The authors gave the relation, $\sigma = (0.5\text{-}0.6)M\mu b\rho^{1/2}$; M (Taylors's Factor) = 3. The value of ρ for a given ε and d was observed to be relatively independent of temperature in the range 300 to 650 K. There were three mechanisms for increase in dislocation density with decrease in grain size. The results in the study were in accordance with Li's grain boundary ledge mechanism for the effect of grain size on the flow stress.

**Chowdhury et al. (2005)** investigated the evolution of microstructure, texture analysis and the reasons thereof in a 316L austenitic stainless steel during cold rolling. The 316L austenitic steel samples, after hot rolling and solution annealing at $1100^0$C showed a fully austenitic structure (observed through diffraction analysis) with an average grain size of 100 µm. The samples after 20% cold rolling showed inhomogeneous presence of slip bands in some of the grains. After 80% reduction, the grains were elongated to such an extent that they showed a fibrous structure. This indicated extensive homogeneous deformation and showed the presence of shear bands within this fibrous structure. Deformation after 40% cold reduction showed accumulation of dislocations in the form of bands. The authors considered that it might be the beginning of formation of lamellar structure. Rolling texture of FCC materials was very much dependent on the composition and temperature of deformation. One major parameter governing the above two factors was Stacking Fault Energy (SFE). The deformation textures formed by cold rolling in FCC metals could be divided into two groups: (i) High SFE leads to copper or pure metal type texture and (ii) Low SFE leads to brass or alloy type texture. There were some conclusions: a) The 316L stainless steel exhibits a well-defined brass type texture from 40% cold rolling reduction and b) This formation of brass type structure was correlated with the formation of twinning in the material. Twinned fraction was increasing with increase in the strain.

**Li et al. (2006)** investigated the tensile behavior of FCC Ni–Fe alloys within three grain size regimes i.e. >100 nm, 15–100 nm, and < 15 nm. Four deposits of pure Ni, Ni–6% Fe, Ni–15% Fe and Ni–20% Fe alloys (wt.%) were formed using electrode position technique (a powerful technique to produce nanostructures). The sulfur impurity level in deposits was analyzed using a carbon–sulfur analyzer, which employed the combustion method with infrared detection. Dog-bone shaped specimens were used for tensile tests at a nominal strain rate of $10^{-4}$ $s^{-1}$ at room temperature. Microstructural analysis and fracture surface examinations were conducted using transmission electron microscopy (TEM) and scanning electron microscopy (SEM). The results showed that compositional distribution of the electrodeposited Ni–Fe alloys was homogeneous throughout the whole deposit. The sulfur in the deposits was measured to be less than 100 ppm (parts per million by weight). X-ray diffraction analysis further revealed that the Ni–Fe alloys had a single FCC phase (a complete solid solution of Fe into Ni). The results of TEM demonstrated that the grain size distributions of the Ni–15% Fe and Ni–20% Fe alloys were much narrower than those for the low iron alloy and pure Ni, which was due to the addition of the alloying element. The grain size ranges were 3–30 nm and 5–50 nm for the Ni–15% Fe and Ni–20%Fe alloys respectively and the pure Ni and Ni–6%Fe alloy had quite wide grain size distributions of 5–155 nm and 5–305 nm respectively. The calculated mean grain sizes were approximately 44 nm, 53 nm, 21 nm, and 9 nm for pure Ni, Ni–6% Fe, Ni–20% Fe, and Ni–15% Fe alloys respectively. The characteristics of grain boundaries in nano-crystalline deposits were studied using high resolution TEM. Tensile tests showed that the strengths of all four nano-crystalline deposits were several times higher than their coarse grained counterparts. The results demonstrated that the nano-grained materials strain-harden significantly rapidly in comparison with the micro grained ones which depend on the grain size and stacking fault energy (SFE).  It was found that the coarse grained samples demonstrated necking in both width and thickness directions, whereas the necking took place only along the thickness direction in case of nanocrystalline specimens. Detailed TEM analysis revealed that in case of nanostructured alloys, the void size had a scale of several times of the grain size value, suggesting that every void covered many grains; while the voids were usually smaller than the grain size in coarse-grained materials. TEM study also suggested that the void initiation usually occurred at the grain boundaries and triple junctions. In all situations, the fracture surfaces were featured by microvoid characteristics. Detailed analysis showed that, at larger grain sizes, the micro-voids on the fracture surface were real concave voids and the fracture took place in an intragranular manner; while at small grain size, the fracture surface exhibited both the concave and convex features and the fracture model was intergranular. From this study, finally it was concluded that the ductility increased with increase in the grain size.

**Tsurekawa et al. (2006)** quantitatively evaluated the connectivity of grain boundary networks (particularly of random boundaries) on the basis of the percolation theory and assessed the interactive effects of the evaluated parameters on the corrosion properties. A 304L austenitic stainless steel (SUS304L) single crystal was used in this study. The single crystal was cut into rectangular shaped specimens with different orientations (<001>, <101>, <111> and <123>) for compression tests. The specimens were uniaxially deformed to 30% and 40% in strain under compression at room temperature and at a crosshead speed of $4.2 \times 10^{-3}$ mm/s. The deformed specimens were annealed at temperatures ranging from 1200 to 1500 K for 3.6 ks in a vacuum of $2 \times 10^{-3}$ Pa. The grain boundary microstructures of the prepared specimens were quantitatively examined with a scanning electron microscope (SEM) equipped with an orientation imaging microscopy (OIM) facility. The grain boundary microstructural properties such as grain size, grain boundary character distribution (GBCD) and grain boundary connectivity were evaluated on the basis of OIM data. The total length of each random boundary cluster was measured on the basis of OIM data, and was defined as ‘‘the length of cluster’’ by analogy with the percolation theory. The frequency of the resistant triple junctions in the microstructure was also evaluated. The intergranular corrosion resistance for specimens was evaluated using a commonly used ferric sulfate sulfuric acid test after sensitization at 923 K for 2 h and air cooling. Results showed that the in case of recrystallized SUS304L austenitic stainless steel having a low stacking fault energy, the frequency of CSL boundaries increased with increasing grain size because of the multiple twinning during grain growth. An increase of CSL boundary fraction yielded a decrease in the maximum random boundary cluster length. The frequency of percolation-resistant triple junctions increased with increasing frequency of CSL boundaries. The maximum length of random boundary clusters (the maximum length of interconnected random boundary networks) decreased with increasing frequency of CSL boundaries near the percolation threshold, leading to a percolation threshold occurring at approximately 70 ± 5% CSL boundaries and at approximately 35% resistant triple junctions. The connectivity of random boundaries, which were susceptible to intergranular degradation, had a strong influence on intergranular corrosion in SUS304 stainless steel polycrystals. Higher were the resistant triple junction fraction, the more were the SUS304 polycrystals immune from intergranular corrosion.

**Yang et al. (2006)** studied the influence of grain rotation due to slip and Schmid factor on deformation twinning using electron backscatter diffraction technique and Schmid factor analysis. The work aimed to examine the dependence of deformation twinning on grain orientation in a tensile deformed polycrystalline TWIP (Twinning Induced Plasticity) steel. Samples with composition of Fe, Mn: 33%, Al: 2.93%, Si: 3% (wt. %) were melted in vacuum. After forging and solution treatment, tensile samples of 5 mm in diameter were machined and tensile deformed by 20% and 40% at room temperature at a strain rate of $10^{-3}$ $s^{-1}$. The constituent phases and texture were evaluated using an X-ray diffractometer. A scanning electron microscope (SEM) equipped with an electron backscatter diffraction (EBSD) system was used for determination of local orientations. It was seen that despite the high content of 33% Mn, small amounts of the body centered cubic $\alpha$ and hexagonal close packed $\varepsilon$ phases (possibly martensite) were detected. The amount of these phases did not change appreciably with increasing strain. It was assumed therefore that these phases are formed due to the low cooling rate and are not strain induced. Schmid factor contours for slip and for twinning were plotted in the orientation triangle. An assumption of equal critical resolved shear stress (CRSS) for slip and twinning was adopted for the calculations. Calculations revealed that if the CRSS for twinning is 15% higher than that for slip, the region favoring twinning in the orientation triangle will disappear both for tension and compression. A 5% strain was needed before the start of twinning in TWIP steel. As multi-slip and dislocation pile-ups are often prerequisites for twin nucleation, it may be expected that more twinning should be seen for grains with orientations near the edges of the unit triangle than for grains with orientations in the single slip interior region, even considering the higher Schmid factor for twinning in this region. Among the two stable texture components of ‹111› and ‹001› induced mainly by slip during tension, ‹111› was the most frequently detected grain orientation producing twins variants and strong work hardening. Both the crystallographic rotation due to slip and the Schmid factor influence the dependence of deformation twinning on the initial grain orientation.

**Kim et al. (2007)** investigated the deformation mechanism of high nitrogen austenitic stainless steels using tensile loading under various strain rate conditions. Austenitic high-nitrogen 18Cr–14Mn–4Ni–3Mo–xN steels with nitrogen contents of 0.51 wt. % and 0.88 wt. % respectively were used. The steels were received as a hot-rolled plate form and were cold rolled to a thickness of 3 mm. Tensile specimens with a gage length of 25.4 mm were machined from the cold rolled plate. 0.51N and 0.88N-SP (single phase) steel specimens were heated to 1100$^{o}$C while 0.88N-DP (dual phase) steel sample was heated to 1050$^{o}$C. Room-temperature tensile tests of the heat treated specimens were carried out under various strain rate conditions ranging from 5 × $10^{-5}s^{-1}$ to 5 × $10^{-1}s^{-1}$. Tensile curves were obtained and analyzed to find out strain hardening characteristics, yield and tensile strengths as well as elongation. Transmission electron microscopy (TEM) and scanning electron microscopy (SEM) microstructures of the tested specimens were examined to understand the deformation behavior of the steel. Both 0.51N and 0.88N-SP specimens that were heat treated at 1100$^{o}$C had a microstructure composed of full γ (austenite), while 0.88N-DP specimen that was heat treated at 1050$^{o}$C was composed of two phases γ (austenite) and precipitates of $Cr_2N$. The ultimate tensile strength of the 0.51N steel tested at the strain rate of 0.05 $s^{-1}$ was 746 MPa, while that of the 0.88N-SP specimen under the same test condition was 945 MPa. For 0.51N steel the yield strength and flow stress increased with the strain rate increase; however, the increase was not steady. In the case of 0.88N steels, when the strain rate exceeded 0.05$s^{-1}$, the yield strength and flow stresses of the 0.88N-DP steel increased suddenly. The 0.88N-DP steel exhibited higher strength than the 0.88N-SP specimen at the strain rate of $5\times10^{-2}s^{-1}$. However, the failure strain of the 0.88N-DP specimen was lower, which indicated that the nitride precipitates increased the strength of the steel but induced brittleness. However, at the strain rate of $5\times10^{-5}s^{-1}$, the yield and tensile strength of the 0.88N-DP steel was lower than that of the 0.88N-SP specimen, and the elongation of both steels were similar. Compared with the 0.88N steel, the strain rate variation did not particularly change the tensile deformation behavior of the 0.51N steel. TEM results showed that the deformation of the high nitrogen steel was controlled by planar slip and twinning at the initial and later deformation stages, respectively. Finally, it was concluded that the strength of the high nitrogen steel increased with the increase of the nitrogen content. The high-nitrogen steel with the microstructure of single FCC austenite did not show significant strength dependency on strain rates (deformation rate), while the steel with the microstructure of fine nitride precipitates in the austenite matrix exhibited considerable strength dependency on the strain rate.

**Kumar et al. (2007)** studied the effect of thermomechanical processing (TMP) on grain boundary character distribution (GBCD) and the effect of GBCD on tensile properties of 304L austenitic stainless steels (ASS). Solution treated ASS 304L plates were rolled at room temperature for thickness reduction upto 60 and 80 percent. Rolled specimens were annealed at 700$^{0}$C, 900$^{0}$C, and 1000$^{0}$C for 1 hour. Electron backscattered diffraction (EBSD) analysis was carried out in an integrated SEM-EBSD-EDS system. Tensile tests were conducted at room temperature under displacement control at a strain rate of $1.3*10^{-4}$ $s^{-1}$ using a closed loop servo hydraulic dynamic testing system equipped with a digital controller. The starting material showed equiaxed grains of average 85 µm size, whereas 60 percent CR and 80 percent CR ASS showed grain sizes of 90 and 100 µm, respectively, after annealing at $1000^0$C. Cold rolling resulted in deformation of grains, causing elongation of grains along the rolling direction. Complete recovery of the deformed structure occurred at $700^o$C. On the other hand, the annealing temperature of $900^0$C resulted in complete recrystallization of the deformed structure for all cold rolling conditions. The annealing temperature of $1000^o$C induced grain growth for both rolling conditions. However, 80 percent cold rolling followed by annealing at $1000^0$C produced larger grains (<100 µm) as compared to 60 percent cold rolled at $1000^0$C (<90 µm). The SEM-EBSD studies revealed variation of coincidence site lattice boundaries (CSLB) with annealing temperature. The base or solution-annealed starting material showed 15 percent of occurrence frequency of Σ3 type CSL boundaries and cold rolling and annealing were observed to enhance the Σ3 type of CSL boundaries with low fraction or negligible fractions of $\Sigma3^n$ type. 60 percent cold rolled specimen produced increasing fractions of Σ3 CSL boundaries with increasing annealing temperature. The annealing temperature of $1000^o$C produced the highest magnitude of Σ3 CSL boundaries. The fraction of high angle boundaries decreased in TMP condition, even though there was an increase in misorientation distribution of about 60 degree angle. It was observed that with increasing annealing temperature, softening of the ASS increased. The yield strength was found to decrease below that of the starting material. The total percent elongation showed an increasing trend, in the range of 20 to 80 percent, with annealing temperature. Annealing at $700^o$C exhibited reasonably good strength and ductility for 60 percent CR. A remarkable 80 percent elongation at $1000^o$C for 60 and 80 percent CR ASS was much higher than the usual 60 percent elongation observed in this material. In all the TMP conditions, a monotonic increase in the stress with increasing strain was observed in the uniform deformation region. Finally, it was concluded that the thermomechanical processing of 304L ASS introduces special grain boundaries with various misorientation distributions. After TMP, 304L ASS was found to show a decrease in yield strength and an increase in percent elongation. The observed softening in tensile properties could be corroborated with recovery and recrystallization of the cold-worked structure upon annealing. The increase in percent of elongation was found to be influenced by the presence of special boundaries Σ3, whereas the increase in the stain hardening exponent resulted from the presence of preferred orientation of the grains, which is conducive for plastic deformation under the simultaneous operation of multiple slip systems.

**Lee et al. (2007a)** investigated an ultrafine grained (UFG) alloy with nanosized precipitates in order to improve its properties further. Ultrafine grained (UFG) steel with nanosized precipitates was fabricated using strain induced martensite transformation (SIMRT) and microstructure and mechanical properties were investigated. For the study, an ingot (Fe, 0.1% C, 10% Cr, 5% Ni, 7.7% Mn, 0.3% Nb) alloy was prepared in a vacuum induction furnace, hot rolled to 6 mm thickness and was given solution treatment at 1200$^{o}$C for 30 min. The initial microstructure of the solution treated plate was austenite having grain size of about 50µm. The plate was then cold rolled to 70 percent thickness reduction at room temperature. The microstructure of the cold rolled sheet was changed from austenite (γ) to martensite (α’). The cold rolled sheet was then annealed at the reverse transformation finish temperature of α’ to γ ($A_f$) + 10$^{o}$C for 10 minutes in order to transform α’ to γ. The $A_f$ temperature was taken as 654$^{o}$C. From the annealed plate, flat tensile specimens with a gauge length of 14mm, 6mm wide and having thickness 1mm were machined. Uniaxial tensile tests were performed at room temperature with a strain rate of $2.2\times10^{-3}$ $s^{-1}$. The martensitic transformation during the tensile tests was observed by transmission electron microscope (TEM). The results showed that the UFG specimens had high yield stress (860 MPa) and ultimate tensile stress (1140 MPa), which were much higher than the solution treated specimens because of grain refinement. Total elongation to failure and uniform elongation of the UFG specimens was also increased from 33.3 to 35.6 percent and from 30 to 33 percent respectively as compared to coarse grained specimens. From the results, it was concluded that the UFG steel with both Cr and Nb particles had highest yield stress which indicated that the fine nano-sized Nb precipitates had a greater impact on yield stress.

**Lee et al. (2007b)** investigated the deformation twinning in a high-nitrogen austenitic stainless steel, in terms of orientation dependence and formation mechanism. The investigated material was a commercial high nitrogen austenitic P900NMo alloy with the following composition: 17.94Cr–18.60Mn–2.09Mo–0.89N–0.04C–balance Fe (wt. %). Specimens were sealed in a quartz tube under vacuum and were solution-treated at 1150$^{o}$C for 30 min in the austenite single phase region, followed by water quenching. The specimen was uniaxially elongated at room temperature using a semi in situ deformation stage incorporated into a field emission gun (FEG) scanning electron microscope (SEM). Strains at each deformation stage were calculated by measuring the relative displacements of the marked indents in scanning electron microscopy (SEM) images. In order to investigate the orientation dependence of deformation twinning, thin foils for the transverse direction (parallel to tensile axis) of a deformed electron back scattered diffraction (EBSD) specimen with {111}, {110}, and {100} crystallographic orientations were prepared using a FEI dual beam system composed of both focused ion beam (FIB) and high resolution SEM columns. TEM observations were also carried out on the bulk specimens systematically deformed to the same strain as those of semi in situ deformation in EBSD using a conventional tensile testing machine. The deformed microstructure was characterized by planar dislocation array in the low strain region and by stacking faults together with well-developed deformation twinning in the high-strain regime. The deformation twinning showed strong orientation dependence with respect to tensile axis. Following twinning systems were observed in different grains i.e. (i) primary and conjugate twinning system cooperated in the {111} grain; (ii) only one twinning system was activated in the {110} grain; (iii) no deformation twinning was observed in {100} grain. Thus, it was deduced that the partial separation was at its maximum for tensile stresses along {111}. At the early stage of deformation, fault pairs composed of two stacking fault planes and one partial dislocation (heterogeneously nucleated), and grew into overlapping stacking faults, resulting in the formation of deformation twinning. Therefore, it was concluded that the orientation dependence of deformation twinning can also be explained in terms of the degree of dissociation associated with relative shear stress acting on leading and trailing partials.

**Cavaliere (2008)** conducted experiments to study the strain rate sensitivity of ultra-fine and nano-crystalline metals and alloys prepared by severe plastic deformation and electro-deposition method. The materials taken in the study were pure Ti Grade 2 produced by Equal-Channel Angular Pressing (ECAP) with eight passes, pure Cu produced by ECAP with four passes, Ni (20 nm mean grain size) and ultra-fine grain counterpart (270 nm mean grain size), Ni-18 %Fe (20 nm mean grain size) and Co (15 nm mean grain size). It was seen that in the UFG Ti, a strong effect on hardness behaviour was observed with variation in the loading rate. This was due to the stronger effect of SPD on material's grain refinement and strength increase. For pure Ni with grain sizes 20 and 270 nm respectively, it was seen that the same material was more sensitive to strain rate variation when the grain size was decreased demonstrating the strong effect of highly strained grain boundary affected zone (GBAZ). Atoms within this GBAZ were more likely to be involved in the deformation process. This was highly helpful in electro-deposited materials, in that the high rate sensitivity could have a strong effect in the delaying of necking during tensile deformation, hence leading to higher ductility. Another observation was, that for, some nano-crystalline metals and alloys, in fact, dislocations were generated at grain boundaries and this defect-assisted mechanism could be rate-limiting in more stable microstructures, observed in electro-deposited Co and Ni-Fe alloys. Room temperature recovery process in NG/UFG metals is important, because dislocations were generated from closely spaced grain boundaries. They were packed in very close spaces and therefore, the phenomenon of dislocation annihilation was prominent. Such process balances the dislocation generation at grain boundary in a prominent way as the grain boundaries were stable, apparently, leading to lack of strain rate sensitivity.

**Milad et al. (2008)** investigated the various degrees of plastic deformation introduced by cold rolling (CR) at ambient temperature on the tensile properties of AISI 304 stainless steel. Microstructural, ferromagnetic and hardness studies were also conducted. The material used in the work was austenitic type stainless steel 304 with a chemical composition of C-0.058, Mn-2.0, Cr-18.70, Si-0.50, Ni-8.0, S-0.023, P-0.026 and Fe-balance (all in wt. %). The steel plates were sectioned into 175mm×60mm×8mm strips which were solution treated at 1100$^{o}$C for 90 min, and then quenched in iced brine to dissolve any carbides present. Plastic deformation of the solution annealed strips was carried out by cold rolling at ambient temperature and ten percentages of cold reduction were obtained (i.e., 5%, 10%, upto 50%). Tensile testing was carried out at room temperature using a 200 KN full-automatic machine with 5mm/min cross-head speed. Three specimens from each cold work % condition were tested. Results showed that the fracture during tensile testing of all specimens was almost at the center of the gauge length. The role of plastic deformation in the strengthening of this stainless steel was evident and it was found that cold rolling increased the yield and tensile strengths of 304SS by about the same rate. Micro-hardness values were found to increase with cold rolling. The amount of α’ martensite produced by rolling was found to increase with % CR, while the amount of α’ martensite formed during tensile testing was found to be independent of % CR. Thus it was concluded that the net effect on the steel properties was mainly due to the prior martensite i.e. the martensite produced during the cold rolling.

**Das et al. (2011)** examined the austenite to martensite transformation during the tensile deformation of austenitic stainless steels to check if the transformation is stress induced (i.e. the stress provides a mechanical driving force) or whether the generation of defects during deformation helps nucleation of martensite. For the study, experimental data was collected from the published literature on strain induced martensitic transformations in a variety of austenitic stainless steels tested in tension. The martensite start temperature ($M_S$), in the absence of deformation in each case was calculated as a function of the chemical composition, using an empirical relation. Stress versus plastic strain curves were used to convert strain data (in plots of volume fraction of martensite versus plastic strain) into a tensile stress that was then used to estimate the mechanical driving force. The entire data was subjected to neural network analysis which is a method of deciphering the independent roles of stress and strain in stimulating martensitic transformation when both are applied simultaneously. The neural network model was created as a function of all the variables (strain rate, temperature, grain size, stress, stain) with the exception of the volume fraction of martensite, which was its output. The results revealed that the in experiments where martensite was stimulated during a tensile test, it was the mechanical driving force which played a dominant role rather than the strain induced transformation.

**Kobayashi et al. (2011)** investigated the role of grain boundary microstructure on the fatigue crack propagation during cyclic deformation of SUS 304 austenitic stainless steels. For the study, two compact type (CT) specimens named as Type A and Type B were prepared from fully pre-annealed SUS 304 stainless steel sheets that were subjected to cold rolling to 5% and 20% respectively. The specimens were 30 mm wide and 3.0 mm thick. Field Emission-Scanning Electron Microscopy (FE-SEM)/ Electron Backscattered Diffraction (EBSD)/ Orientation Imaging Microscopy (OIM) were applied for quantitative analysis of grain boundary microstructure of pre- fatigued and post-fatigued specimens. Fatigue crack propagation tests were carried out by using a servo-hydraulic machine in air at room temperature and at the load ratio of R = 0.1 and frequency of 5 Hz. In situ observations of fatigue crack propagation were made by using 2D-motion capture system consisting of a Charged Coupled Device (CCD) camera. The average grain size for Type A and Type B specimen was 23 µm and 22 µm respectively. The post-annealed specimens had a high density of annealing twin and had a high fraction of {111}/Σ3 coherent twin boundaries. Type A specimen which was subjected to cold-rolling to 5 % had shown a high fraction of {111}/ Σ 3 boundaries. The total fraction of low- Σ boundaries for Type A and Type B specimen was 73 % (Σ 3: 58 %) and 53 % (Σ 3: 39 %), respectively. The propagation rate of fatigue crack for Type A specimen was lower than that for Type B specimen because the local crack propagation in the Type A was inhibited due to the presence of a higher fraction of Σ3 boundaries (Σ 3: 58 %) as compared to Type B (Σ 3: 39 %). This effect was due to the reason that local propagation rate of fatigue crack along Σ3 boundaries was lower, while the fatigue crack propagation was accelerated when propagating along random boundaries. Therefore, it was concluded that the austenitic stainless steel with fine grained structure and a high fraction of low- Σ boundaries, particularly Σ 3 boundaries, can be endowed with higher resistivity to fatigue crack propagation than conventionally processed specimen of the same material. Thus, grain boundary engineering can be utilized to control the fatigue crack propagation in austenitic stainless steels.

**Kumar et al. (2011)** conducted experiments with 316L austenitic stainless steel to evaluate the microstructure and mechanical properties during the thermal cycling process. The material considered was a solution annealed 316L austenitic stainless steel plate. Multi-pass unidirectional cold rolling with same thickness per pass was performed to a total thickness reduction of the order of 90%. This was followed by cyclic thermal process in the temperature range of 850 to 925$^0$C. Heating rate was kept at 58$^0$C/s. Transmission Electron Microscopy technique was used to see the microstructure of cold rolled specimens. The microstructure of cold rolled specimens exhibited typical elongated and heavily dislocated grains consisting of blocky dislocated tangles and banded structures. The magnetic measurements carried out for depicting the formation of DIM in cold rolled specimens showed its absence, indicating stable austenite phases not inducing DIM by cold deformation. The $M_d$ temperature for the stainless steel in the study was about 18$^0$C, which was below room temperature. It was observed that the evolution of recrystallization fraction was influenced by temperature and time of annealing of specimens. The values of recrystallization volume fraction against the annealing temperatures showed that a sharp increase in recrystallization fraction volume occurs above 900$^0$C. The volume fraction of residual deformed area was observed to decrease with increase in number of thermal cycles. The two step thermal cycling process appeared to be more appropriate for tailoring the grain size subjecting the specimens first at high and then at low temperatures. The study indicated a significant change in tensile properties due to the thermal cycling process. The microstructure with fine recrystallized grains resulted in some drop in yield strength (about 900 MPa) but it was much above as compared to solution annealed coarse grained specimen. The highly deformed structure was the main reason of poor strain hardening ability. The increase in yield strength and decrease in ductility was due to the small grain size. It was observed that the loss in ductility was due to the inhomogeneous deformation.

**Shen et al. (2012)** investigated the microstructure characteristics and deformation behavior of 304L stainless steel during tensile deformation at two different strain rates by means of electron backscatter diffraction (EBSD) and transmission electron microscopy (TEM) techniques. The volume fractions of transformed martensite and deformation twins at different stages of the deformation process were measured using X-ray diffraction method and TEM observations. In this study, authors conducted a series of experimental studies to obtain quantitative measurements on the deformed microstructures and the interactions of different deformation mechanisms at various stages of the deformation process for 304L stainless steel deformed at room temperature under two strain rates. For the experiments, as received steel sheet was cut into the dog bone shaped specimens with a gauge length of 30 mm and a width of 6 mm, with a final thickness of 1.5 mm. Uniaxial tensile tests were performed at two strain rates ($3\times10^{-3}$ $s^{-1}$ and $3\times10^{-1}$ $s^{-1}$) under room temperature. Specimens were deformed to various strain levels and then fully unloaded. Metallurgical cross sections were cut from the gauge of the deformed samples and evaluated for martensite volume fraction, using X-ray diffraction and electron backscatter diffraction (EBSD) analysis. Results showed that the when the strain rate was increased from $3\times10^{-3}$ $s^{-1}$ to $3\times10^{-1}$ $s^{-1}$, the yield stress increased from 300 MPa to 340 MPa, while the ultimate tensile stress decreased from 900 MPa to 850 MPa. X-ray diffraction results revealed that the volume fraction of martensite increased monotonically with increasing strain for both strain rates. At the beginning of the deformation, a monotonic increase in the stress with increasing strain to 1.2% was observed. When deformed to 10% strain, a large amount of lattice dislocations had been generated, accompanied with some stacking faults (SFs). At a strain level of 20%, SFs and martensite had occurred and SFs acted as the precursor of twins and $\varepsilon$ martensite. From a strain level of 30% to 57%, the density of twins and martensite increased with increase in strain. Above the strain level of 57%, the density of martensite further increased but that of twin abruptly decreased with increase in strain. The increment of induced martensite caused the drop in twin density. The loss of twin relationship across their boundaries (due to crystal rotations of the austenitic lattice) was also responsible for the decrease of twin density before fracture.

**Xu et al. (2012)** analyzed the strain induced martensitic transformation in AISI 304 austenitic stainless steel under cyclic tensile loading and unloading, using in situ X- ray diffraction (XRD) technique. For the study, an in situ XRD method was used to study the martensitic transformation during cyclic tensile loading and unloading (CTLU) tension in AISI 304 stainless steel and transmission electron microscopy (TEM) was also employed to analyze the microstructure of the deformed specimens. The specimens were loaded and unloaded at strains of 0.3, 0.4, 0.5, 0.6 and near fracture. An incident X-ray source with a 5 mm wide beam was focused on the center zone of the specimen, which underwent the largest deformation during the tensile process. X-ray diffraction analysis was carried out twice at each strain cycle i.e. during loading as well as unloading conditions. A direct comparison method was utilized to quantitatively determine the fraction of austenitic phase and martensitic phase. It was found that the martensitic transformation started at the first stage of deformation. The tensile specimen showed a parabolic transformation behavior and unloading process had a minor influence on the kinetics of martensitic transformation at small strains (for example, strain at 0.3), while the fraction of martensitic phase showed a sudden increase at unloading points when strain surpassed 0.4. Microstructure observations were performed with transmission electron microscopy (TEM). The martensitic lath was formed at the austenite matrix during deformation and dislocations were found parallel to each other at some distance from the martensitic lath. Results showed that the fraction of strain induced martensite increased due to variation of internal stress and dislocation when unloading occurred. It was also found that the enhanced transformation induced plasticity effect prolonged the time to neck formation to a significant extent. This study also revealed that the martensitic transformation was stimulated by the unloading process under CTLU tension, which observably altered the internal structure involving the internal stress and dislocation configuration.

**Das (2012)** studied the interaction between deformation induced martensite and voids during the tensile deformation of metastable austenitic stainless steel at various strain rates under ambient temperature while keeping the initial inclusion volume fraction constant. Nuclear-grade AISI 304LN metastable austenitic stainless steel was used for the study. The chemical composition (in wt. %) of the material was: C 0.03, Mn 1.78, Si 0.65, S 0.02, P 0.034, Ni 8.17, Cr 18.73, Mo

0.26, Cu 0.29, N 0.08 and the balance Fe. The$M_{d30}$ temperature of the material, at which 50% of the austenite transformed to martensite at a true strain of 0.30 was calculated and found to be 2.746$^{o}$C. The initial austenite grain size of the material was 70 µm. The mechanical properties of AISI 304LN stainless steel at five different strain rates (i.e., 1.0, 0.1, 0.01, 0.001 and 0.0001 $s^{-1}$) were determined through room temperature tensile tests of solid cylindrical specimens. The fracture surfaces of all the samples were analyzed by scanning electron microscopy (SEM). From the broken pieces, several thin slices (1–2 mm width) were extracted from the fracture end up to the uniformly deformed region for all the fractured specimens. The void density fraction was measured for all the slices repeatedly through Archimedes principle. The void population adjacent to the fracture surface was observed by optical microscope and field emission gun electron back scattered (EBSD) imaging. Results showed that the rate of development of the void population with strain was initially low, and then increased rapidly with the high strains on approaching the fracture surfaces. For the same amount of true strain, the void density fraction was found to be higher for the high strain rate specimens as compared to the low strain rate. At lower strain levels, the amount of martensite increased rapidly in a linearly proportional manner, after which the rate of transformation slowed down. In tensile specimens, voids initiated at the martensite–austenite interfaces along the axis of applied stress at the position of maximum tensile stress. Various void sizes were found at higher strains, which suggested both the nucleation and growth of voids. A small number of voids were formed at lower strains by fracture/decohesion of deformation induced martensite (DIM). From the results it was concluded that the there was a systematic correlation of the void density fraction and the martensite volume fraction with the strain rate variation of metastable AISI 304LN stainless steel tested at ambient temperature. DIM acted as a void nucleation site where the initial volume fraction for all the specimens was kept constant. It was also concluded that the void nucleation occurred at lower strains in higher strain rate specimens and vice-versa and the inhomogeneous distribution of DIM in the deformed austenite grains helped to nucleate voids, which grew under the influence of favorable plastic strain and hydrostatic stress.

## 2.7 CONCLUSIONS FROM LITERATURE REVIEW

The austenitic stainless steels are materials of great interest in the present times due to some great mechanical and physical properties. These steels have great ductility up to 80% and also have very good corrosion properties and moderate strength. Many researchers have done work on these steels to improve their mechanical strength. The main problem has been to optimize the strength and ductility combination of these steels. Various researchers have reported literature on the phase transformation in these steels [γ (austenite) → α'-martensite transformation] in terms of the route followed by the transformation and the nucleation sites for martensite formation. Some researchers have reported about the strain hardening in these steels and various phenomenon of deformation like slip and twinning.

### 2.7.1 Gaps in the Literature

- The deformation behavior of austenitic stainless steels just after the start of yielding has not been reported in the literature. It has not been explained as to when the slip phenomenon starts in the material (i.e. at what strain level) and in which type of grains (in respect of grain size). Also no information is available as when the slip type changes from single unit system to the multi-variant type.
- The effect of grain size and interrupted type of tensile deformation on the martensitic transformation is not depicted by the authors.
- Effect of change in grain orientation during stage-1 of deformation on the deformation behavior of the material during tensile deformation has not been discussed yet.
- Effect of twinning regarding to the grain orientation change on deformation behavior during tensile deformation is not explained by researchers.
- The effect of bi-modal type of grain distribution on the martensitic transformation is not described yet.
- The effect of misorientation of the grain boundaries on the strain induced martensitic transformations during tensile deformation has not been described by researchers.
- In-situ scanning electron microscopy (SEM) for the study of tensile deformation behavior of AISI 304L austenitic stainless steel at lower strain values has not been done by any author.

# CHAPTER 3

# DESIGN OF THE STUDY

## 3.1 GENERAL

This chapter of thesis work gives all details of the experimental work done to achieve the desired objective of study. In the very starting, the objective of work has been described clearly in detail. On the basis of objective, the planned experimental design to meet the objective is described step wise step. The machinery and equipment used as a tool for experimental work has been described in brief with model numbers, machine specifications, purposes and operating conditions etc. Material used for study with its specifications is also given. The input variables for goal experiments have also been described.

## 3.2 METHODOLOGY

The study of in-situ tensile deformation at different strain levels was planned in main three phases to achieve the goal with accuracy. The whole study, starting from objective setting and material selection, then sample preparation, followed by experimentation and at the last conclusions drawn from obtained results is designed into the following three phases, with the work planned and importance of all phases step by step.

***Phase 1:*** The first phase comprised of goal setting, material selection for the study, machinery and equipment required, and input parameters to be taken. The input parameters (strain and strain rate) were largely taken from previous research and standards. The operating range of each process parameter has been finalized after its detailed study from the previous research work.

***Phase 2:*** In this phase, a series of experiments have been carried out in order to extract valuable information regarding the alloy. The experiments have been conducted with due concern in the operating range of process parameters (established in the previous phase) and the resulting outputs have been analysed.

***Phase 3:*** This phase discusses the results obtained, the reasons thereof, and draws important conclusions. It also discusses the limitations of the present work and its future scope.

## 3.3 ESTABLISHMENT OF OBJECTIVE FUNCTION

The review of literature for the present thesis work revealed that extensive work has been done on AISI 304L austenitic stainless steels in respect of strain induced martensitic transformations, tensile property enhancement by various processing routes and on other important issues like enhancement of corrosion resistant etc. However, very limited work has been reported on grain orientation changes during the tensile deformation of austenitic stainless steels and its effect on the mechanical properties. Also, the strain induced transformation in bi-modal austenite grains has not been reported by researchers.

*The main objective of the present work is to study the changes in microstructural behavior of AISI 304L austenitic stainless steels during their tensile deformation with regards to changes in grain orientation and transformation of austenitic grains into strain induced martensite. Thus,* the main goal of the work is to study the effect of grain orientation changes on tensile deformation behavior of the material. The overall objective of present work consisted of several sub-problems/issues. The key issues taken up during the present research work are:

- To study the effect of annealing twins present in the grains, on the grain orientation change during tensile deformation.
- To study the deformation phenomenons activated in the grains during tensile deformation correlated with the grain orientations of the particular grains.
- To study the effect of grain size on the strain induced martensitic transformation in bi-modal type austenitic grains.
- To study the effect of grain misorientation on the strain induced martensitic transformation in bi-modal type austenitic grain structure.
- To study the effect of microstructure on the tensile properties of bi-modal type austenitic grained materials.

## 3.4 MATERIAL SELECTION

The chemical composition of the alloy under investigation has been shown in Table 3.1

**Table 3.1 Chemical Composition of AISI 304L Alloy**

| **Element** | **C** | **Mn** | **Cr** | **Ni** | **Si** | **S** | **P** | **N** |
|---|---|---|---|---|---|---|---|---|
| **Percent Weight** | 0.02 | 1.5 | 18.6 | 10.1 | 0.3 | 0.01 | 0.028 | 0.02 |

## 3.5 INPUT VARIABLES

The main input variable taken in this study is the strain level. A single specimen was strained to different strain levels to find the nucleation sites of martensite transformation. The different strain levels used in the study were selected on the basis of literature to see different deformation mechanisms activated at different increased strain levels. Also the grain orientations and misorientations were observed at different strain levels. However, the strain rate was kept constant during the study. The strain rate selected was very low, in the order of $10^{-5}$ $s^{-1}$. At higher strain rate values the martensite transformation suppresses due to increase in temperature beyond the martensite start temperature (Marshall, 1984). Thus, to observe the martensite phase nucleation sites and its growth, the strain rate was kept very low.

## 3.6 EXPERIMENTAL SETUP

Several machines and equipment have been used to achieve the objective or goal of the present study. Machines were used for mainly three different purposes: some machines were used for sample preparation, some for tensile experimentation and others for microstructural characterization. The detail of machinery and equipment used for sample preparation and tensile experimentation is described below.

### *3.6.1 Cold Rolling Mill*

The as-received AISI 304 steel samples were made available in thickness of 3.4 mm. Their thickness was reduced to a final size of 2.0 mm using a cold rolling mill of specifications (Maximum Width: 8”; Maximum Thickness: 6”). Unidirectional rolling with same thickness reduction in each pass was performed. Figure 3.1 shows the rolling mill used for the present work.

**Fig. 3. 1 Cold Rolling Mill**

### *3.6.2 Muffle Furnace*

In the present study, the muffle furnace is used for solution annealing of tensile samples. The box type furnace consists of two main bodies, outer and inner made of mild steel and stainless steel respectively. The glass wool insulation is used between outer and inner walls. The heaters mounted on the muffle are made up of 80/20 nichrome wire. Temperature of heaters mounted inside the furnace is controlled by capillary thermostat which enhances its accuracy and durability. The operating features of this furnace are on/off switch, digital display temperature controller, thermocouple sensor made of Cu/Al and indicators. Also, a safety fuse is provided for safety above the set temperatures. This furnace is run by a 230V (AC), 50Hz single phase supply. Muffle furnace used in the present study is shown in Figure 3.2.

### *3.6.3 In-situ Tensile Tester*

The present work uses a tensile tester ***(Make:*** **Gatan MTEST 2000** ***Microtest Tensile Tester***) suitable for in-situ scanning electron microscopy (SEM) tensile experiments; This tester is of small size and fitted properly in SEM chamber. The load capacity of this small tensile tester is 2KN. The software of this tensile tester can adjust the tensile experiment to five different motor speeds or strain rates. The extension obtained during tensile testing can be recorded at any stage during the tensile deformation in point. The points can be recorded in graph to very close points between the range.

**Fig. 3.2 Muffle Furnace**

Also, the break load detecting facility is provided. The data files and graphs are recorded in .csv and .bitmap files respectively. To hold the sample, four pins (two on each side) and a holding plate is proved in the arrangement. Figure 3.3 shows the in-situ tensile tester placed into scanning electron microscopy machine chamber.

## 3.7 SAMPLE PREPERATION

Sample preparation is a very important task in any study in which microstructure analysis has to be performed. To reveal microstructures in very high resolution machines like scanning electron microscopes with provision of electron back scattered diffraction or transmission electron microscope etc., highly polished samples are required so as to reveal the deep inside structures and then to correlate them with corresponding properties. In the present work, sample preparation has been done for in-situ tensile deformation study by the following the route/steps described in this section. The tensile specimens used in the present work are shown in Figure 3.4.

### *3.7.1 Cold Rolling*

As received plate of AISI 304L austenitic stainless steel of 3.4 mm thickness was cold rolled to a thickness of 2 mm and was then cut into dog bone shaped samples with a span of 10 mm, width 2 mm and thickness of 2 mm. The material, was cold rolled to same thickness reduction per pass. Unidirectional cold rolling was performed to achieve required thickness of sample.

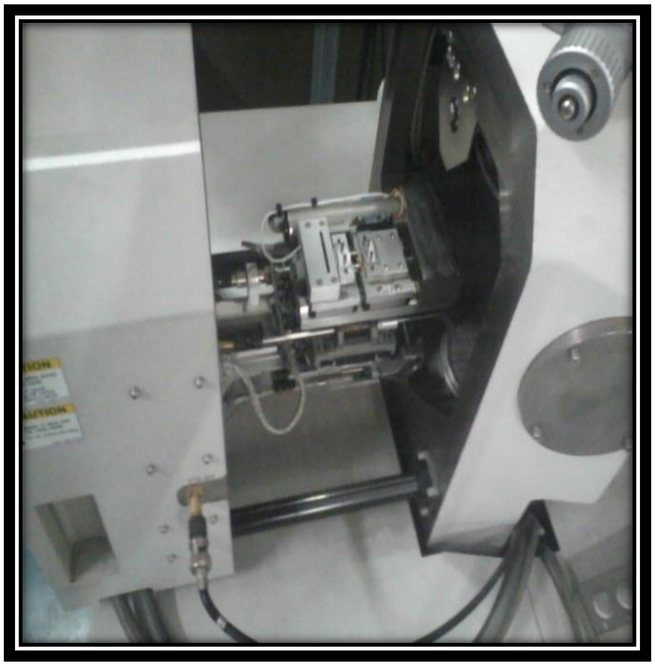

**Fig. 3.3 In-Situ Tensile Tester in SEM Chamber**

**Fig. 3.4 Tensile Samples of AISI 304L**

The shape of the samples was dog-bone shape required for tensile specimens. There were a total of four holes in each samples: two on each side for holding the sample in pins of microtest tensile tester.

### *3.7.2 Solution Annealing*

The cold rolled samples were brought to the muffle furnace. Here, solution treatment was given to samples to remove all the effects of cold rolling. The samples were loaded into muffle furnace at 800°C and after reaching at temperature 1060°C, the samples remained there for one hour. The solution annealing treatment was followed by air cooling.

### *3.7.3 Grinding*

After solution annealing (for eliminating cold rolling effects), the samples were brought to grinding and polishing lab. First of all, the samples were grinded with silicon carbide paper of small number (of 80 grit size) to remove scaling which evolved during solution annealing treatment. The grinding of the samples after cutting was also necessary to level or planarize the samples and to provide better finish. The scratches which occurred on samples due to grinding at papers disappeared by grinding the samples on silicon carbide papers of increased grit sizes. The grinding was started from coarser grit size paper and then to finer ones (the coarseness of paper is represented by its grit number means number of grits per square inch area). The finest paper used in this study was 2000 grit size paper. Every next paper removed the scratches of previous paper by grinding in perpendicular direction to previous paper repeatedly. After each grinding step, the sample was washed by soapy water to remove contaminants.

### *3.7.4 Polishing*

After grinding, the samples were polished by different polishing liquids and diamond paste for high level of finish to reveal microstructure in scanning electron microscope (SEM) by electron back scattered diffraction (EBSD) technique. In the present study, polishing was started from alumina solution on fine cloths tightly fixed on polishing wheels in the polishing machine. After polishing on alumina solution, the polishing was done with diamond paste (3μm particle size in diameter) to remove scratches and pits. After completing with the polishing with diamond paste, the (oily) samples were washed with soapy water to remove layer of oil particles from samples.

At last, polishing was done with very fine particle size colloidal solution to impart very high level of finish to samples. Before polishing with all solutions, the polishing wheels and cloths had been washed properly to prevent scratches and pit formations from any dust or other sticky particle. After polishing, the samples were dried with the drier to save samples from corrosion. When the samples were not under any kind of processing (in-between polishing process and also during any stage of study), they were placed into a desiccator for the same reason. Figure 3.5 shows the colloidal and alumina polishing machines (Make: BANIPOL METCO, Model No: PMVO18) of 0.37 Kw capacity was used in the present work.

**Fig. 3.5 Polishing Machine (Colloidal)**

### *3.7.5 Ultrasonic Cleaner*

After polishing, many contaminants like dust, oil particles, polishing agents, greases, holding tape particles, pigments, fluxes and fingerprints etc. adhere to surface and sometimes get embedded into the cavities, cracks and recesses of the sample. So, to reveal the actual microstructure clearly during characterization, these contaminants have to be removed. The ultrasonic cleaner is used to remove these contaminants by inducing high frequency sound waves in the cleaning agent. The sample is put into the cleaning agent (acetone, in present study) under vibrations of high frequency in the range of 20-400 KHz. The solvents or cleaning agents used to remove contaminants depends

**Fig. 3.6 Ultrasonic Cleaner**

on the type of contaminants. The ultrasonic cleaner (***Make: Elmasonic S30H***) with capacity of 80$^{o}$C maximum temperature and 30 min maximum time has been used in the present study.

## 3.8 IN-SITU TENSILE EXPERIMENT

The main phase of experimental work was in-situ scanning electron microscope tensile deformation. The main objective of in-situ analysis of tensile deformation behavior was to observe the time and place (i.e. the grains) where major and minor microstructural changes are happening during testing. For this purpose, a small in-situ tensile tester (GATAN Microtest Tensile Stage) has been used. The polished specimens were brought to scanning electron microscope lab for in-situ tensile deformation test. The experimentation was done in two main parts (a) first, a single specimen was strained to multiple level strain in a low strain range up to 6% and (b) in the second part, the material was strained to high strains in the range up to 30% strain.

### *3.8.1 Single Specimen at Varying Strain Levels*

An experiment was performed by taking a single specimen which was loaded at very low strain levels. At first, the specimen was loaded and strained up to 0.4% strain (i.e. just at yielding) and the test was interrupted. The load was relaxed and the samples were ultrasonically cleaned and scanned by electron back scattered diffraction (EBSD) detector and micrographs were recorded to observe microstructural changes. The specimen was then loaded up to 6% strain level and was again scanned following the earlier procedure.

In another experiment, a single specimen was loaded again to the small tensile tester and strained upto 7% strain. The specimen was unloaded, ultrasonically cleaned, and scanned in EBSD machine for microstructural analysis. After EBSD analysis, the sample was again loaded and deformed in tensile mode up to 10%, 14%, and 30% strain levels. In each case of strain level, the entire procedure, as discussed earlier was followed. The strain levels were decided according to the microstructural changes seen during tensile testing in scanning electron microscope (SEM).

### *3.8.2 Tensile Deformation of Bi-Modal (BM) Type Austenite Grained Material*

In this part of the work, tensile deformation of bi-modal type austenitic grained material with 0.5µm and 1.5µm size was done to study the microstructural changes. As received bi-modal type AISI 304L austenitic stainless steel prepared by thermal cycling technique was tensile deformed. A flat tensile dog bone shaped specimen of 25 mm gauge length was prepared. Tensile tests were conducted at room temperature under displacement control at a strain rate of 1.3 x $10^{-4}$ $sec^{-1}$ using a tensile testing machine (Instron 8862 system) of 100 kN capacity. The tensile specimens were marked at several locations along the gauge length and cross-sectional areas of the marked locations were measured before and after the tensile deformation to determine the true-strains. Electron backscattered diffraction (EBSD) was performed in a Field Emission Gun (FEG) scanning electron microscope with an EBSD system equipped with a high-speed camera for pattern acquisition. All samples observed here were prepared using initially the standard metallographic technique and then final polishing on colloidal silica. Subsequent to this, electro-polishing was done in order to give the highest diffraction pattern quality. A step size of 0.05 µm was used for EBSD data collection. Optical Imaging Microscopy (OIM) analysis software was used for data analysis.

## 3.9 TENSILE PROPERTY BASE MATERIAL

The solution annealed reference samples of material AISI 304L was tested on 100kN capacity tensile machine to obtain stress-strain graph. The tensile properties of this sample mainly yield strength (YS), ultimate tensile strength (UTS) and percentage elongation were calculated from the graph. Experiment was done with (***Make: INSTRON-8862***) tensile testing machine.

**Fig. 3.7 Tensile Testing Machine**

## 3.10 MICROSTRUCTURAL CHARACTERIZATION

The last and the most important part of the study is material characterization in which microstructure of the material is studied from several point of views for several different purposes. Microstructural investigation are very important because the properties of materials strongly depend upon materials microstructure. The present work correlates the impact of starting input variable (different levels of strain) on the microstructural changes mainly strain induced martensite transformation, variation of strain accumulation in different grains and change in crystallographic orientations. The main microstructure characterization machines used in this study are discussed as follows.

### *3.10.1 Optical Microscopy*

Optical microscope is used for the purpose of magnifying small samples by using visible light and system of lenses. The image from an optical microscope can be captured by normal light sensitive cameras to generate micrographs. Metallic materials are usually opaque and therefore investigations of plane cross-sections by incident light prevail in metallography. While amplitude objects become visible owing to differences in light absorption and thus appear in different grey shades or even colors, phase objects only differ in the refractive indices which cannot be recognized without additional provision. Starting from the cross-section preparation, to etching of the specimen, and setting up of microscope, all steps should be carefully optimized in order to get maximum information from a microscopic study. The optical microscope used in the study is shown in Figure 3.8 (***Make: LEICA DM 2500M***).

**Fig. 3.8 Optical Microscope**

### *3.10.2 Scanning Electron Microscope (SEM)*

In scanning electron microscope, an electron beam is used as a source for getting image from surface of the sample. The maximum magnification of SEM **(Make: HitachiS-3400N)** used for this study was 300000X and the resolution was 3 nm. The emitter used in a conventional scanning electron microscope was of tungsten electrode. The emitted electron beam strikes at the sample surface and ejects electrons from its surface. The ejected electrons give several kinds of signals captured by different detectors to obtain various types of information. The signals are in the form of secondary electrons (give morphology), back-scattered electrons (BSE), diffracted back scattered electrons (EBSD), characteristic X-rays used for elemental analysis, visible light and remaining as heat. The scanning electron microscope (SEM) contains a sample chamber, electron beam source, lenses, various types of detectors and display monitors as output devices. The sample used in scanning electron microscope should be conducting. In the present study, scanning electron microscope was used for in-situ tensile analysis of AISI 304 stainless steel to see the microstructural changes occurring during tensile testing. The tensile deformation in the sample loaded in a small tensile tester placed in the vacuum chamber of SEM was observed to interrupt test at required stages of deformation to get various information from EBSD technique. Figure 3.9 shows the SEM setup used in the present work.

**Fig. 3.9 Scanning Electron Microscope**

### *3.10.3 Electron Back Scattered Diffraction (EBSD)*

Electron Back Scatter Diffraction (EBSD) is also known as Backscatter Kikuchi Diffraction (BKD) or Electron Back Scatter Patterns (EBSP). It is generally an add on package to Scanning Electron Microscopy (SEM). EBSD is used to examine the crystallographic orientation of many materials, applied to crystal orientation mapping, defect studies, phase identification, grain boundary and morphology studies, regional heterogeneity investigations, material discrimination and micro-strain mapping etc. Additionally, the technique enables three-dimensional (3D) reconstruction of microstructure from consecutive surface sections that are created by mechanical serial sections. EBSD is conducted using a scanning electron microscope equipped with an EBSD detector containing at-least a phosphor screen, compact lens and low light CCD camera. Automated EBSD at present is limited to characterize only conductive materials in which grain size is larger than several tens of nanometre in diameter and several square millimetres in area. The surface should be reasonably flat and free from foreign layers. In this study (***Make: Digi View IV EBSD camera of EDAX Company***) was used for analysis.

# CHAPTER 4

# RESULTS AND DISCUSSION

## 4.1 GENERAL

This chapter explains and discusses of all the experimental results obtained from the study. The results and discussion on the microstructural changes occurred during tensile deformation occurring at different stages of deformation has been incorporated. The chapter includes the results on the changes in grain orientation/misorientation, variation in the martensite content in microstructure, strain accumulation in different grain boundaries and core of the grains during deformation from SEM-EBSD techniques. The slip mediated deformation activated during different deformation stages have been discussed in detail. The resulting strain hardening effect during tensile deformation is also discussed with explanation on the basis of microstructural changes. At starting, the composition of the material investigated and cold rolling and solution annealing treatment done on the material for certain purpose have been explained. After this, the results obtained from planned multilevel strain to a single specimen experiment which was analyzed through in-situ scanning electron microscope in collaboration with electron back scattered diffraction (EBSD) technique has been described in detail. In the second part of the experiment, the strain induced α'-martensite transformation during tensile deformation of bi-modal (BM) type grain distribution is reported. The chemical composition of the material under study is given below in Table 4.1.

**Table 4.1 Chemical composition of AISI 304L Steel**

| **Element** | **C** | **Mn** | **Cr** | **Ni** | **Si** | **S** | **P** | **N** |
|---|---|---|---|---|---|---|---|---|
| **Weight percent** | 0.02 | 1.5 | 18.6 | 10.1 | 0.3 | 0.01 | 0.028 | 0.02 |

The samples were cold rolled to achieve certain reduced thickness (already explained in chapter 3) suitable to perform tensile test on a small capacity in-situ tensile testing machine (Gatan MTEST 2000 Microtest Tensile Tester) attached in a scanning electron microscope (Hitachi S-3400 N) and solution treated to release the effects of cold rolling. Following three steps, tensile test was performed for tensile property evaluation.

## 4.2 TENSILE PROPERTY EVALUATION

The tensile properties of the base material AISI 304L were determined by constructing the stress-strain plot as shown in Figure 4.1 (data provided in Appendix 1).The yield strength, ultimate tensile strength and percentage elongation are obtained from the experiment. As the material did not show the yield point, the yield strength of the material was calculated with offsetting by 0.2% proof stress value as a standard practice. Tensile test was carried out on a 100 kN universal tensile machine (Instron Servo Hydraulic Machine INSTRON-8862) and tensile properties were recorded for the base material. These base properties were taken as reference values with the starting microstructure for the next planned multilevel strain to a single specimen in-situ tensile experiments to record the changes in microstructure.

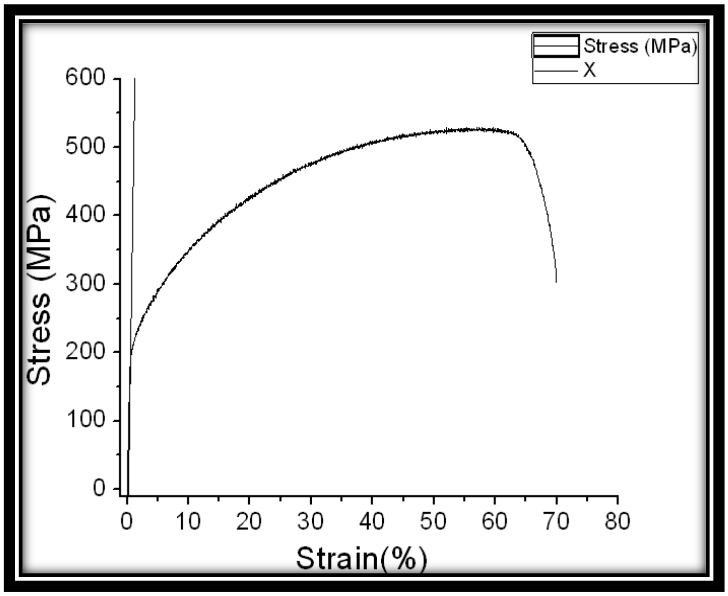

**Fig. 4.1 Stress-Strain Graph of Base Material**

The mechanical properties of the base AISI 304L steel are provided in Table 4.2.

**Table 4.2 Mechanical Properties of Base Material**

| Yield Strength | Ultimate Tensile Strength | Percentage Elongation |
|---|---|---|
| 191 MPa | 528 MPa | 70% |

## 4.3 EBSD ANALYSIS OF STARTING MATERIAL

The SEM-EBSD analysis was carried out for the virgin sample at zero strain level as reference to capture and later on compare/study the changes in microstructures during different deformation stages at different strain levels. The scanning electron microscope image (BSE-TOPO mode) shown in Figure 4.2 gave evidence that no signature of deformation, means slip lines and mechanical twinning was present in the microstructure which showed that all the effects of cold rolling had been cancelled by solution annealing treatment. At 0% strain, most of the grains consisting of annealing twins were observed in the microstructure captured by SEM and EBSD IQ map shown in Figure 4.2 and 4.3 respectively (white circles show some portions with annealing twins). Random orientation of grains in different crystallographic orientations in the starting material can be seen in EBSD colored orientation map as shown in Fig. 4.4.

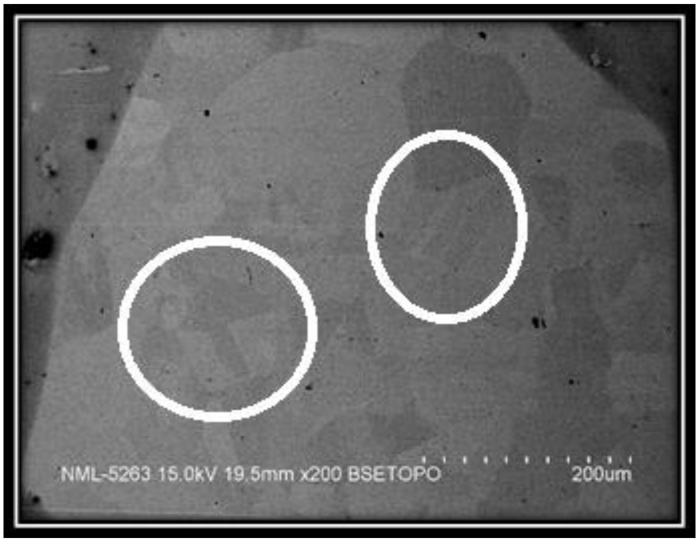

**Fig. 4.2 SEM Micrograph of Starting Material at 0% Strain**

The image quality (IQ) map from EBSD analysis showed the grains of the starting material inhibited no slip in Figure 4.3. Also the annealing twins present in the starting material can be clearly identified in several grains. The grain boundaries of the different grains also revealed clearly in EBSD IQ image.

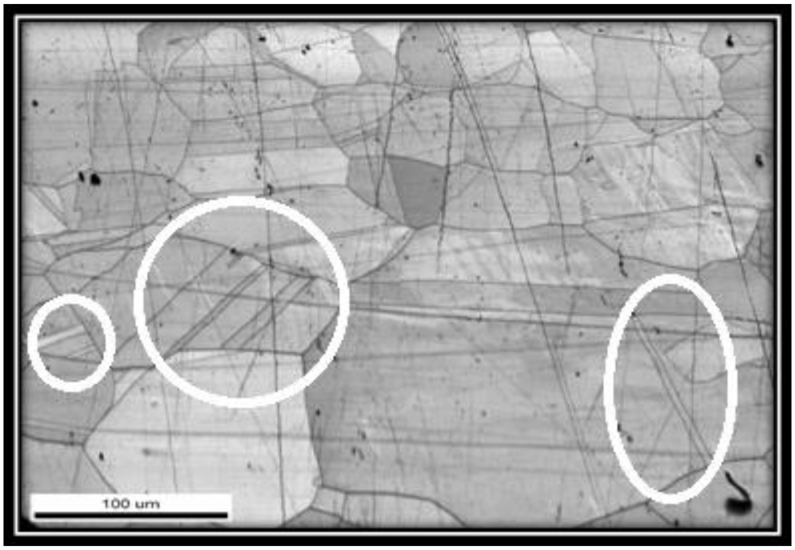

**Fig. 4.3 EBSD-IQ Map of Starting Material at 0% Strain**

The EBSD grain orientation map in Figure 4.4 for the starting material's grains show their grain orientations in different crystallographic directions with different colors of grains with respect to the colors in the stereographic triangle. The grains in Figure 4.4 have been appropriately numbered to identify and track them easily during the deformation process. The orientations of the grains shown in the EBSD map in Figure 4.4 are totally random. Most of the grains lie in the soft area of the triangle (refer Fig. 4.4a) and some lie near the [111] and [001] poles i.e. in hard area of the triangle. This starting phase map will help to track the change in grain orientations of different grains during tensile deformation at increased strain levels. The annealing twins in several grains can also be tracked with the changing orientations in next stages the tensile deformation. The tensile axis during the EBSD analysis has been aligned with [101] direction. For each grain that has been numbered in Figure4.4 a, the color of each grain has been matched with standard stereographic triangle (Figure 4.4 b), to obtain the orientation of the grain. Grain 1 lies near the [101] orientation at which the tensile axis was aligned. The grain numbers 2, 3 and 4 were oriented in the soft orientation area in the stereographic triangle i.e. near [123] orientation. Grain 5 was lying near to [112] orientation and the twinned region in this grain was near [113] crystallographic orientation. Grain 6 was at the [123] soft orientation and the twin within this grain was at the nearly [101] orientation. Grain number 7 was lying near the [133] hard orientation and twin within this grain was at [123] orientation. Grain numbers 8 and 11 were situated at [001] hard orientation and twin in grain number 8 was at [101] orientation. Grain number 9 lies near the orientation [133] and the twinned region within this grain lies near [012] direction.

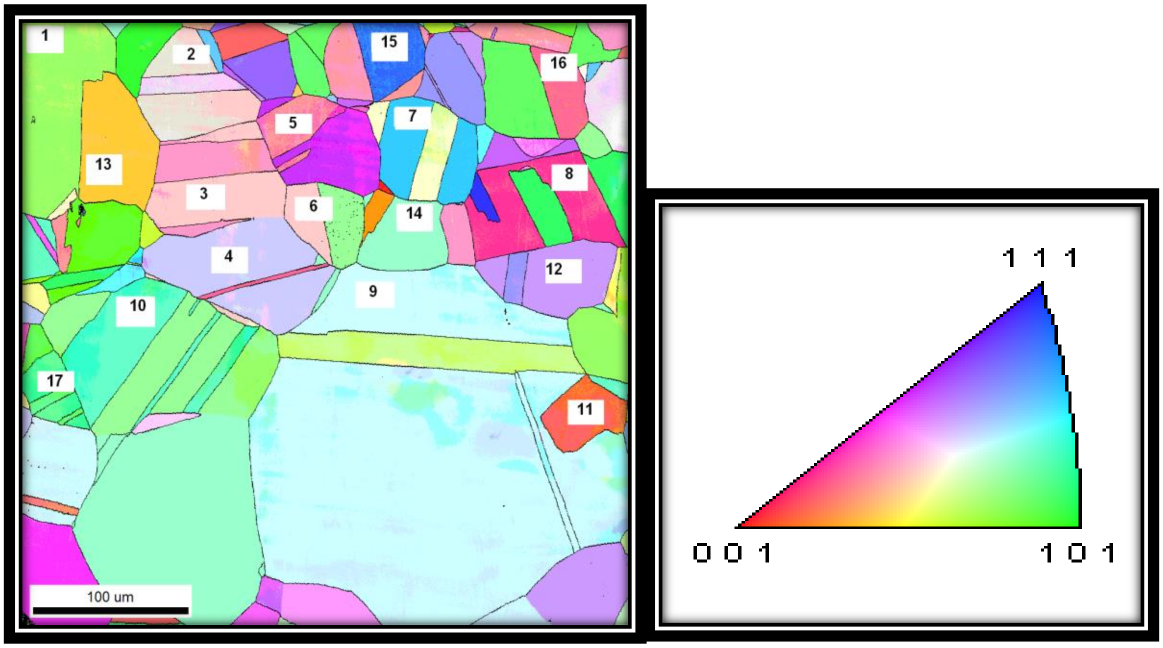

**(a)** **(b)**

**Fig. 4.4 (a) EBSD Grain Orientation Map at 0% Strain Level (b) Standard Stereographic Triangle**

Grain number 12 and the twin in this grain was at the stabile orientation [112]. Grain numbers 10 and 17 in the EBSD orientation map were at the [155] orientation and the multiple twinned regions in this grain were in the near [101] orientation as of the grain. Grain numbers 13 and 14 were oriented near the center of the triangle, means at [123] orientation in the soft region having high Schmid Factor. Grain number 15 and the twinned region in this grain were both oriented in the [001] and [111] hard orientation of the stereographic triangle. Grain number 16 was oriented at [101] orientation and the twinned region in this grain was near [001] orientation.

EBSD analysis was also used to prepare (for 0% strain level) the GB Misorientation Map (Figure 4.5 a) and, the graph between fraction of grain boundaries (Number Fraction) and misorientation angle (Figure 4.5 b). The data in Figure 4.5 (a, b) shall be used to compare the changes in grain boundary character of the material when it is deformed to different strain levels.

Table 4.3 presents the coding criteria to be followed for grain boundaries to prepare the GB Misorientation Map. This criteria classifies the grain boundaries into four categories (gives four color codes) on the basis of misorientation angle range. Figure 4.5 (a) provides the following information.

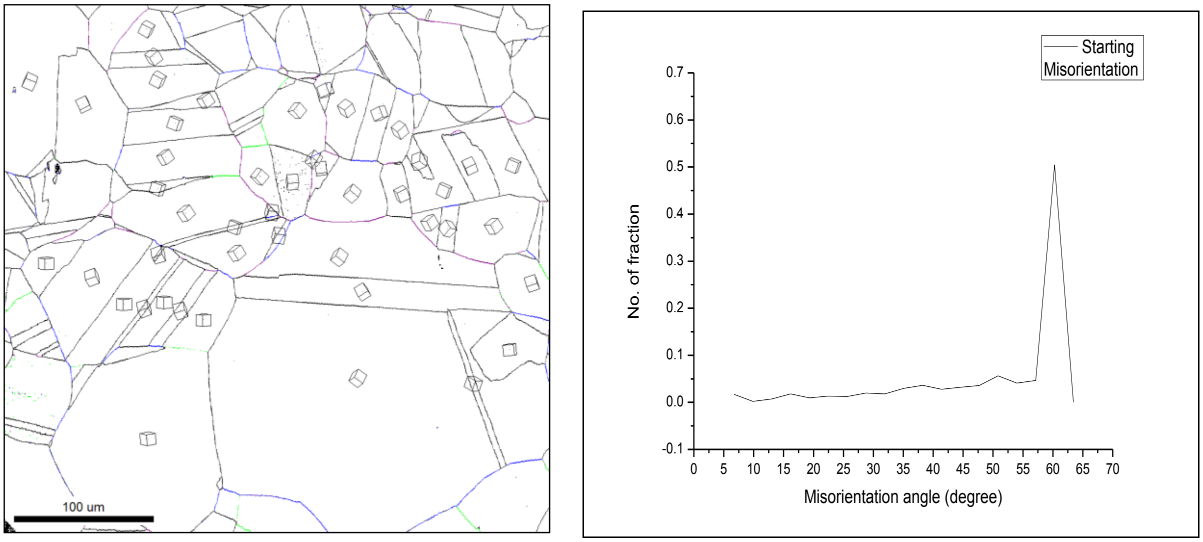

**(a)** **(b)**

**Fig. 4.5 (a) GB Misorientation Map b) Misorientation Angle V/S No. Fraction Curve for Starting material**

- The cube (⬡) shows the grain orientation for each crystal grain.
- The cube (⬡) also shows the orientation of twins present in some grains.it may also be noted that in any crystal containing a twin, the orientation of the two (grain and twin) is different.
- In case a grain has an annealing twin at the grain boundary area (eg. Grain Number 3 and 6), it leads to a different grain boundary character (in terms of misorientation)

Figure 4.5 (b) shows the graph between Misorientation Angle and Number Fraction of grain boundaries. Figure 4.5 (b) reveals that most of the grain boundaries were high angle grain boundaries with misorientation angle peak at 60° (approx.). This observation can be noted from Figure 4.5 (a) also, where most of the grain boundaries are in black color (for which misorientation angle is more than 40°) followed by blue color.

**Table 4.3 Misorientation of Grain Boundaries**

| Color of GB | Min. | Max. |
|---|---|---|
| 🟩 | **5°** | **15°** |
| 🟪 | **15°** | **30°** |
| 🟦 | **30°** | **40°** |
| ⬛ | **40°** | **180°** |

A very small fraction of grain boundaries were low angle grain boundaries. EBSD analysis was also used for Schmid Fcator calculations. Figure 4.6 shows the Schmid Factor values (refer Appendix 3) and the corresponding Number Fraction of grain boundaries. Figure 4.6 shows that high fraction of the grains lie under high Schmid Factor values in the range of 0.4 to 0.5. This high Schmid Factor for high fraction of grains showed that deformation will start in most of the grains which lie in high Schmid Factor region. Three peaks of the graph are at 0.42, 0.45 and 0.49 Schmid factor values.

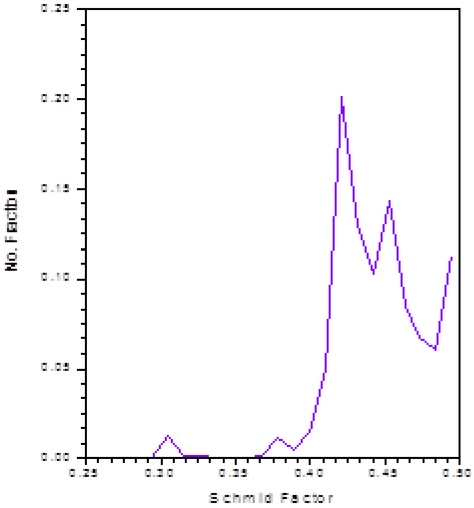

**Figure 4.6 Schmid Factor and Number Fraction of Grains in Starting Material**

At last grain orientation in stereographic triangle has been also shown for the starting material (from EBSD analysis) in Figure 4.7. The grain orientation map at 0% strain has revealed that most of the grains lie at the soft orientation area and [101] orientation in stereographic triangle. Very few grains lie near the [111] pole and some grains also lie in the [001] orientation (i.e. hard regions).

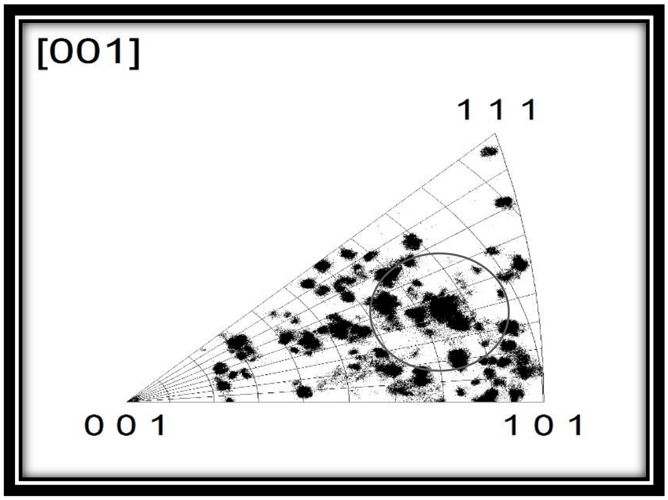

**Fig. 4.7 EBSD Grain Orientation Map for Starting Material (0% Strain)**

## 4.4 IN-SITU SEM DEFORMATION OF MATERIAL AT 0.4% STRAIN

After recording the grain orientations, Schmid factors and misorientation of grain boundaries at 0% strain level (from SEM and EBSD analysis), the sample was further strained just up to its yield point, at 0.4% strain (Δ l= 0.04 mm) level (under in-situ tensile stage in the SEM). The change in the orientation of grains was captured by EBSD and represented by the grain orientation map as shown in Figure 4.10. The load v/s elongation graph shown in Figure 4.8(b) (refer appendix 4) showed that the test was interrupted at 0.4% strain and the in-situ SEM microstructure (BSE-TOPO mode) as shown in Figure 4.8 (a) revealed changes at this level of strain without etching.

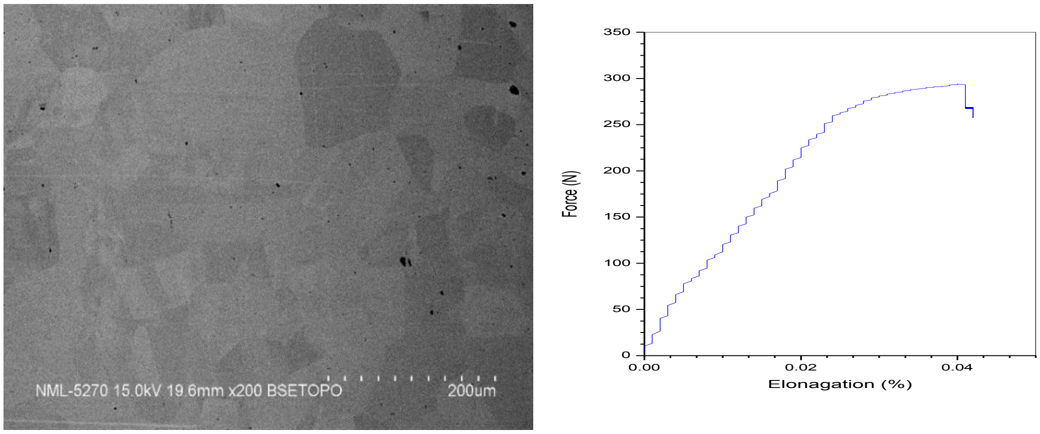

**(a)** **(b)**

**Fig. 4.8 a) SEM Micrograph at 0.4% Strain b) Load v/s Elongation Graph at 0.4% Strain**

In-situ tensile deformation up to 0.4% strain (just at yield point) showed a few slip lines in some grains. The SEM micrograph in Figure 4.8(a) revealed the small elongation of grains. The EBSD-IQ image given in Figure 4.9 showed appearance of slip lines in a few grains which was signature of the inset of plastic deformation in the material. also revealed the slip in few grains and the elonagtion of the grains at 0.4% strain.

The change in grain orientations of different grains was recorded at the strain just on the yield point (0.4% strain) and is represented in Figure 4.10. This grain orientation map (Figure 4.10) can be used to observe and identify the grains who have changed their orientation at the start of deformation in the material. Grain 1 oriented near [101] orientation in the starting material (strain level: 0%) got oriented near [123] orientation after 0.4% strain due to the high Schmid factor in this region. The grain numbers 2, 3 and 4 also showed a large orientation change because these grains were also lying in the easy glide regions before deformation having (i.e were lying in regions with high Schmid factor values). Grain number 5 which was oriented near [113] orientation on [001]-[111] boundary before deformation, got oriented near the stable [112] orientation after 0.4% strain level. However, the twinned region in this grain was oriented near [013] orientation at [001]-[101] boundary of the stereographic triangle. Grain number 6 oriented near center of triangle in the easy glide region was oriented at the stable [112] orientation at this level of strain but the twinned region in this grain changed its orientation to near [155] orientation. Grain number 7 was reoriented to near [111] orientation but the twinned region in this grain changed its orientation from nearly [123] towards [001] orientation.

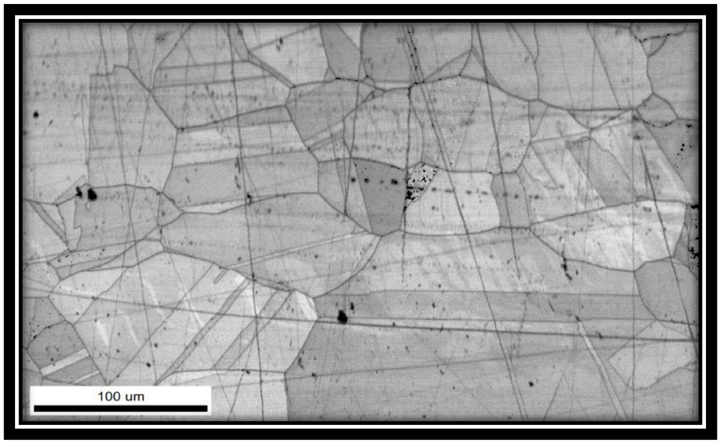

**Fig. 4.9 EBSD-IQ Map at 0.4% Strain**

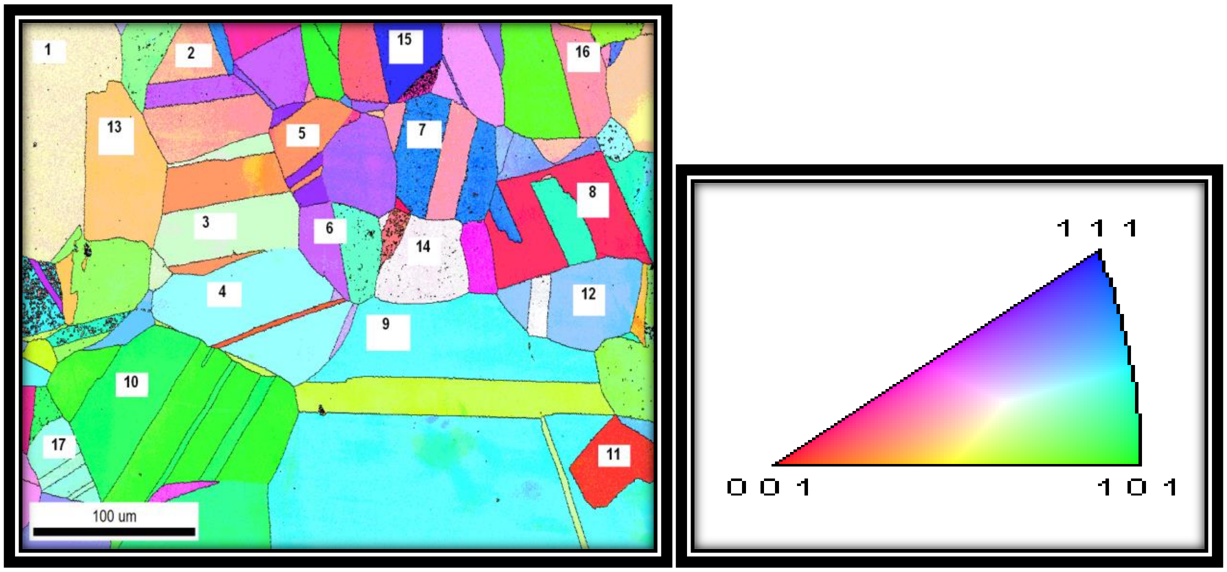

**Fig. 4.10 (a) EBSD Grain Orientation Map (0.4% Strain) (b) Standard Stereographic Triangle**

Grain number 8, 11 and 15 did not show any change in their orientation up to this strain because their orientation was far away from the tensile axis and they had orientations in the hard regions (i.e. having low Schmid factor values, near [001] and [111] poles of the stereographic triangle). Grain number 12 changed its orientation from nearly [112] towards [111] pole and the twin in this grain got oriented from near [111] orientation to [123] orientation in the center of the triangle. Grain number 10 having multiple twinned regions within it exhibited only a small orientation change. This was because the strain was distributed in the neighboring grain numbers 2, 3 and 4 having very high Schmid factor values. Due to the same reason, grain number 13 has also exhibited only a minor orientation change. Grain 9, which was oriented in [133] orientation at [101]-[111] boundary (means in the hard orientation area of the stereographic triangle) did not show any noticeable change in orientation change and twinned the region in this grain also did not show orientation change. Another reason was that this grain (Grain Number 9) occupied a large area due to which it did not accumulate the minimum required strain for orientation change. Figure 4.11 (b) (refer appendix 5)shows the graph between Misorientation Angle and number fraction of grain boundaries when the material is subjected to 0.4% strain level. It can be observed from Figure 4.11 (b) that as compared to the starting material (Figure 4.5 b) some fraction of low angle boundaries have changed into high angle grain boundaries (misorientation angle ranging between 35-40°). Also, there was a slight increase in the number fraction of higher angle grain boundaries with (misorientation angle in the range 55-65°). figure 4.11 (a) reveals that some of the low angle grain boundaries (which were present in the starting meterial, and shown by green color in Figure 4.5 a) have shifted to high angle regime.

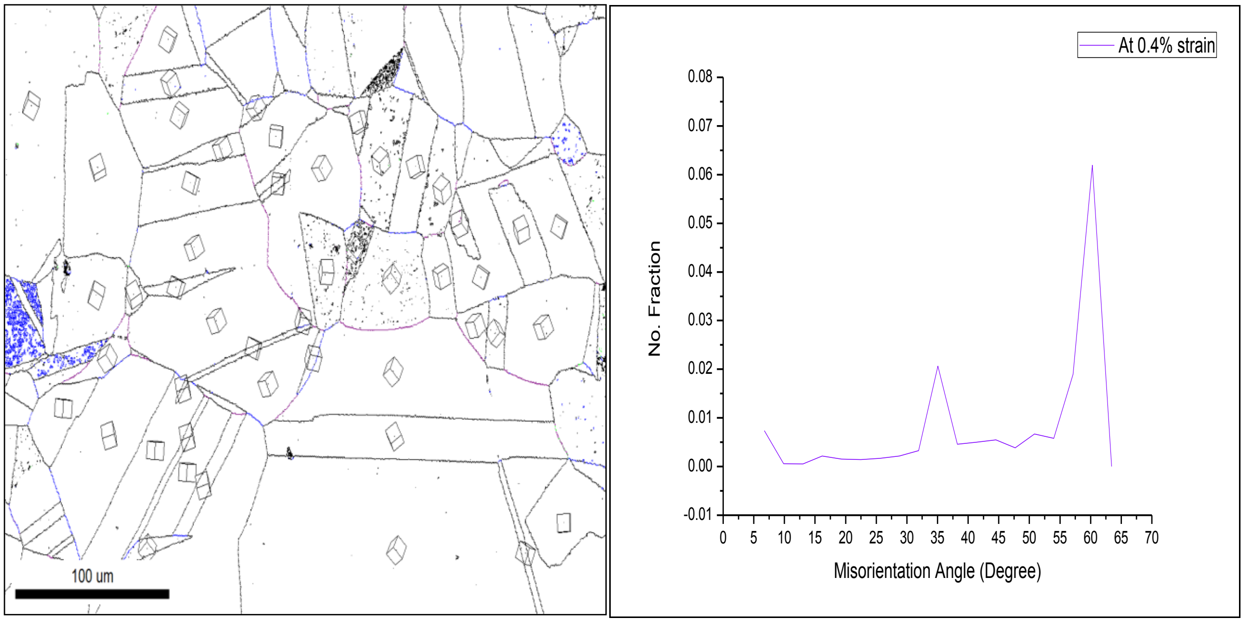

**(a)** **(b)**

**Fig. 4.11 (a) EBSD GB Map showing Misorientation (b) Misorientation Angle v/s Number fraction of grain boundaries**

Figure 4.11 (a) reveals that most of the grain boundaries are high angle (with misorientation angle more than 40°), followed by grain boundaries with misorientation angle ranging between 30-40°. it may be noted that there are no small angle grain boundaries (green color).

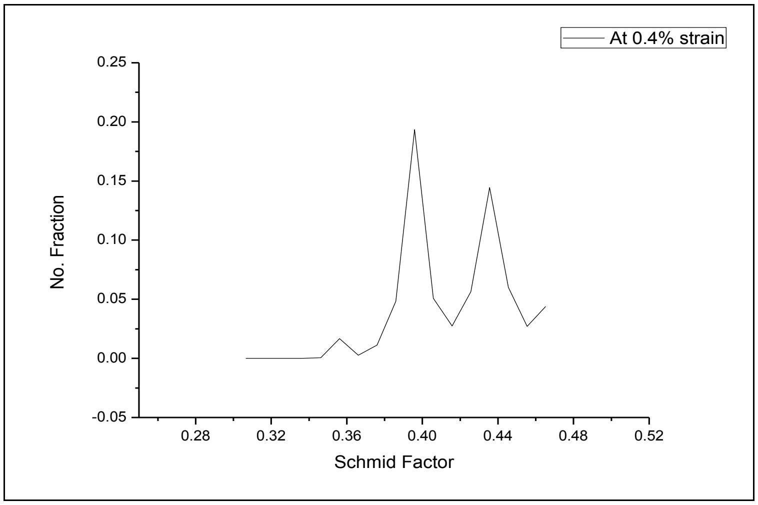

**Fig. 4.12 Schmid Factor v/s Number Fraction of grains at 0.4% Strain**

The Schmid Factor calculations (refer appendix 6) for the number fraction of grains from EBSD analysis at 0.4% strain level show that a high number fraction if grains lie under high Schmid Factor region with two peaks at 0.40 and 0.44 values. Here, it may be noted that as compared to the starting material (Figure 4.6) having three peaks, the strained material (0.4 % strain level) has only two peaks. The highest peak of the starting material i.e. grain with Schmid Factor value 0.49 have got deformed and now oriented in low Schmid Factor regions. Figure 4.13 shows the grain orientation in stereographic triangle for the material at 0.4% strain level. Figure 4.13 shows the strectching of grains which earlier lied in the soft orientation area in the starting material (Figure 4.7). These grains have now deformed and have rotated in the stable orientation [112].

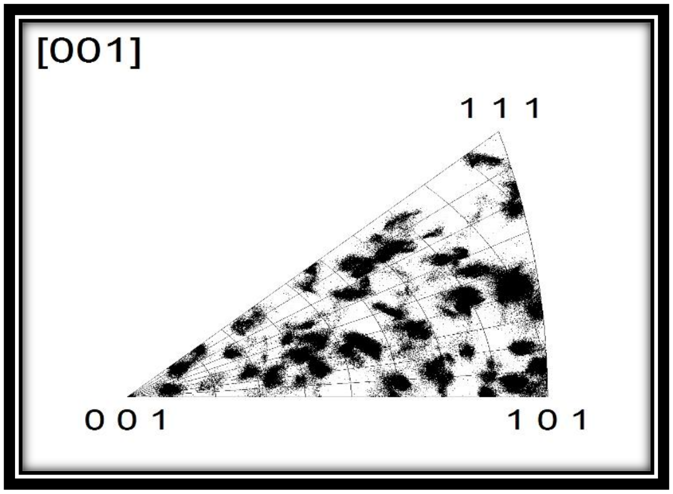

**Fig. 4.13 EBSD Grain Orientation Map at 0.4% Strain Level**

The strectch in grain orientation map at 0.4% strain level (Figure 4.13) gave a clear evidence that the grains having orientation in easy glide region (at the center of the stereographic triangle) have started to rotate towards the [001] and [111] boundary at [112] orientation by plastic deformation in the material. Thus, the grain density increased at nearly [112] orientation compared to the starting material at this strain level (0.04%).

### 4.5 IN-SITU SEM DEFORMATION: AT 6% STRAIN

After the first stage of deformation (strain up to yield, 0.4% strain), the sample was strained to 6% strain level and the SEM micrograph for the same is shown in Figure 4.14 (refer appendix 7). The micrograph  revealed more slip lines in the microstructure. The slip lines shown in the SEM micrograph  (Figure 4.14) might have appeared due to the large value of Schmid Facor in a large fraction of grains (Figure 4.12) which undervent plastic deformation.

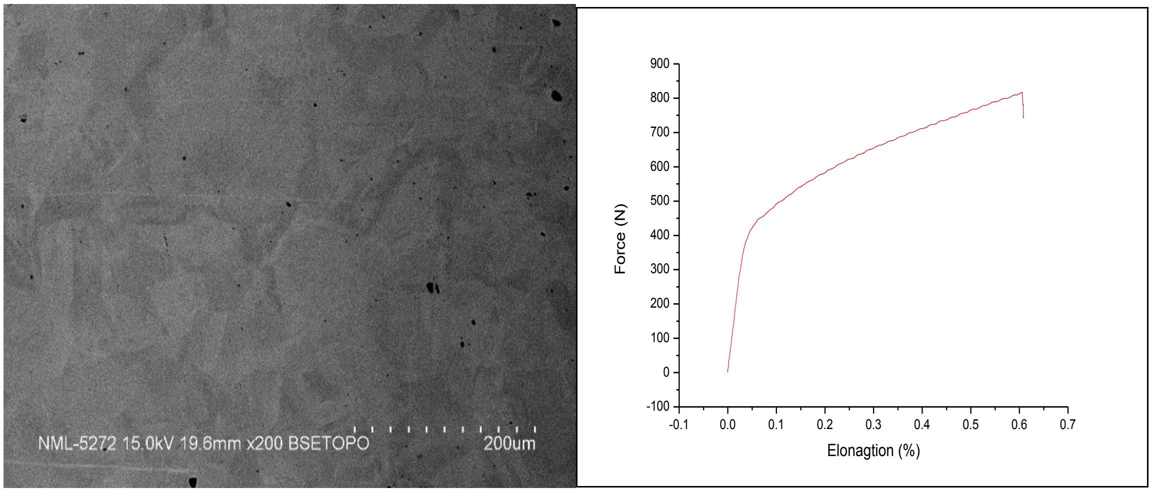

**(a)** **(b)**

**Fig. 4.14 a) SEM Micrograph b) Load v/s Elongation at 6% Strain Level**

The IQ Map (Figure 4.15) from the EBSD analysis revealed that slip lines were more prominant in grians 1, 4, 9 and 15 which showed that these grains have accommodated the plastic deformations.

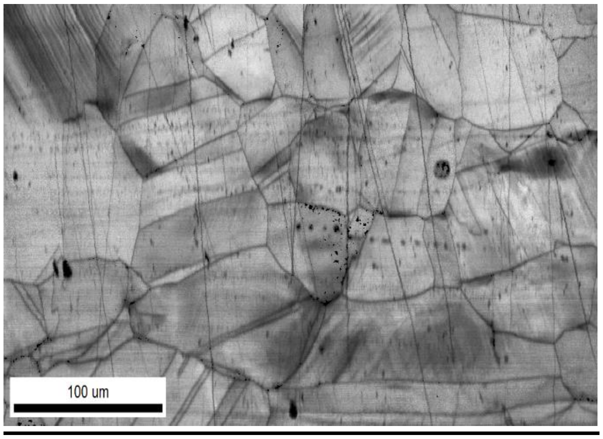

Fig. 4.15 EBSD-IQ Map at 6% Strain Level

Figure 4.14 (b) depicts the load-extension curve which shows that the test has been interrupted at 6% strain level. EBSD Grain Orientation Map in Figure 4.16 shows that most of the grains still lie (on changing strain level from 0.4% to 6%) in the soft area with high Schmid Factor [by comparing Figure 4.16(a) and 4.16 (b)].

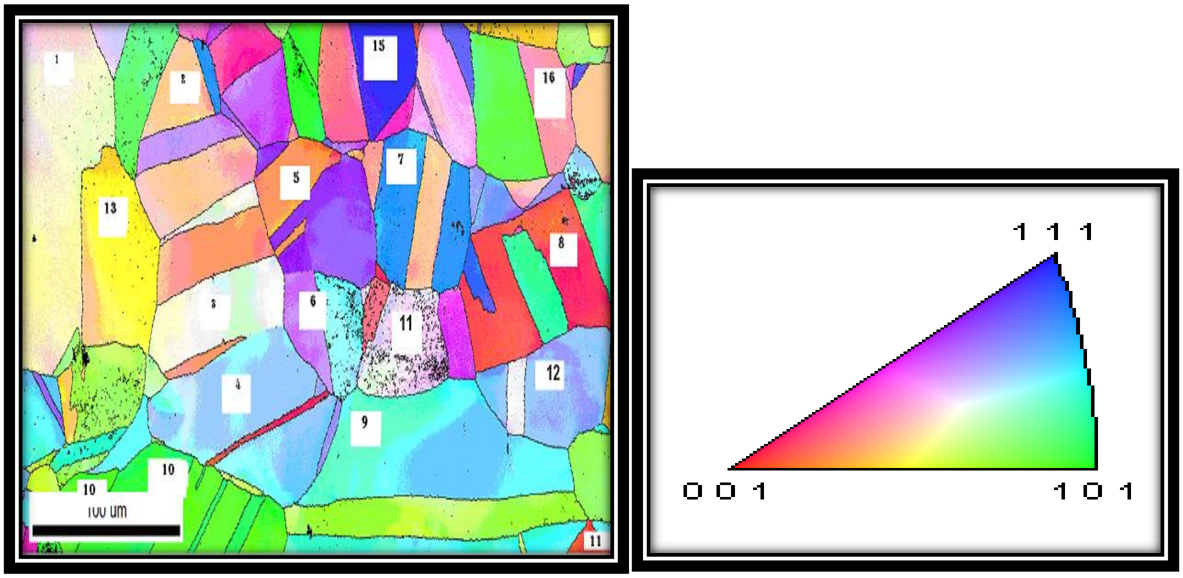

**(a)** **(b)**

Fig. 4.16 EBSD Grain Orientation Map a) at 0.4% Strain Level b) Standard Stereographic Triangle

In the initial stage of deformation (from 0% to 0.4% strain level), grains 2, 3and 4 showed significant change in orientation [refer Figure 4.4 (a) and Figure 4.10 (a)] and thus accommodated plastic deformation due to their high Schmid Factor. However, during the initial deformation grain 13 (surrounded by grain 2, 3 and 4) did not show significant change in orientation and did not appreciably accommodate plastic deformation because of its relatively low Schmid Factor than the surrounding grains. But in the next stage of deformation (0.4%-6%), grain showed an appreciable change in orientation (Figure 4.16a) and accommodated plastic deformation. This happened because its neighboring grains (2, 3 and 4) had already reached relatively stable orientations at strain levels of 0.4%. At 0.4% strain level, grain one was oriented at [123] soft region and had a high Schmid Factor. On increasing the strain level to 6%, it reoriented at [112] (refer Figure 4.16 b). EBSD-IQ Map (Figure 4.15) shows slip lines in this grain which indicate that this grain has accommodated plastic deformation. Further, it can be noted that because of slip, different orientations (with different colors) within the same grain can be observed (e.g. Grains 1, 4, 9,12 and 13 which represents slip mediated plastic deformation have different orientations and hence different color within same grain). The same observation was made for grains 4, 9, 12 and 13 also.

Grain 2, 3, 5, 6, 7, 8, 10, 12 and 15 had already reached nearly stable orientation at strain level of 0.4%, therefore on increasing the strain level to 6%, these grain did not show any significant change with regards to grain orientation (Figure 4.10 a and 4.16 a). Grain 14 which was oriented near [123] at 0.4% strain got reoriented to nearly [112] orientation.

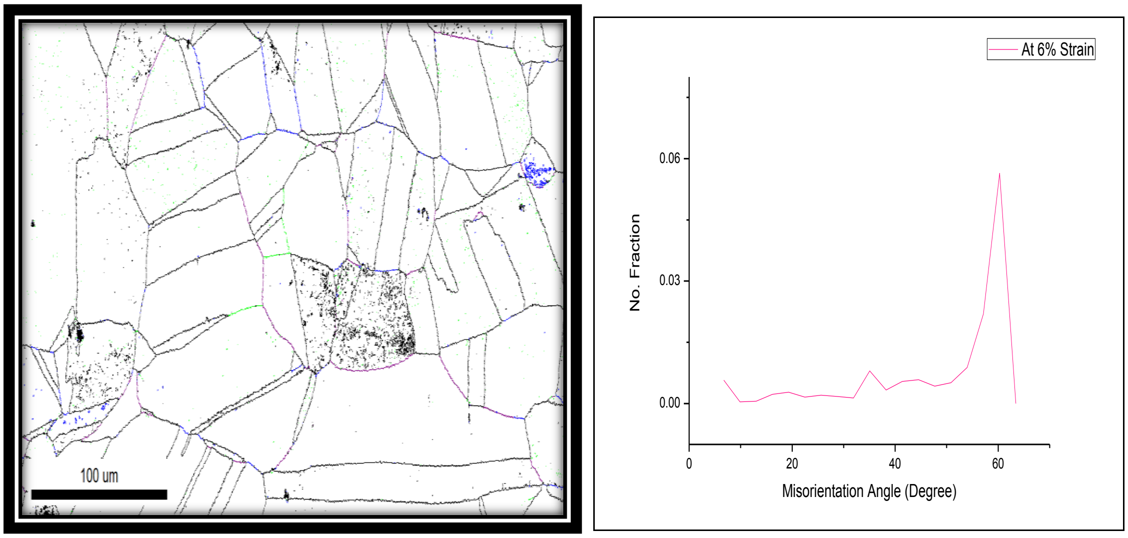

**(a)** **(b)**

**Fig. 4.17 a) Grain Boundary Misorientation Map b) Misorientation Angle v/s Number Fraction Graph**

The Schmid factor calculation at this level of strain shown in Figure 4.18 revealed that the Schmid factor was again high for a large number fraction of grains. Schmid Factor is near 0.5 for very small fraction of grains. Another peak was observed at 0.42.

**Fig. 4.18 Schmid factor at 6% strain**

The above results showed that the grains having orientations near the center of the stereographic triangle exhibited orientation changes at the starting of deformation towards the stable [112] orientation due to their high Schmid factor values. The grains near the [001] and [111] hard orientations and away from the tensile stress direction [101] were having low Schmid factor values and exhibited negligible orientation changes up to the strain level at which all grains lying in the soft region (having high Schmid factor values) rotated to their stable [112] orientation. Also the effect of neighboring grains was observed on the rotation of the grains. For grains with twinned regions within them, it was observed that the orientation change with strain was different for the grains and its twinned region. The misorientation mapping did not show large changes in the grain boundary misorientation behavior with increased strain level. However, small fraction of the grain boundaries shifted to high angle grain boundaries.

## 4.6 EBSD ANALYSIS AT HIGH STRAIN LEVELS

After tracking the tensile deformation behavior of material at low strain levels the material was deformed at high strains up to 30% with same in-situ SEM and EBSD technique. Slip mediated plastic deformation and its growth through increased strain levels was studied.

### 4.6.1 In-situ SEM deformation: at 7% strain level

After the tensile deformation of AISI 304L austenitic stainless steel at low strain levels up to 6% strain, the tensile deformation behavior of the steel at high strain levels was recorded with the help of in-situ SEM and EBSD analysis. The microstructural changes in respect of change in the crystallographic orientations and slip mediated plastic deformation on increased strain levels was analyzed. The results were again tracked by grain to grain changes. At 7% strain level, the EBSD (colored) grain orientation map is shown in Figure 4.19. Most of the grains were oriented near [101] and [112] crystallographic orientations w.r.t the stereographic triangle. Slip lines were observed in some grains as revealed by IQ map shown in Figure 4.19(c).

The EBSD grain map (Figure 4.19a) and the IQ map (Figure 4.19c) at this level of strain were recorded to observe the orientation change and growth of slip mediated plastic deformation in the material. Total of four grains were tracked in the same way as done in low strain regime.

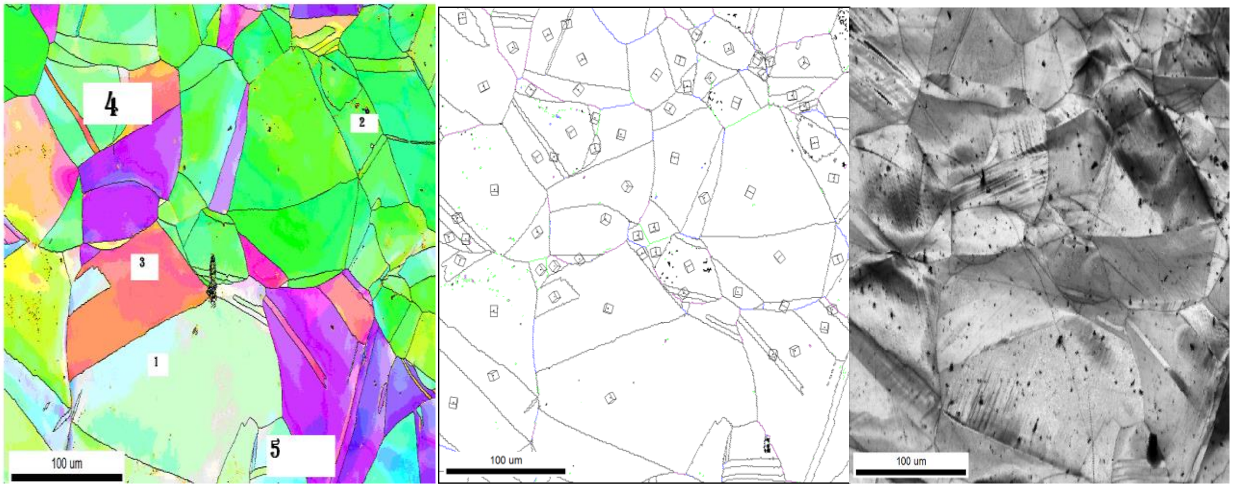

**(a)** **(b)** **(c)**

**Fig. 4.19 a) EBSD Orientation Map b) Misorientation Map c) IQ Map at 7% Strain Level**

### 4.6.2 In-situ SEM Deformation: at 10% Strain Level

The next stage of plastic deformation at 10% strain level showed changes in the grain orientation in the grains exhibiting slip lines. The grains shown in the EBSD map in Figure 4.20(a) at 10% strain level revealed the orientation change in the grains lying in [101] orientation with slip mediated plastic deformation and the grains were rotating at the [001]-[111] boundary at [112] stable orientation.

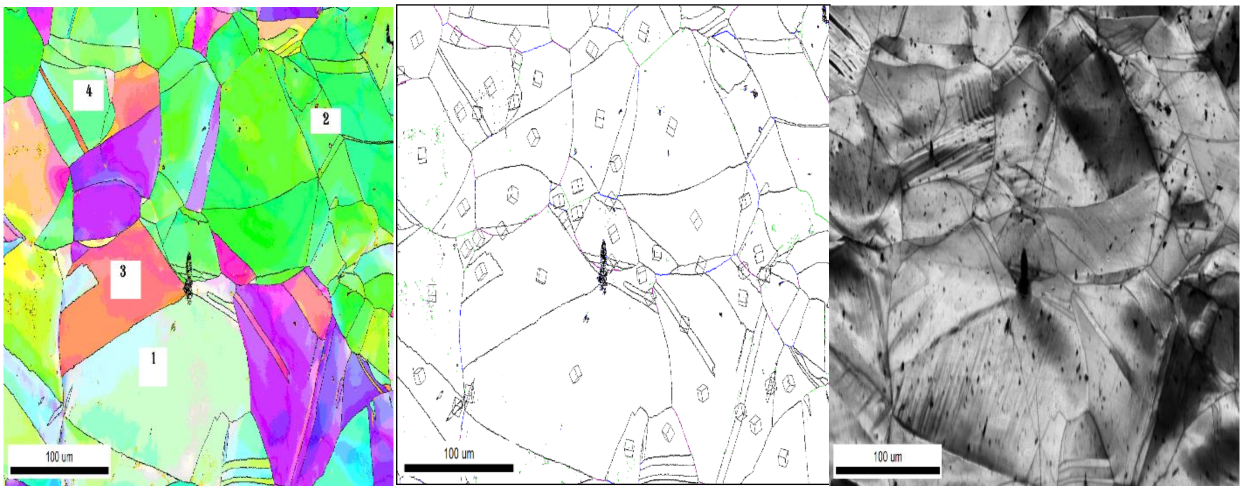

**(a)** **(b)** **(c)**

**Fig. 4.20 a) EBSD Orientation Map b) Misorientation Map c) IQ Map at 10% Strain Level**

At 10% of strain level the grain number 1, undergone slip mediated plastic deformation showed the orientation change and oriented at [123] orientation shown in the EBSD map in Figure 4.20(c). Grain 2 was not undergone yet any orientation change up to this level of strain. The grain number 3 shown to be oriented in two orientations some area of this grain is oriented at [013] orientation and other at [113] orientation. The twinned grains 4 & 5 showed some relation with the orientation of its twin region. The grain and its twin were rotated at the different orientations in the stereographic triangle.

### 4.6.3 In-situ SEM Deformation: at 30% Strain Level

The EBSD colored grain orientation map in collaboration with the IQ map at this strain revealed the grain orientation change at the same areas where the slip lines were recorded in IQ map shown in Figure 4.21(a & c). Still most of the grains at 30% strain lying in the [101] orientation it means that the deformation was still in the stage-1. the slip lines observed in the grain number 1 & 2 at 30% strain showed the orientation change on the slip lines and both the areas of slip lines in these grains rotated to the orientation of [112] stable orientation at [001]-[111] boundary.

grain number 2 which was at two orientations in the 7% and 10% strain levels was oriented completely at [113] orientation at [001]-[111] boundary.

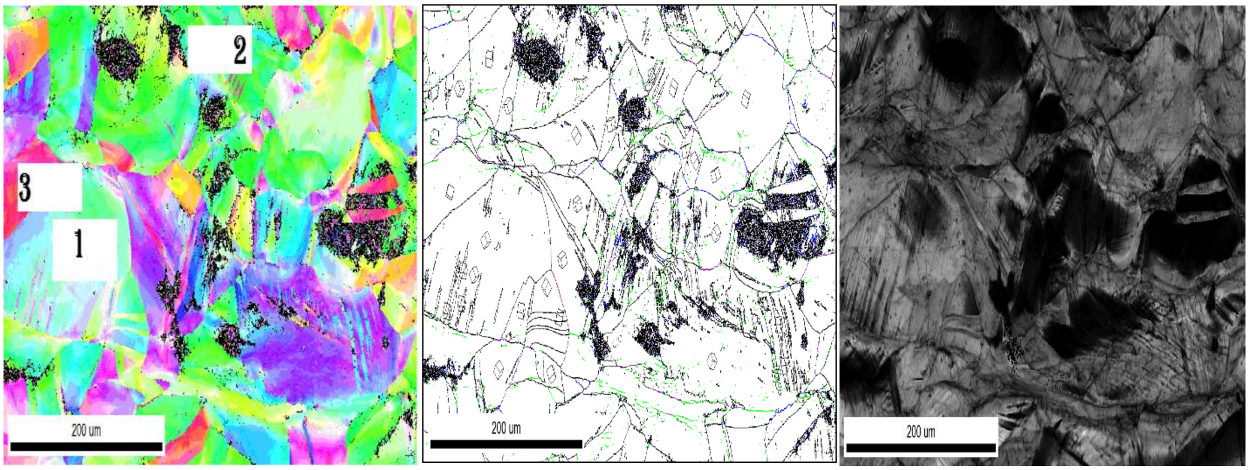

(a) (b) (c)

**Fig. 4.21 a) EBSD Orientation Map b) Misorientation Map c) IQ Map at 30% Strain Level**

Scanning electron microscope (SEM) images during tensile deformation at different strains showed the slip mediated plastic deformation in the material. With increasing strain level the slip lines increasing in more number of grains shown in Figure 4.22 (a, b, c & d). The SEM micrographs showed that at medium strain of 14% multi-variant slip comes into picture which is the sign of start of strain hardening in the material. At 30% strain slip lines were observed in each grain of the material.

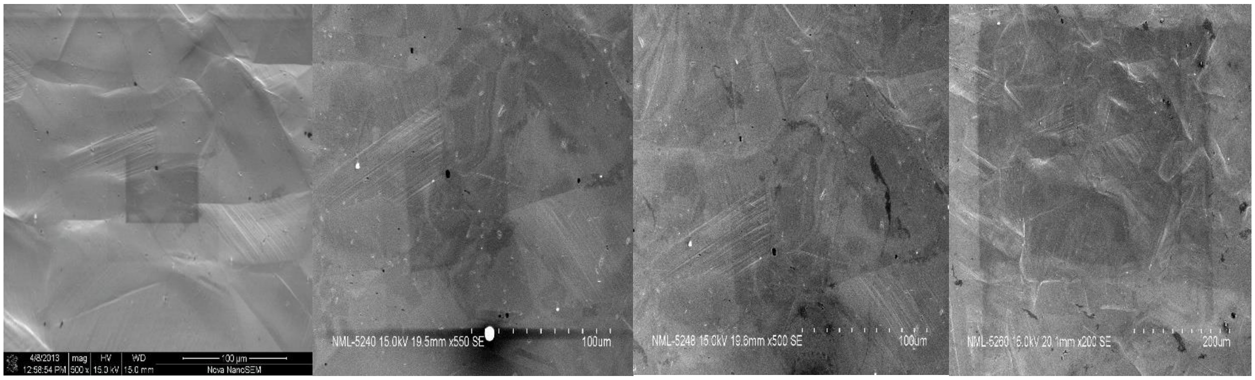

**Fig. 4.22 SEM micrographs showing slip lines strain levels a) 7% b) 10% c) 14% d) 30%**

SEM micrographs show the slip mediated plastic deformation in the material but the load v/s extension graphs from 7% to 30% deformation showed the absence of the strain hardening in the material. This was due to that the dislocation interactions were very low because the unit slip systems were activated at these strain levels in the deformation stage-1 for FCC materials. The multi-variant slip was activated also in some of the grains but the grain size was large so no strain hardening was shown in the load v/s extension graph. The load v/s extension curves are shown in the Figure 4.23.

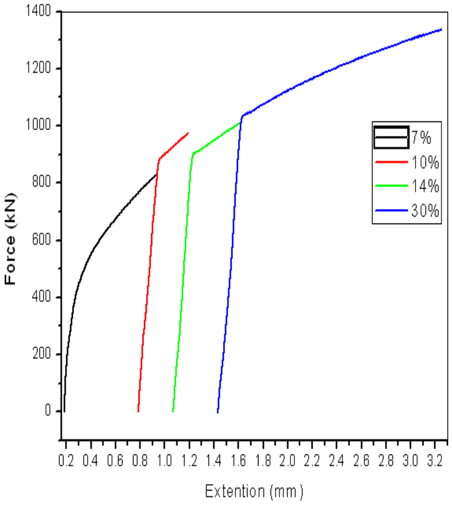

**Fig. 4.23 Load v/s Extension Curves at 7%, 10%, 14% and 30%**

## 4.7 PHASE TRANSFORMATION DURING DEFORMATION

Martensite transformation in 304L austenitic stainless steel depends upon pre-strain, strain rate, stress state and temperature (Shen et al., 2012). In this work, 304L austenitic stainless steel was deformed in tensile mode up to 30% strain by multi-loading to a single specimen technique. Despite the low Stacking Fault Energy (SFE), total strain of 30%, and low strain rate ($10^{-5}$ $s^{-1}$) [i.e. all conditions favoring martensitic transformation], the martensite phase was not observed in the microstructure. The temperature ($M_d$) at which 50% martensite gets formed at 30% true strain has been calculated from Equation 4.1(Marshall, 1984). $M_d$ comes out to be above $28^0$C.

$$M_d\ (\alpha')\ (30/50) = 413 - 9.5\%\ \mathrm{Ni} - 13.7\%\ \mathrm{Cr} - 8.1\%\ \mathrm{Mn} - 9.2\%\ \mathrm{Si} - 18.5\%\ \mathrm{Mo} - 462\%\ (\mathrm{C+N})$$

**…………………. Eq 4.1**

All the conditions discussed here are favorable for martensite transformation, but still there was no evidence of martensite presence in the microstructure Figure 4.25. The reason that comes forward for austenite not transforming to martensite seems to be the interrupted pattern of loading. During tensile multi-loading to a single specimen, at the interruptions after a particular strain level, the dislocations got relaxed due to the removal of load. Back stress was exerted on the dislocations and these dislocations moved towards their original sources.

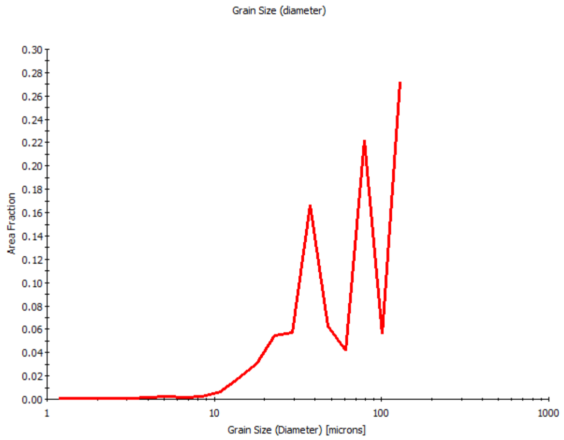

**Fig. 4.24 Grain size distribution of starting material**

Some of the dislocations were annihilated with the negative dislocations produced at the same sources and cancelled the effects (Dieter, 1988). The martensite formation in the material was delayed because the required dislocation density was not accumulated in the grains due to the repeated loading and unloading of the specimens. The dislocation density was also low as the AISI 304L steel under investigation was not very fine grained having average grain size in the range 50-70 µm (refer Figure 4.24). The Electron Back Scattered Diffraction (EBSD) phase maps shown in Figure 4.25 at different tensile deformations give the evidence that no martensitic transformation had occurred up to 30% strain level.

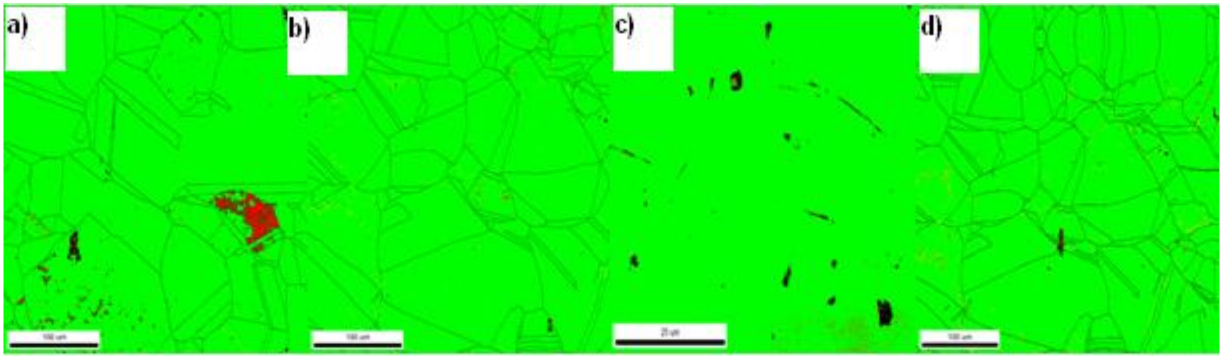

Fig. 4.25 EBSD phase maps at different strains a) 0% b) 7% c) 10% d) 30%

## 4.8 VOID FORMATION

During tensile experimentation the void formation observed is shown below in scanning electron microscope (SEM) micrographs. These micrographs gave the clear evidence of void formation at the slip bands. The voids were formed along the slip bands in the material. Voids, phenomenon of the ductile failure of the material was observed in the experiment before the load v/s extension curve reached the ultimate tensile stress (UTS) value.

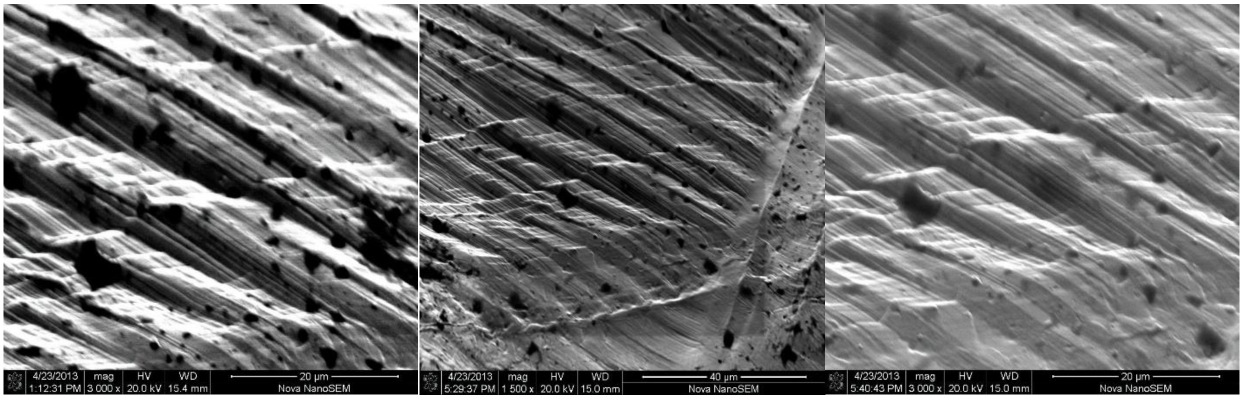

**Fig. 4.26 SEM Micrographs Showing the Void Formation during Tensile Loading**

## 4.9 PHASE TRANSFORMATION IN BI-MODAL AUSTENITIC STAINLESS STEEL

In the second part of this thesis work, experiments were conducted on an as received bi-modal (BM) type AISI 304L stainless steel to investigate the strain induced α’-martensitic transformation (SIM) during tensile deformation in the strain range of 0.21 to 0.28 (true strain). The as received material prepared through thermal cycling process mainly contained bi-modal grains of size, 0.5 µm and 1.5 µm. Figure 4.27 (a & b) show the grain size distribution in the bi-modal type AISI 304L stainless steel under investigation.

Berbenni et al. (2007) studied the deformation of heterogeneous grain distribution and showed that the coarser grains with more plastic deformation have lower internal stresses and the finer grains with low plastic deformation had higher internal stresses in the grains. This phenomenon depended upon the Hall-Petch strengthening effect. Thus, in the present work, the grains with grain size of 1.5μm showed more plastic deformation in the tensile stress direction while the grains with lesser size (<0.5μm) showed elastic nature of deformation. This revealed that strain localization was taking place.

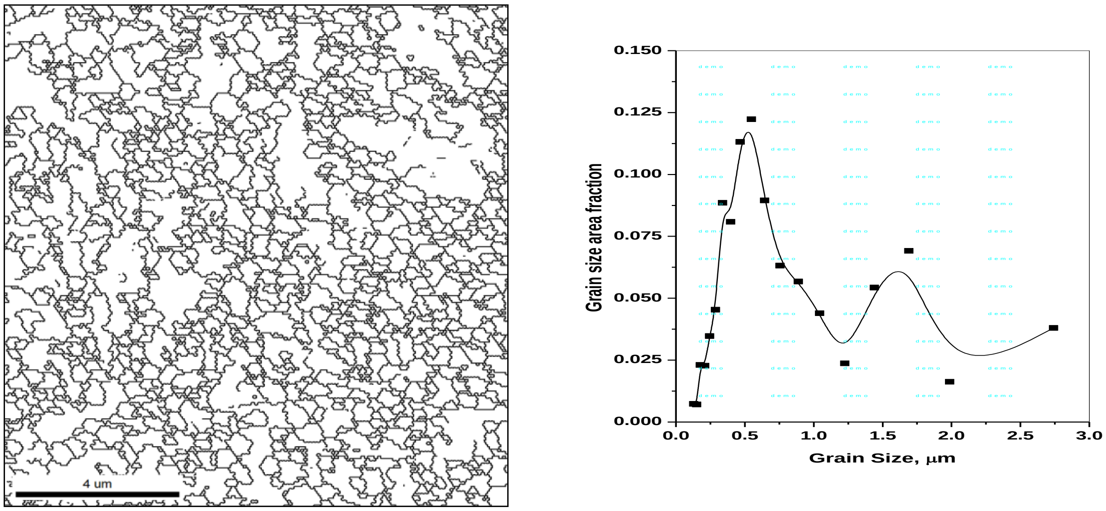

**(a)** **(b)**

**Fig. 4.27 a) EBSD Grain Boundary Map Showing (a) grain size distribution and (b) bi-modal type distribution with minima at 0.5 µm and maxima at about 1.5 µm**

Figure 4.28 and Figure 4.29 show the relation between true strain and percentage volume of martensitic transformation in the bi-modal type material.

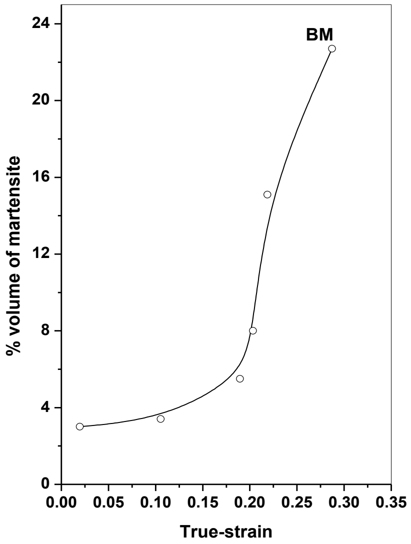

**Fig. 4.28 Volume Fraction of SIM with True Strain**

In Figure 4.29, the area with grey shade represents the austenite phase and the remaining (all colors except grey) represent martensite phase. It can be observed that martensite content is continuously increasing with increase in true strain value.

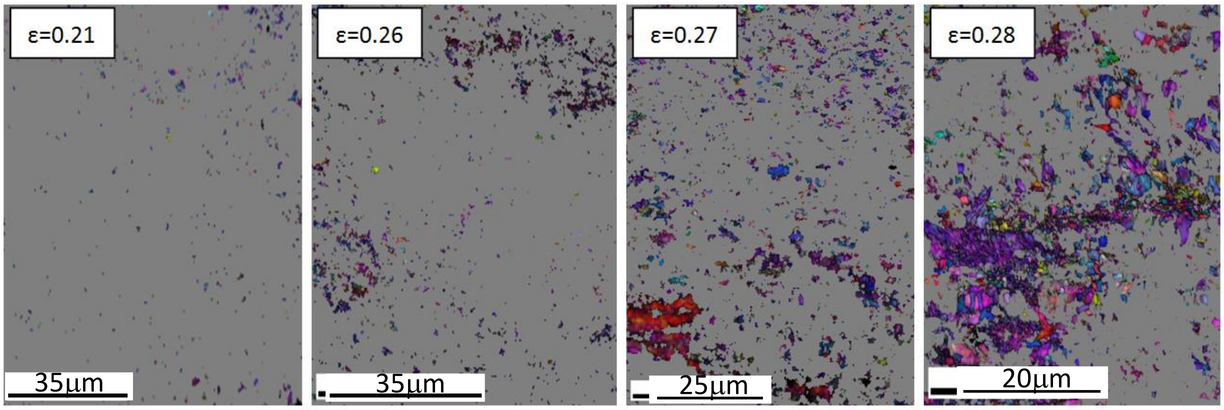

**Fig. 4.29 EBSD IPF Map showing increase in percent volume and changes in distribution pattern of α′-martensite with increasing true-strain**

Kernel Misorientation Mapping was done with the help of EBSD which revealed that strain accumulation in grains depends upon the grain size in bi-modal type distribution and on the misorientation of grain boundaries.

Finer grains (size up-to 0.5 µm) underwent elastic deformation up to 0.28 strain level (at necking) and appeared at relatively higher strain state (shown with bright green and red color). The coarse grains (size in the range, 0.5 - 1.5 µm) underwent large plastic deformation and appeared at relatively low strain state (shown with blue color) in Figure 4.30.

Figure 4.30 shows the Kernel Misorientation Mapping for the bi-modal material. The figure shows higher stress concentration in relatively finer grains. The magnified view (Figure 4.29) of encircled area (with arrows) indicates high strains near the grain boundaries.

Figure 4.31 depicts the Grain Boundary Misorientation plots showing change in misorientation angles in austenite and α’-martensite regions with increase in true-strain level. The Grain Boundary Misorientation Plots in Figure 4.31 show a decrease in high angle grain boundaries in the austenite region with increase in true strain levels. On the contrary, in the α’-martensite phase regions, an increase in the high angle grain boundaries was observed with increased true strain levels.

Figure 4.32 shows the Grain Boundary Map from EBSD analysis for the post tensile deformed specimens. The figures clearly reveal that martensite phase nucleates and grow at finer grains (initially observed at a true strain level of 0.21). |Also the figure reveals and seconds the earlier reporting (Figure 4.29) that amount of martensite phase in this bi-modal steel increases at the expense of decrease in the austenite phase with increase in true strain level.

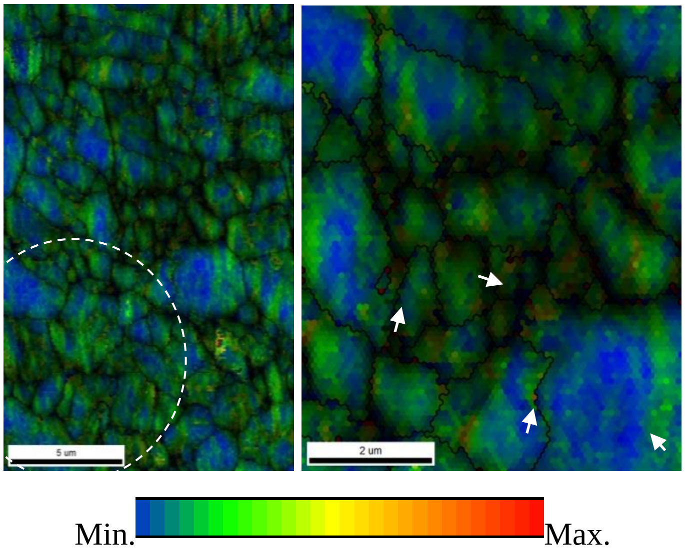

**Fig. 4.30 Kernel Average Misorientation Map showing Strain Concentration in Fine Grains in at 0.21 True Strain**

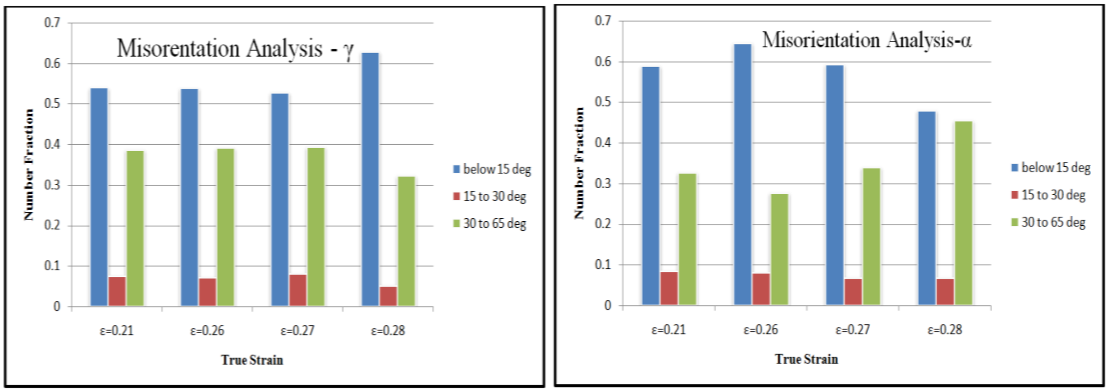

**(a)** **(b)**

**Fig. 4.31 Number Fraction of Grain Boundaries with Specific Misorientation Angle versus True Strain for (a) Austenite (b) Martensite**

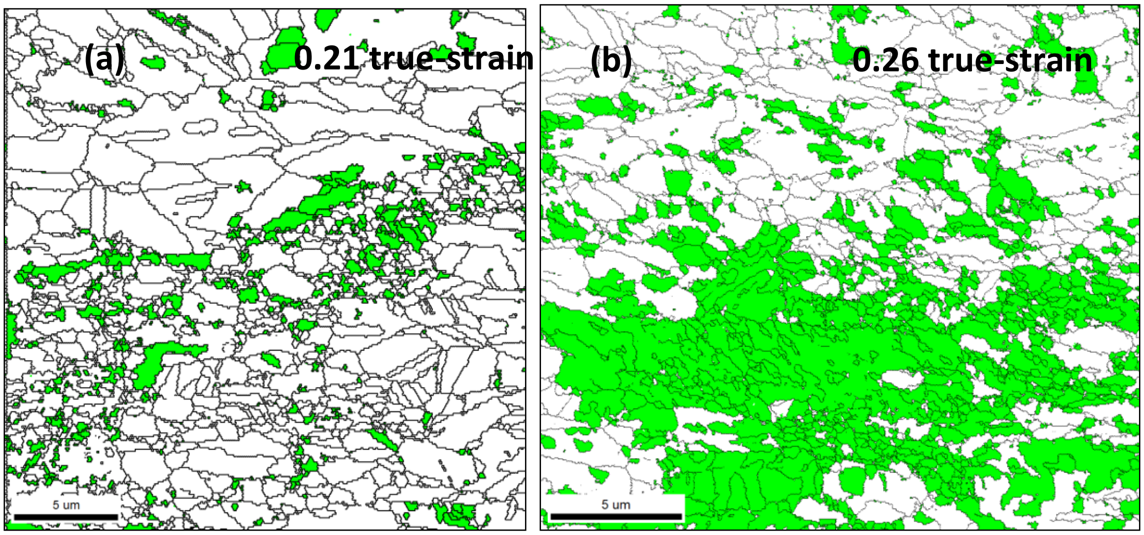

**Fig. 4.32 EBSD Analysis of Post Tensile Deformed Specimen showing Grain Boundary Map at two Strain Levels (a) 0.21 True-Strain and (b) at 0.26 True-Strain**

The results presented in Part-1 of this chapter give the detail of in-situ tensile deformation behavior of AISI 304L austenitic stainless steel in low strain and high strain ranges. Annealing twins in the grains were observed after cold rolling and then annealing treatment was given to the material. The annealing twins were also observed in the material as reported by (Cullity, 1956). He reported that annealing twins present in the cold-worked and annealed FCC material are due to the change in ABCABCABC stacking sequence of the material. Hosford (2005) reported about the tensile deformation behavior of FCC materials. The author reported that for FCC crystal oriented in the basic stereographic triangle, tensile axis will rotate towards the [101] direction until it reaches at [001]-[111] boundary near [112] stable orientation shown in Figure 4.33.

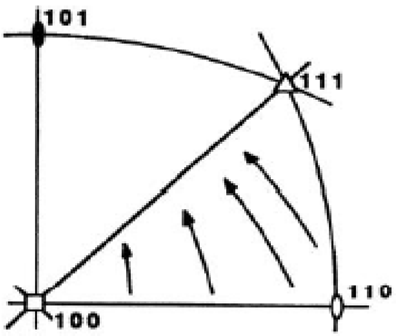

**Fig. 4.33 Primary Slip on [101] causes the Tensile Axis to Rotate at [101]**

(Image Source: Hosford, 2005)

Honeycombe (1968) reported that the deformation behavior of FCC materials can be divided in three stages according to increased level of strains. The author reported the effect of orientation of the grains on the deformation behavior. The first stage of deformation (without strain hardening and deformation in easy glide with unit slip system) activated shows change in orientations of grains in the soft regions with high Schmid factor to the stable [112] direction at [001]-[111] boundary of the stereographic triangle as shown in  Figure 4.34.

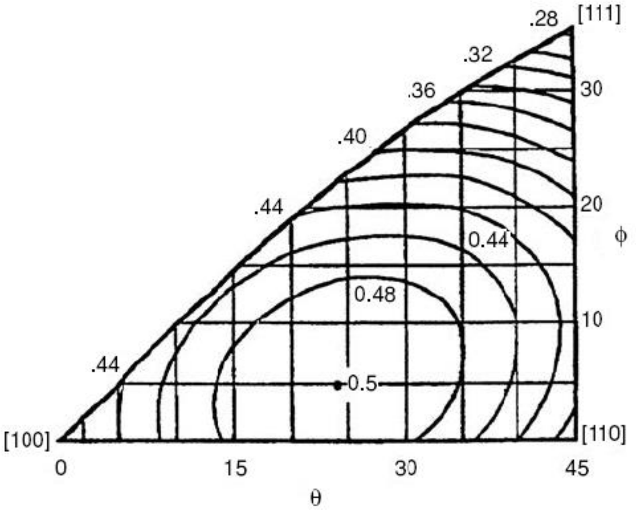

**Fig. 4.34 Contours of Constant Schmid Factors in FCC**

(Image Source: Hosford, 2005)

At strain levels up to 6%, the grains lying in the center of the stereographic triangle showed orientation changes due to the high Schmid factor of grains in this region (i.e. soft region). The grains with high Schmid factors lying in the soft regions of the stereographic triangle oriented towards the stable orientation in [112] direction at [001]-[111] boundary. Slip phenomenon was observed in only one grain in the hard orientations near [111]-[101] boundary and [111] pole at 6% strain level. The grains oriented at [001]-[111] boundary at [115] and [113] orientations showed their orientation change at stable [112] orientation towards [111] pole. The grains in the hard orientation did not show any orientation change up to 6% strain level due to their low Schmid factor and also for the reason that these grains were lying away from the tensile axis aligned at [101] direction. The EBSD grain orientation maps clearly revealed this behavior of grain orientation change as discussed above which is in well agreement with the literature reported by Honeycombe (1968) and Hosford (2005).

The effect of the orientation of neighbouring grain's orientation was also observed from the orientation changes with increased level of strains which showed that the grain lying between the grains of high Schmid factors inhibited orientation changes when the neighbouring grains rotated to comparatively low Schmid factor areas/towards the stable [112] orientation in the stereographic triangle.

Grains having twinned regions showed the orientation changes in the directions other than the stable orientation [112] and also in the opposite direction of twinned region in the stereographic triangle. This showed that twinned grains showed different behavior than the normal behavior showed by the FCC materials in stage-1 deformation. The small fraction of grain boundaries shifted from low angle to high angle grain boundaries. This was attributed to strain accumulation in regions of grain boundaries with dislocation accumulation in these areas with increased strains.

The results from the analysis of deformation behaviour at high strain levels from 7% to 30% showed the grain orientation changes with similar behaviour as was shown in the low strain levels with slip mediated plastic deformation. The grain orientation changes on the slip lines were observed in high strain levels towards the [001]-[111] boundary of stereographic triangle at stable orientation [112]. The grains with twinned regions within these grains showed different behavior at high strain levels also. The orientation of the grains and their twinned region was in the different orientations after deformation. Multiple-variant slip systems were activated in the material at 14% strain level and these showed further growth with increase in strain levels up to 30%.

The results obtained from the tensile experiment of bi-modal type grain distributed material include the effect of grain size distribution on strain induced martensite transformation in the material. The fine grains which showed elastic deformation up to 0.28 true strains (at necking) and appeared in the high strain states (shown in kernel average misorientation map) exhibited strain induced martensitic transformation. Also, the grain boundary regions having high degree of misorientations exhibited strain induced martensite transformation. The grains with coarser size did not show any significant strain induced martensitic transformation; however, these grains underwent large plastic deformation mediated with slip.

The results obtained in the present work showed agreement with the study reported by Staudhammer et al. (1983). It was reported that in UFG materials, the embryos of martensite formed and their growth was there with increased strain level at small strains; however the possibility of slip mediated plastic deformation is limited in UFG materials. Also results reported by Lee et al. (2007) showed the nucleation of α′-martensite at these strained grain boundaries in UFG austenitic stainless steels and their growth into the grains. The results obtained from this study showed that α′-martensite transformation from the austenitic grains in the strained grain boundary regions having degree of misorientation more than $15^0$ are also in well agreement with the study of previous authors.

# CHAPTER 5

# CONCLUSIONS

## 5.1 GENERAL

The austenitic stainless steels are very useful engineering materials due to their good corrosion resistant, formability, oxidation resistance and good luster but these steels have low mechanical strength. The main emphasis of the research on austenitic stainless steels (ASS) is to increase mechanical strength of these steels by retaining high uniform elongation percentage value. The present work has been done with the objective to study the microstructural changes in respect of grain orientation changes and phase transformation during tensile deformation. The study of tensile deformation behavior in this respect opens up the new routes to alter the mechanical properties of materials by engineering the microstructure of the material. The effect of grain orientation and annealing twinning on the deformation behavior has been reported in the present work. Deformation of FCC materials in stage-1 includes the rotation of the grains by unit slip system activated lying in soft regions having high Schmid factor values in the stereographic triangle. If the rotation of the grains is delayed to high strains, then the stage-1 range of deformation can be enlarged and strain hardening can be delayed which further increase in the uniform elongation of the material. So, in order to engineer the grain orientation the study of microstructural changes in the material was very necessary. So the rotation of the grain’s tracked in low strain to high strain range and the behavior of the grain rotation is analyzed. It was observed that in low strain range, the grains lying near [101] pole or near the [123] orientation without annealing twins with in these grains, showed rotation of these grains towards the stable [112] orientation at [001]-[111] boundary in the stereographic triangle. The grains with annealing twins within them showed a different behavior (if the grain rotates towards the preferred orientation [112] then the twinned region rotates in other direction and vice-versa).

In the latter part of present work, the effect of grain size distribution and misorientation between grains on strain induced α’-martensitic transformation has been described.

## 5.2 RESULTS AND CONCLUSIONS

The main results obtained from the present experimental work and the conclusions drawn from the results are summarized in this section. The results drawn from the study are summarized in the same manner or sequence as the discussion of results has been reported in Chapter 4.

### *5.2.1 Deformation Behavior in Low Strain Regime*

- The starting material revealed a random orientation of all the grains i.e. grains were observed to be lying in different regions of stereographic triangle. Also, in many grains, because of the prior cold working followed by solution annealing treatment, annealing twins were observed. Further, in the starting material, a large fraction of grain boundaries were observed to be high angle grain boundaries (with peak of number fraction at nearly $60^0$ misorientation angle). The Schmid factor values were very high for very high fraction of grains at the starting stage.
- In the low strain regime up to 6% strain level, the grains without any twinned region within them and lying in the soft region with high Schmid factor deformed initially towards the stable orientation [112] at [001]-[111] boundary.
- Grains having single twinned regions within them showed orientation changes in directions other than the stable orientation [112] and also in the opposite direction of twinned region in the stereographic triangle. This showed that twinned grains show a different behavior than the normal behavior shown by the FCC materials in Stage-1 deformation. Another significant observation was with regards to grains having multiple twinned regions which showed no orientation changes with increased strain levels.
- The effect of orientation of the neighboring grains on the rotation of grains was also observed. It was concluded that with increased stain levels, the grain lying between grains of relatively higher Schmid factor inhibited any orientation change when the neighboring grains rotated to comparatively low Schmid factor areas/towards the stable [112] orientation in the stereographic triangle.
- The grain orientation changes were also observed within the grains at their different locations. This meant that same grain had different orientations with in the same grain. The portions of the grain where slip had initiated showed a different orientation from portions where slip was not present.

- The grains which were lying in the hard regions of the stereographic triangle in the starting material were observed to remain at the same orientations at all strain levels.
- Misorientation angle changes for grain boundaries was also observed up to 6% strains from low angle grain boundaries to high angle grain boundaries (with misorientation angle above $30^o$).
- Grains with high Schmid factor values rotated first towards the stable [112] orientation and the highest peaks of the Schmid factor shifted to lower values with increase in strain levels.

### *5.2.2 Deformation Behavior in High Strain Regime*

- The analysis of results of the deformation behavior at high strain levels from 7% to 30% showed the grain orientation changes with similar behavior as in the low strain levels with slip mediated plastic deformation. The grain orientation changes on the slip lines were observed at high strain levels towards the [001]-[111] boundary of stereographic triangle at stable orientation [112].
- The predominant phenomenon of plastic deformation in AISI 304L steel was still slip. The grain orientation changes in high strain regimes were observed at the slip lines. This showed that the slip induced in the material was the main phenomenon causing the rotation of the grains. However, the single variant slip enhanced to multi-variant slip with increase in strain levels beyond 10% strain level. This was an indication of the initiation of strain hardening phenomenon in the material.
- Void formation was observed at the interaction of the slip lines (at the interaction of the multi-variant slip lines).
- In the present experimental work, interrupted loading was done to reach a higher strain level. This interrupted in-situ tensile testing led to the generation of back stresses in the dislocations interacting with other dislocations or the ones which were piled up at the grain boundaries. As a result, the stresses generated were released resulting in absence of martensitic transformation and strain hardening.

### *5.2.3 Phase Transformation in Bi-Modal Type Austenitic Stainless Steel*

- The strain induced α’-martensitic transformation in relatively finer grains with very limited slip mediated plastic deformation was observed in bi-modal type austenite grains. This was mainly due to the increase in dislocation density and high internal stresses in these smaller grains.

- The grain boundaries regions with high misorientation (with misorientation angle $>15^0$) also showed strain induced α’-martensite transformation in these regions. This was attributed to the fact that high angle grain boundaries are the strained grain boundaries.
- Martensitic transformation in coarse grains was absent. Though, the deformation in these grains was slip mediated plastic deformation but because of their relatively larger sizes, low internal stresses were accumulated in these areas and the SIM transformation could not be observed.

## 5.3 MAJOR CONCLUSIONS AND RECOMMENDATIONS

Attempts made to track the changes in grain orientations during tensile deformation of AISI 304L austenitic stainless steel has been successful. The following are the major conclusions and recommendations which can be made from the present experimental investigations:

- The grains without twins showed a similar trend of rotation as is shown in general by FCC materials that these grains moved towards the [112] stable orientation at [001]-[111] boundary in the stereographic triangle. The grains lying in the soft regions showed the rotation initially because of the high Schmid factor in this region of stereographic triangle. However, the grains with twins showed a different deformation behavior, in the sense that the grains and the twinned regions rotated to different orientations with some particular relation. Up to 30% strain, no strain hardening was observed (in the load v/s extension curves) because the deformation was still in Stage-1 FCC deformation.
- The dominant plastic deformation phenomenon observed in the present work was slip. Initially, the unit slip system got activated in the grains lying in the soft regions (at the center at [123] and near [101] pole) of the stereographic triangle. At strain levels beyond 10%, multi-variant slip was observed. This means that the slip occurred at more than one slip systems. Thus, it was concluded that during the tensile deformation of AISI 304L austenitic stainless steel, at low strain levels up to 10%, deformation proceeds by unit slip system whereas at higher strain levels, it proceeds by multi-variant slip system.
- In the bi-modal type austenite grain distribution, the extent of strain-induced α’-martensite transformation increased with increasing the true strain level. Further, the strain-induced α’-martensite transformation was observed in relatively small sized grains. Though there was very limited slip mediated plastic deformation in smaller grains but due to the increased internal stresses (as dislocations could not move because of the small size of grains), SIM

transformation was observed. However, in the relatively coarse grains which underwent sufficient slip mediated plastic deformation, there was absence of martensitic transformation because of the low internal stresses accumulated in these coarser grains because of their comparatively larger grain size.

| **Elongation (mm)** | **Force (N)** | **Elongation (mm)** | **Force (N)** | **Elongation (mm)** | **Force (N)** |
|---|---|---|---|---|---|

- The strain induced α’-martensite transformation was observed in the grain boundary regions with high misorientation angles of more than 15$^o$. The high misorientation angles were attributed to the high strain localization in the grain boundary regions. The high internal stresses in the grain boundary region was attributed to the dislocation accumulation in these regions which led to the strain induced α’-martensitic transformation.

### 5.4 SCOPE OF FUTURE WORK

Tensile deformation behavior can be further investigated for austenitic stainless steels in Stage-2 and Stage-3 deformation stage at higher strain levels. The relation between the orientation of grains and their twins can be further studied. Similar to the investigations during tensile deformation (as done in the present study), the creep and fatigue behavior can also be studied. New routes can be developed to engineer the deformation behavior regarding grain orientation changes for enhancing the mechanical properties of materials (especially. extending the Stage I deformation stage for better ductility).

## APPENDIX 1: Data for Force v/s Elongation, upto 7% Strain Level

| | | | | | |
|---|---|---|---|---|---|
| 0 | 6.07 | 0.376 | 652.35 | 0.731 | 822.21 |
| 0 | 8.89 | 0.376 | 652.62 | 0.732 | 822.37 |
| 0 | 11.79 | 0.377 | 652.85 | 0.732 | 822.59 |
| 0.001 | 14.74 | 0.377 | 653.22 | 0.733 | 822.88 |
| 0.001 | 17.64 | 0.377 | 653.53 | 0.733 | 823.13 |
| 0.002 | 20.64 | 0.378 | 654.27 | 0.733 | 823.27 |
| 0.002 | 24.4 | 0.378 | 654.95 | 0.734 | 823.67 |
| 0.002 | 27.25 | 0.379 | 655.59 | 0.734 | 823.85 |
| 0.002 | 29.87 | 0.379 | 656.06 | 0.734 | 824.12 |
| 0.002 | 32.48 | 0.379 | 656.65 | 0.735 | 824.38 |
| 0.003 | 35.37 | 0.38 | 656.84 | 0.736 | 824.93 |
| 0.003 | 38.06 | 0.38 | 657.01 | 0.736 | 825.5 |
| 0.003 | 40.68 | 0.381 | 657.44 | 0.737 | 826.02 |
| 0.003 | 43.43 | 0.381 | 657.57 | 0.737 | 826.48 |
| 0.004 | 46.04 | 0.381 | 657.97 | 0.738 | 826.84 |
| 0.004 | 48.73 | 0.382 | 658.1 | 0.738 | 827.14 |
| 0.004 | 51.78 | 0.382 | 658.47 | 0.739 | 827.14 |
| 0.004 | 54.28 | 0.383 | 658.69 | 0.739 | 827.44 |
| 0.005 | 56.73 | 0.383 | 659 | 0.739 | 827.65 |
| 0.005 | 58.82 | 0.384 | 659.4 | 0.74 | 827.96 |
| 0.005 | 61.07 | 0.384 | 659.68 | 0.741 | 828.05 |
| 0.005 | 63.22 | 0.385 | 660.03 | 0.741 | 828.27 |
| 0.005 | 65.55 | . | . | | |
| 0.006 | 67.74 | . | . | | |
| 0.006 | 69.94 | . | . | | |
| 0.007 | 72.18 | . | . | | |

|  |  |  |  |
|---|---|---|---|
| 0.007 | 74.43 | . | . |
| 0.007 | 76.63 | 0.719 | 820.02 |
| 0.007 | 78.76 | 0.72 | 820.19 |
| 0.007 | 80.98 | 0.72 | 820.36 |
| 0.007 | 83.31 | 0.721 | 820.7 |
| 0.007 | 85.59 | 0.721 | 820.96 |
| 0.007 | 87.84 | 0.722 | 821.1 |
| 0.008 | 87.89 | 0.723 | 820.68 |
| 0.008 | 87.98 | 0.724 | 820.54 |
| . | . | 0.725 | 820.39 |

## APPENDIX 2: Data for Force v/s Elongation, upto 10% Strain Level

| Elongation (mm) | Force (N) | Elongation (mm) | Force (N) |
|---|---|---|---|
| 0 | 2.36 | 0.117 | 659.22 |
| 0 | 2.36 | 0.117 | 661.58 |
| 0 | 2.41 | 0.118 | 663.75 |
| 0 | 2.37 | 0.119 | 666.06 |
| 0 | 2.44 | 0.12 | 668.42 |
| 0 | 2.38 | 0.12 | 670.79 |
| 0 | 2.41 | 0.12 | 673.22 |
| 0 | 2.45 | 0.121 | 675.51 |
| 0 | 2.51 | 0.122 | 677.85 |

|  |  |  |  |
|---|---|---|---|
| 0 | 2.44 | 0.122 | 680.15 |
| 0 | 2.2 | 0.122 | 682.45 |
| 0 | 0.91 | 0.123 | 684.79 |
| 0 | 1.99 | 0.124 | 687.06 |
| 0 | 3.87 | 0.124 | 689.4 |
| 0 | 6.09 | 0.124 | 691.31 |
| 0 | 8.59 | . | . |
| 0 | 11.23 | . | . |
| 0.001 | 13.62 | . | . |
| 0.001 | 16.11 | . | . |
| 0.001 | 19.42 | . | . |
| 0.002 | 21.54 | 0.389 | 966.51 |
| 0.002 | 23.71 | 0.389 | 966.74 |
| 0.002 | 25.9 | 0.39 | 966.89 |
| 0.002 | 28.21 | 0.391 | 967.17 |
| 0.003 | 30.3 | 0.391 | 967.42 |
| 0.003 | 32.35 | 0.392 | 967.66 |
| 0.003 | 34.66 | 0.393 | 968.45 |
| 0.004 | 36.85 | 0.393 | 969.16 |
| 0.004 | 39.1 | 0.394 | 969.64 |
| 0.004 | 41.31 | 0.395 | 970.2 |
| 0.005 | 43.57 | 0.395 | 970.65 |
| 0.005 | 45.74 | 0.396 | 971.05 |
| 0.005 | 47.9 | 0.396 | 971.35 |
| 0.006 | 50.11 | 0.396 | 971.56 |
| 0.006 | 52.23 | 0.397 | 971.79 |

| | | | |
|---|---|---|---|
| . | . | 0.397 | 972.06 |
| . | . | 0.398 | 972.18 |
| . | . | 0.398 | 972.57 |
| . | . | 0.398 | 972.82 |
| . | . | 0.399 | 972.98 |
| 0.116 | 650.8 | 0.399 | 973.12 |

## APPENDIX 3: Data for Force v/s Elongation, upto 14% Strain Level

| **Elongation (mm)** | **Force (N)** | **Elongation (mm)** | **Force (N)** |
|---|---|---|---|
| 0.001 | 1.13 | 0.301 | 939.88 |
| 0 | 1.16 | 0.301 | 939.93 |
| 0 | 1.03 | 0.301 | 940.16 |
| 0 | 1.17 | 0.301 | 940.4 |
| 0 | 1.17 | 0.302 | 941.04 |
| 0 | 1.16 | 0.302 | 941.75 |
| 0 | 1.2 | 0.303 | 942.34 |
| 0.001 | 1.28 | 0.304 | 942.84 |
| 0 | 1.25 | 0.304 | 943.24 |
| 0 | 1.18 | 0.305 | 943.58 |
| 0 | 1.32 | 0.305 | 943.98 |
| 0 | 0.97 | 0.306 | 944.37 |
| 0 | 0.11 | 0.307 | 944.53 |
| 0 | 1.02 | . | . |
| 0 | 3.39 | . | . |
| 0.001 | 6.18 | . | . |
| 0.001 | 9.22 | . | . |
| 0.002 | 12.12 | . | . |

|  |  |  |  |
|---|---|---|---|
| 0.002 | 15.16 | 0.53 | 1007.92 |
| 0.002 | 18.73 | 0.53 | 1007.94 |
| 0.003 | 21.63 | 0.531 | 1007.81 |
| 0.003 | 24.22 | 0.532 | 1007.52 |
| 0.004 | 26.8 | 0.532 | 1007.32 |
| 0.004 | 29.3 | 0.533 | 1007.38 |
| 0.004 | 31.63 | 0.533 | 1007.23 |
| 0.005 | 33.99 | 0.534 | 1007.22 |
| 0.005 | 36.21 | 0.534 | 1007.33 |
| 0.005 | 38.58 | 0.535 | 1007.36 |
| 0.005 | 40.67 | 0.535 | 1007.47 |
| 0.006 | 42.81 |  |  |
| 0.006 | 44.78 |  |  |
| 0.007 | 46.85 |  |  |
| 0.007 | 48.65 |  |  |
| 0.008 | 50.44 |  |  |
| . | . |  |  |
| . | . |  |  |
| . | . |  |  |
| . | . |  |  |
| . | . |  |  |
| 0.297 | 939.19 |  |  |
| 0.298 | 939.25 |  |  |
| 0.298 | 939.3 |  |  |

## APPENDIX 4: Data for Force v/s Elongation, upto 30% Strain Level

| **Elongation (mm)** | **Force (N)** | **Elongation (mm)** | **Force (N)** |
|---|---|---|---|

|  |  |  |  |
|---|---|---|---|
| 0 | 0.61 | 1.001 | 1209.3 |
| 0.001 | 3.08 | 1.001 | 1209.36 |
| 0.001 | 5.54 | 1.002 | 1209.38 |
| 0.002 | 7.92 | 1.002 | 1209.57 |
| 0.002 | 10.51 | 1.003 | 1209. 71 |
| 0.002 | 13.66 | 1.003 | 1209.82 |
| 0.003 | 15.86 | 1.004 | 1209.9 |
| 0.003 | 18.08 | 1.004 | 1210.08 |
| 0.004 | 20.8 | 1.004 | 1210.33 |
| 0.005 | 27.08 | 1.005 | 1210.62 |
| 0.006 | 33.52 | 1.005 | 1210.73 |
| 0.006 | 36.68 | . | . |
| 0.006 | 39.19 | . | . |
| 0.007 | 41.66 | . | . |
| 0.007 | 44.29 | . | . |
| 0.008 | 46.85 | . | . |
| 0.008 | 49.71 | 1.813 | 1337.11 |
| 0.01 | 52.38 | 1.814 | 1336.73 |
| 0.01 | 54.54 | 1.814 | 1336.51 |
| 0.011 | 56.68 | 1.815 | 1336.24 |
| 0.011 | 58.77 | 1.815 | 1336 |
| 0.011 | 61.03 | 1.815 | 1335.79 |
| 0.012 | 63.15 | 1.816 | 1335.63 |
| 0.012 | 65.35 | 1.817 | 1335.61 |
| 0.013 | 67.4 |  |  |
| 0.013 | 69.61 |  |  |

| | |
|---|---|
| 0.013 | 71.75 |
| 0.014 | 74.19 |
| 0.014 | 76.11 |
| 0.014 | 77.95 |
| 0.015 | 79.74 |
| 0.016 | 81.57 |
| 0.016 | 83.6 |
| 0.017 | 85.38 |
| 0.017 | 87.29 |
| 0.017 | 89.31 |
| . | . |
| . | . |
| . | . |
| . | . |
| . | . |
| 0.999 | 1209.15 |

## REFERENCES

---

- Abbaschian, R., Abbaschian, L. and Reed–Hill, R. E. (2009), ‘Physical Metallurgy Principles’, *Cengage Learning*, ed. 4th, Stamford (USA), pp. 82–157.

- Allain, S., Chateau, J. P. and Bouaziz, O. (2004), ‘A physical model of twinning–induced plasticity effect in a high manganese austenitic steel’, *Materials Science and Engineering A*, Vol. 387–389, pp. 143–147.
- Avner, S. H. (1997), ‘Introduction to Physical Metallurgy’, *Tata McGraw Hill*, New Delhi, ed. 2nd.
- Bacon, D. J. and Hull, D. (2001), ‘Introduction to Dislocations’, *Butterworth–Heinemann*, London, ed. 4th, pp. 102–144.
- Berbenni, S., Favier, V. and Berveiller, M. (2007), ‘Impact of the grain size distribution on the yield stress of heterogeneous materials’, *International Journal of Plasticity*, Vol. 23, pp. 114-142.
- Bi, H. Y., Kokawa, H., Wang, Z. J., Shimada, M. and Sato, Y. S. (2003), ‘Suppression of chromium depletion by grain boundary structural change during twin–induced grain boundary engineering of 304 stainless steel’, *Scripta Materialia*, Vol. 49, pp. 219–223.
- Callister, W. D. (2007), ‘Material Science and Engineering’, *John Wiley and Sons, Inc.*, ed. 7th, New York, pp. 88–92.
- Cavaliere, P. (2008), ‘Strain rate sensitivity of ultra–fine and nanocrystalline metals and alloys’, *Physica B*, Vol. 403, pp. 569–575.
- Chia, K.H., Jung, K. and Conrad, H. (2005), ‘Dislocation density model for the effect of grain size on the flow stress of a Ti–15.2 at.% Mo β–alloy at 4.2–650K’, *Materials Science and Engineering A*, Vol. 409, pp. 32–38.
- Chowdhury, S.G., Das, S. and De, P.K. (2005), ‘Cold rolling behaviour and textural evolution in AISI 316L austenitic stainless steel’, *Acta Materialia*, Vol. 53, pp. 3951–3959.
- Cullity, B. D. (1956), ‘Elements of X-Ray Diffraction’, *Addison-Wesley Publishing Company, Inc.*, ed. 1st, USA, pp. 55–65.
- Das, A., Chakraborti, P. C., Tarafder, S. and Bhadeshia, H. K. D. H. (2011), ‘Analysis of deformation induced martensite transformation in stainless steels’, *Materials Science and Technology*, Vol. 27(1), pp. 366–370.
- Das, A., Tarafder, S. and Chakraborti, P. C. (2011), ‘Estimation of deformation induced martensite in austenitic stainless steels’, *Materials Science and Engineering A*, Vol. 529, pp. 9–20.

- Das, A. and Tarafder, S. (2009), 'Experimental investigation on martensitic transformation and fracture morphologies of austenitic stainless steel', *International Journal of Plasticity*, Vol. 25, pp. 2222–2247.
- Dieter, G. E. (1988), 'Mechanical Metallurgy', *McGraw–Hill Book Company,* ed. 4th, London, pp. 103–183.
- Elsariti, S. M. and Haftirman (2013), 'Behaviour of stress corrosion cracking of austenitic stainless steels in sodium chloride solutions', *Procedia Engineering*, Vol. 53, pp. 650–654.
- Felbeck, D. K. and Atkins, A. G. (1996), 'Strength and Fracture of Engineering Solids', *Prentice Hall, Inc.*, USA, ed. 2nd, pp. 103.
- Gardner, L., Talja, A. and Baddoo, N. R. (2006), 'Structural design of high–strength austenitic stainless steel', *Thin–Walled Structures*, Vol. 44, pp. 517–528.
- Hertzberg, R. W. (1996), 'Deformation and Fracture Mechanics of Engineering Materials', *John Wiley and Sons, Inc.*, ed., 4th, USA, pp. 57–107.
- Honeycombe, R. W. K. (1968), 'The Plastic Deformation of Metals', *Edward Arnold Publishers Ltd.*, ed. 1st, *Great Britain*, pp. 5-127.
- Hosford, W. F. (2005), 'Mechanical Behavior of Materials', *Cambridge University Press*, ed. 2nd, UK, pp. 120–135.
- Kim, Y. S., Nam, S. M. and Kim, S. J. (2007), 'Strain rate dependence of deformation behavior of high–nitrogen austenitic steels', *Journal of Materials Processing Technology*, Vol. 187–188, pp. 575–577.
- Kobayashi, S., Hirata, M., Tsurekawa, S. and Watanabe, T. (2011), 'Grain boundary engineering for control of fatigue crack propagation in austenitic stainless steel', *Procedia Engineering*, Vol. 10, pp. 112–117.
- Kumar, B. R., Chowdhury, S. G., Narasaiah, N., Mahato, B. and Das, S. K. (2007), 'Role of Grain Boundary Character Distribution on Tensile Properties of 304L Stainless Steel', *Metallurgical and Materials transaction A.*
- Kumar, B.R., Das, S.K., Sharma, S. and Mahato, B. (2011), 'Formation of ultrafine grained microstructure in the austenitic stainless steel and its impact on tensile properties', *Materials Science and Engineering A*, Vol. 528, pp. 2209–2216.
- Lee, T. H., Oh, C. S., Kim, S. J. and Takaki, S. (2007b), 'Deformation twinning in high–nitrogen austenitic stainless steel', *Acta Materialia*, Vol. 55, pp. 3649–3662.

- Lee, Y. K., Jin, J. E. and Ma, Y. Q. (2007a), ‘Transformation-induced extraordinary ductility in an ultrafine-grained alloy with nanosized precipitates’, *Scripta Materialia*, Vol. 57, pp.707-710.
- Li, H., Ebrahimi, F. and Choo, H. (2006), ‘Grain size dependence of tensile behavior in nanocrystalline Ni–Fe alloys’, *J Mater Sci.*, Vol. 41, pp. 7636–7642.
- Marshall, P. (1984), ‘Austenitic Stainless Steels: Microstructure and Mechanical Properties’, *Elsevier Science Publishing Co., Inc.*, 1st ed., pp. 1–102.
- McDowell, D. and Mayne, W. C. (1966), ‘Stainless Steels’, *American Society for Metals,* Metals Park, Vol.18, *Lesson 1–Lesson 3.*
- McGuire, M. F. (2008), ‘Stainless Steels for Design Engineers’, *ASM International,* USA, pp. 69–78.
- Meyers, M. and Chawla, K. (2009), ‘Mechanical Behavior of Materials’, *Cambridge University Press,* ed. 2nd, U.K., pp. 268–277.
- Milad, M., Zreiba, N., Elhalouani, F. and Baradai, C. (2008), ‘The effect of cold work on structure and properties of AISI 304 stainless steel’, *Journal of Materials Processing Technology,* Vol. 203, pp. 80–85.
- Nagy, E., Mertinger, V., Tranta, F. and Solyom, J. (2004), ‘Deformation induced martensitic transformation in stainless steels’, *Materials Science and Engineering A,* Vol. 378, pp. 308–313.
- Park, W. S., Yoo, S. W., Kim, M. H. and Lee, J. M. (2010), ‘Strain–rate effects on the mechanical behavior of the AISI 300 series of austenitic stainless steel under cryogenic environments’, *Materials and Design,* Vol. 31, pp. 3630–3640.
- Pickering, F. B. (1978), ‘Physical Metallurgy and the Design of Steels’, *Applied Science Publishers Limited, London,* ed. 1st, pp. 226–266.
- Raghavan, V. (2006), ‘Physical Metallurgy: Principles and Practice’, *PHI Learning private Limited,* ed. 2nd, *New Delhi,* pp. 134–137.
- Rocha, M. R. and Oliveira, C. A. S. (2009), ‘Evaluation of the martensitic transformation in austenitic stainless steel’, *Materials Science and Engineering A,* Vol. 517, pp. 281–285.
- Schino, A.D. and Kenny, J.M. (2003), ‘Grain refinement strengthening of a microcrystalline high nitrogen austenitic stainless steel’, *Materials Letters,* Vol. 57, pp. 1830–1834.
- Sedriks, A. J. (1996), ‘Corrosion of Stainless Steels’, *John Wiley and Sons, Inc.*, 2nd ed., *USA*, pp. 13–15.

- Shen, Y. F., Li, X. X., Sun, X., Wang, Y. D. and Zuo, L. (2012), 'Twinning and martensite in a 304 austenitic stainless steel', *Materials Science and Engineering A*, Vol. 552, pp. 514–522.
- Shimada, M., Kokawa, H., Wang, Z. J., Sato, Y. S. and Karibe, I. (2002), 'Optimization of grain boundary character distribution for intergranular corrosion resistant 304 stainless steel by twin induced grain boundary engineering', *Acta Materialia*, Vol. 50, pp. 2331–2341.
- Singh, V. (2008), 'Physical Metallurgy', *Lomus offset press*, Delhi, ed. 1st .
- Smith, W. F. (2008), 'Materials Science & Engineering', *Tata McGraw–Hill Education, New Delhi,* ed. 4th, pp. 271–437.
- Staudhammer, K. P., Murr, L. E. and Hecker, S. S. (1983), 'Nucleation and evolution of strain-induced martensitic (B.C.C.) embryos and substructure in stainless steel: A transmission electron microscope study,' *Acta Metallica*, Vol. 31(2), pp. 267-274.
- Tsurekawa, S., Nakamichi, S. and Watanable, T. (2006), 'Correlation of grain boundary connectivity with grain boundary character distribution in austenitic stainless steel', *Acta Materialia,* Vol. 54, pp. 3617–3626.
- Xu, Y., Zhang, S. H., Cheng, M. and Song, H. W. (2012), 'In–situ X–ray diffraction study of martensitic transformation in austenitic stainless steel during cyclic tensile loading and unloading', *Scripta Materialia,* Vol. 67, pp. 771–774.
- Yang, P., Xie, Q., Meng, L., Ding, H. and Tang, Z. (2006), 'Dependence of deformation twinning on grain orientation in a high manganese steel', *Scripta Materialia*, Vol. 55, pp. 629–631
- Yeddu, H. K., Razumovskiy, V. I., Borgenstam, A., Korzhavyi, P. A., Ruban, A. V. and Agren, J. (2012), 'Multi–length scale modeling of martensitic transformations in stainless steels', *Acta Materialia*, Vol. 60, pp. 6508–6517.
- Yuan, Z. Z., Dai, Q. X., Cheng, X. N., Chen, K. M., Pan, L. and Wang, A. D. (2006), 'In–situ tensile test of high–nitrogen austenitic stainless steel', *Materials Characterization,* Vol. 56, pp. 79–83.

**WEB REFERENCES:**

- Leffler, B., 2013, Stainless steels and their properties, http://www.hazmetal.com/f/kutu/1236776229.pdf (downloaded on 03/05/13)

- http://img186.exs.cx/img186/5051/sss4nj.jpg (downloaded on 04/05/13)
- http://www.aksteel.com/pdf/markets_products/stainless/austenitic/301_Data_Sheet.pdf (downloaded on 10/05/13)
- http://www.espimetals.com/tech/stainlesssteel.pdf (downloaded on 10/05/13)